DIPLOMARBEIT

Studies of magnetic and electronic properties of quasi-one-dimensional metals

zur Erlangung des akademischen Grades
Diplom-Ingenieurin

im Rahmen des Studiums
Technische Physik

eingereicht von
Lisa Carina Reisinger, BSc
Matrikelnummer 01456543

ausgeführt am Institut für Festkörperphysik
der Fakultät für Physik der Technischen Universität Wien

unter der Aufsicht von
Ao.Univ.Prof. Dipl.-Ing. Dr.techn. Herwig Michor

Wien, 12. März 2021

Unterschrift Verfasserin

Unterschrift Betreuer

Abstract

Dimensionality is an important aspect in solid state physics and frequently connected to emergent phenomena such as high-temperature superconductivity, dimensionally frustrated magnetism and various others. One of these is the Peierls charge density wave instability which occurs in crystals with a quasi-one-dimensional electronic structure. This can result from crystal structures with chain-like building blocks but also appears under specific bonding conditions in typical three-dimensional crystals. The charge density wave transition (CDW) causes a modulation of the lattice which enlarges the periodicity in real space and therefore results in an inverse alteration of the Brillouin zone size, giving rise to extraordinary features like non-linear transport which may find use in modern electronic applications.

The motivation of this master thesis is divided into three aspects revolving around the electronically quasi-one-dimensional rare-earth nickel dicarbides ($RNiC_2$). Supplementary to single crystal diffraction experiments carried out by specialists, the nature of the structural and electronic modifications at phase transitions were examined with dilatometry, heat capacity and resistivity measurements. Characteristic features of the first and second order CDW transitions were distinguished. By applying the Clausius-Clapeyron and a modified Ehrenfest relation, it is revealed that the commensurate CDW order parameter is stabilized by pressure while the incommensurate order parameter is rather destabilized by pressure. Additionally, the magnetic ground state of $PrNiC_2$ was analyzed in order to ascertain possible dynamic frustration. The crystal field parameters and the energy level splitting due to the impact of the crystalline electric field were evaluated for $PrNiC_2$. Moreover, pseudo-ternary solid solutions of $LuNi_{1\text{-}x}Co_xC_2$ were grown in the optical floating zone furnace in order to determine the CDW critical point in dependence of the Ni/Co composition. It has earlier been attempted to discover the suppression of the CDW in polycrystalline samples which however due to emerging compositional inhomogeneity has been feasible only for very small degrees of substitution and accordingly small reductions of the Peierls temperature. Using the floating zone melting technique, it was possible to grow more homogeneous solid solutions, whereby the critical point of the suppression of the CDW state could be located to $LuNi_{(0.85\text{-}0.8)}Co_{(0.15\text{-}0.2)}C_2$.

Contents

1 Introduction and Motivation

Intriguing features in solid state physics are often associated with an essential property of the system, namely its dimensionality and the related topology of its Fermi surface. In crystals that exhibit quasi-one-dimensional electronic characteristics, the Fermi surface resembles quasi-planar Fermi surface sheets. An enlargement of the unit cell of such low-dimensional crystals in real space evokes a shift in the Brillouin zone boundaries and consequently enables the opening of an additional energy gap. Despite extensive studies on this so-called charge density wave (CDW) transition, there are still open questions and extraordinary characteristics to explore. Nonetheless, numerous spectacular features in CDW materials have already been discovered, including non-linear transport and high-temperature superconductivity which may have potential to find application in modern detectors, information processing or memory [1].

At the end of the 1970s, the finding of the crystal system of intermetallic rare-earth nickel dicarbides ($RNiC_2$, with R= La,...,Lu) was a novelty but arising interest in these materials owes the discovery of their quasi-one-dimensional electronic properties in the 2000s [2]. Rare-earths are 17 metallic elements including the 15 lanthanides, yttrium and scandium. The crystalline structure of rare-earth nickel dicarbides (with R= La,...,Lu and Y) has been studied and it was found that they display an orthorhombic unit cell, which belong to the space group *Amm2 (38)*, *cf.* Ref. [3], and the variation of the lattice constants reflects the lanthanide contraction. Even though the lattice of these metals is three-dimensional, the electronic properties display features of quasi-planar Fermi surface sheets which is reminiscent of a quasi-one-dimensional material [2, 4]. After ascertaining the existence of different $RNiC_2$ compounds, the focus of research was set on examining their magnetic features, as the magnetic moment of these materials is solely carried by the rare-earth element [5, 6]. Soon, the discovery of extraordinary physical phenomena associated with the quasi-one-dimensionality was a driving force in continuing the investigation of these compounds. The unusual properties of these materials do not only feature multiple charge density wave transitions [7, 8, 9, 4] but also superconductivity below 2.9 K in $LaNiC_2$ [10, 11]. Furthermore, the complex interplay between magnetism and CDWs is in the area of interest [12]. To name just a few recent fields of research, anisotropic behavior of the electrical resistivity in $LuNiC_2$ [4] has been studied, the magnetoresistance and CDW transitions deduced from temperature dependent electrical resistivity measurements of polycrystalline $YNiC_2$ are already known [13], the anisotropic magneto-transport properties of $YNiC_2$ single crystals have been examined and the magnetic, transport and specific heat properties of polycrystalline $CeNiC_2$, $PrNiC_2$ and $NdNiC_2$ are also within the scope of knowledge [14, 15, 16, 17].

The aim of this work emphasizes on studying distinctive features of rare-earth nickel dicarbides. The main focus was set on examining primary single crystalline samples, as each orthorhombic direction of the crystal exhibits a characteristic behavior regardless of whether the magnetic, electric or thermoelastic features are investigated. In polycrystals, the striking features of the material are discovered as well but the contributions of all axes fuse together and insightful information remains undeciphered. For this purpose, either already existing samples were examined or crystals were grown using the optical floating zone method. The structural changes at the phase transitions of monocrystalline $RNiC_2$ (R = Ho, Pr, Dy or Gd) and $LuNi_{0.92}Co_{0.08}C_2$ were studied with dilatometry in order to study the nature of phase transitions and to reveal elastic interactions of magnetic and charge density wave order parameters caused by spontaneous magnetostriction. With additional resistivity measurements, characteristic features of the charge density wave transitions were analyzed. In combining the structural modifications with heat capacity data, the pressure dependence of the transition temperatures of the first and second order phase transitions were estimated by applying the Clausius-Clapeyron and Ehrenfest relation. Another goal was to examine the singlet ground state of $PrNiC_2$ as spin glasses have already been discovered in other Pr compounds [18]. Extensive magnetic studies with different methods, such as AC susceptibility, the Vibrating Sample Magnetometer (VSM) and the Superconducting Quantum Interference Device (SQUID) were conducted. Furthermore, the influence of the crystalline electric field (CEF) on the degenerate ground state of $PrNiC_2$ was evaluated by fitting experimental magnetic and thermodynamic data with the single ion CEF model for localised rare earth 4f states. Another objective was to explore if the CDW in $LuNi_xCo_{1\text{-}x}C_2$ can be suppressed with the substitution of Co. Therefore, it was attempted to grow pseudo-ternary single crystals of $LuNi_{1\text{-}x}Co_xC_2$ with a Co amount between 8 % and 20 % and to find the critical point of suppression by employing resistivity, heat capacity and magnetic measurements. In some other systems, the finding of a quantum critical point lead to the observation of superconductivity. However, the fabrication of pseudo-ternary compounds proves difficulties due to a higher risk of segregation during growth and thus, inhomogeneities in the crystals arise.

This thesis is divided into seven chapters. An introduction to relevant physical concepts will be given in chapter 2. Chapter 3 will firstly cover the whole process of preparing the samples. Commencing with the preparation of rods for the crystal growth, the actual growth and the different methods to reveal the crystalline structure of the crystals. Furthermore, the measurement methods and the process of calibrating the AC susceptometer will be delineated. In the following chapter, the experimental outcomes on the suppression of the CDW in $LuNi_{1\text{-}x}Co_xC_2$ will be presented. Subsequently, chapter 5 will show the results regarding $PrNiC_2$. In chapter 6, the findings relating to the thermal expansion of the single crystals will be discussed. The findings will be summarized and motivation for future measurements will be given in chapter 7.

2 Theoretical Concepts

2.1 Thermodynamic Variables and Potentials

Every macroscopic system containing a large number of particles ($\sim 10^{23}$) and many degrees of freedom is considered as thermodynamic system. In order to characterize the system, not the microscopic but macroscopic properties are of relevance which are described with statistical theory. State variables are defined that characterize the macroscopic system and the relation between these variables unambiguously. These include the intensive variables pressure p, temperature T, chemical potential μ and the magnetic field H, as well as the extensive variables volume V, entropy S, magnetization M and number of particles N [19].

Thermodynamic potentials describe the equilibrium state of a system in relation to the natural variables. By partially deriving thermodynamic potentials with respect to the natural variables other state variables can be calculated directly. An example would be the derivative of the internal energy $U(S,V,N)$ with respect to the entropy, which is a natural variable, and at constant volume and number of particles:

$$U(S,V,N) = TS - pV + \mu N \Rightarrow \left(\frac{\partial U}{\partial S}\right)_{V,\,N} = T \tag{2.1}$$

Generally, it is easier to measure intensive variables under given conditions. With the Legendre transform an extensive variable can be replaced by its conjugate intensive variable leading to new thermodynamic potentials. By substituting the entropy with the temperature as an independent variable of U, the consequent Legendre transform is the Helmholtz free energy F which plays a key role in physics and is defined as follows:

$$F(T,V,N) = U - TS \tag{2.2}$$

Furthermore, the Gibbs free energy is given by:

$$G(T,p,N) = U - TS + pV \tag{2.3}$$

These thermodynamic potentials are connected with measured values, *e.g.* the volume or heat capacity, *via* the Maxwell relations. The first or second derivatives of these potentials yield to important measurands that are defined below.

The volume and the entropy are expressed by:

$$V = \left(\frac{\partial G}{\partial p}\right)_T \tag{2.4}$$

$$S = -\left(\frac{\partial G}{\partial T}\right)_p = -\left(\frac{\partial F}{\partial T}\right)_V \tag{2.5}$$

If heat is transferred to a material, its temperature rises. The amount of energy transferred as heat that is required to increment the temperature of a body by one degree is named heat capacity in the SI unit J/K. This relation can be described with following equation:

$$C = \frac{dQ}{dT}, \tag{2.6}$$

with the heat capacity C, the transferred heat dQ and the temperature change dT. The heat capacity per unit mass is called specific heat capacity and is material-dependent. Subsequently, the heat capacity at constant volume (C_V) and the heat capacity at constant pressure (C_p) are derived from following thermodynamic relation:

$$C_V = T\left(\frac{\partial S}{\partial T}\right)_{V,N} = -T\left(\frac{\partial^2 F}{\partial^2 T}\right)_{V,N} \tag{2.7}$$

$$C_p = T\left(\frac{\partial S}{\partial T}\right)_{p,N} = -T\left(\frac{\partial^2 G}{\partial^2 T}\right)_{p,N} \tag{2.8}$$

The circumstance of matter to change the volume with the alteration of the pressure at constant temperature is called isothermal compressibility:

$$\kappa = \frac{1}{V}\left(\frac{\partial V}{\partial p}\right)_{T,N} = -\frac{1}{V}\left(\frac{\partial^2 G}{\partial^2 p}\right)_{T,N} \tag{2.9}$$

If the pressure is kept at a constant value, the change in length is dependent on the temperature, which is designated as thermal expansion. The thermal expansion coefficient corresponds to the first derivative of the change in length with respect to temperature:

$$\alpha = \frac{1}{l}\left(\frac{\partial l}{\partial T}\right)_{p} \tag{2.10}$$

Analogously, the volume coefficient of thermal expansion, which is in relation to the compressibility, is specified as:

$$\beta = \frac{1}{V}\left(\frac{\partial V}{\partial T}\right)_{p} = \kappa\left(\frac{\partial p}{\partial T}\right)_{V,N} = -\kappa\left(\frac{\partial^2 G}{\partial p \partial T}\right)_{N} \tag{2.11}$$

The listed thermodynamic potentials and further information are provided *e.g.* in the book of Nolting [19].

2.2 Phase Transitions

A phase refers to a state of matter which can be described by definite physical and chemical properties. Different phases can be distinguished *e.g.* by their appearance or internal structures and spin orientations. A phase transition marks a transformation of a system from one phase into another phase. These phases are characterized by different sorts of symmetry, causing a spontaneous symmetry breaking at the transition. In many cases a phase transition occurs with the variation of temperature. A higher temperature goes hand in hand with a higher thermal excitation yielding to a larger number of states that can be occupied and therefore more different possibilities of configurations in a many-body system arise. This often leads to a change in macroscopic variables such as an increasing entropy and disorder. Also other external parameters like the pressure or magnetic field can give rise to phase transitions.

In 1933, Paul Ehrenfest was the first to introduce a classification of phase transitions in relation to discontinuities in the derivatives of the free energy function. If the first derivative of the free energy function with respect to a thermodynamic variable shows a discontinuity, these are named first order phase transitions. Moreover, a second order phase transition is characterized by a continuous first derivative of the free energy but a jump in the second derivative is exhibited. In contrast to second order transitions, transitions of first order are always in conjunction with the absorption or release of latent heat. An example of a first order phase transition would be the liquid-solid or liquid-gas transition. The transition from a ferromagnetic to a paramagnetic state is considered as second order transition [20].

Clausius-Clapeyron Relation

At phase transitions of first order, the Gibbs energy is a continuous function, whereas its derivatives with respect to the temperature or the pressure are discontinuous. In solids, a sudden modification of the crystalline structure can give rise to a phase transition of first order which is accompanied by abrupt changes in the volume and entropy. During this transition, if reversible, latent heat $Q = T_C \Delta S$ is absorbed or released. The Clausius-Clapeyron relation applies to first order phase transitions with the condition that the process of compression and decompression must be reversible (see *e.g.* Ref. [19]):

$$\frac{dp}{dT} = \frac{\Delta Q}{T \Delta V} = \frac{\Delta S}{\Delta V} \tag{2.12}$$

While the Clausius-Clapeyron relation has been initially conceptualized for the liquid-vapor transition, it has also been applied to various problems in solid state physics. Griza *et al.* [21] investigated the structural transition temperature of C_{60} in dependence of the pressure and subsequently concluded an upper limit of the relative change in length of the lattice parameter. The pressure dependence of the first order paramagnetic-ferromagnetic transition in Eu_2In was estimated by Guillou *et al.* [22]. The applicability of the Clausius-Clapeyron relation on a transition of first order between two CDW phases was confirmed by Wang *et al.* [23], who observed consistent results of ΔS, ΔV and dp/dT in 1T-TaS_2.

Ehrenfest Relation

At phase transitions of second order, a correlation between the specific heat, the thermal expansion coefficient and the elastic modulus exists. The interrelation between those physical quantities is described with the generalized Ehrenfest relation. A derivation of the generalized Ehrenfest relation with methods of classical and quantum mechanical approaches that would go beyond the scope of this thesis is given by Rosaler, *c.f.* Ref. [24]. Following relation applies to a second order phase transition at the transition temperature T^* (see *e.g.* Ref. [19]):

$$\frac{\partial T^*}{\partial p} = \Delta \beta V \frac{T^*}{\Delta C_\mathrm{p}} \tag{2.13}$$

For this work, only the formulation of the Ehrenfest relation of charge density wave transitions in low-dimensional metals is relevant, where in addition to pressure, see Eq. 2.13, also uniaxial strain is of interest. The behavior of the system near a critical point can be described with the Landau theory [25]. Lev Landau attempted to formulate an approximate form of the free energy without knowledge about the numerical value of the microscopic states. The system is described with an order parameter that is often defined to be zero at temperatures above the phase transition and non-zero below the critical temperature. The free energy can be considered as following power series of the order parameter Q:

$$F(T) = F_0(T) + A(T - T_\mathrm{C})Q^2 + BQ^4, \tag{2.14}$$

with F_0(T) being the temperature dependence of the high temperature phase, the critical temperature T_C and the parameters A and B, with $A > 0$ and $B > 0$. The order parameter that gives the minimal free energy is computed by:

$$\frac{\partial F}{\partial Q} = 0 = 2AQ(T - T_\mathrm{C}) + 4BQ^3 \tag{2.15}$$

Rearranging the equation yields:

$$Q^2 = \frac{AT_\mathrm{C}}{2B}\left(1 - \frac{T}{T_\mathrm{C}}\right) \tag{2.16}$$

By using the relations of the entropy and the heat capacity that were mentioned in section 2.1, the kink in the specific heat at the second order phase transition at T_C is described by:

$$\Delta C_\mathrm{p} = \frac{A^2 T_\mathrm{C}}{2B} \tag{2.17}$$

With the equations outlined in the article of Testardi [26], the specific heat jump ΔC_p is in relation to a discontinuity in the thermal expansion coefficients α_i and also correlates to the stress dependent components $\partial T_\mathrm{CDW}/\partial\sigma_\mathrm{i}$ at the critical temperature T_{CDW}:

$$\Delta\alpha_\mathrm{i} = \frac{1}{V_\mathrm{m}}\left(\frac{\Delta C_\mathrm{p}}{T_\mathrm{CDW}}\right)\left(\frac{\partial T_\mathrm{CDW}}{\partial\sigma_\mathrm{i}}\right), \tag{2.18}$$

where V_m labels the molar volume of the material and $i = a$, b or c, corresponds to the crystallographic axis in an orthorhombic crystal [27, 26, 28]. The application of the Ehrenfest relation to specific CDW transitions as expressed in Eq. 2.18 has been reviewed by Saint-Paul and Monceau [27].

2.3 Heat Capacity of Solids

The Debye model [29] gives a valid approximation of the heat capacity originating from phonons within the solid at low temperatures, known as the T^3 law. In metals, heat capacity is not only influenced by phonons, but also by electron contributions, which can be calculated with the aid of Fermi-Dirac statistics. Combining these two parts yields:

$$C = C_\mathrm{Electron} + C_\mathrm{Phonon} \tag{2.19}$$

$$C = \frac{\pi^2 N_\mathrm{A} {k_\mathrm{B}}^2}{2E_\mathrm{F}}T + \frac{12\pi^4 N_\mathrm{A} k_\mathrm{B}}{5{\Theta_\mathrm{D}}^3}T^3 \tag{2.20}$$

N_A denotes the Avogadro constant, k_B the Boltzmann constant, E_F the Fermi energy and Θ_D the Debye temperature. The Debye temperature is a material-dependent constant. It is defined as follows:

$$\Theta_\mathrm{D} = \frac{\hbar\omega_\mathrm{D}}{k_\mathrm{B}}, \tag{2.21}$$

with $\hbar$, the Planck constant divided by 2π and the Debye frequency ω_D, which represents the maximum allowed phonon frequency. Therefore, there will be no collective lattice vibration above the Debye frequency, meaning only low-energy modes are present while high-frequency modes are frozen out. Solely independent thermal lattice vibrations can exist above Θ_{D}. The Debye temperature also is an indicator of the binding strength between the atoms. The higher Θ_{D}, the stronger the atoms are bound.

The specific heat can also be described with:

$$C = C_{\mathrm{Electron}} + C_{\mathrm{Phonon}} \approx \gamma T + \beta T^3, \tag{2.22}$$

whereby γ is the Sommerfeld coefficient, which is in the range of 10^{-3} J/molK^2 for most metals. The Debye temperature at low temperatures can be evaluated with the coefficient β. For this purpose, it is convenient to plot C/T over T^2 and to extrapolate the low temperature data for $T \rightarrow 0$. A comparison with Eq. 2.20 shows, that the y-axis intercept corresponds to γ and the slope of the curve correlates to β. Hence, when inserting numbers and rearranging the equation, following relation holds:

$$\Theta_{\mathrm{D}} = \sqrt[3]{\frac{1994N}{\beta}} \tag{2.23}$$

In this context N is the number of atoms per formula unit (see *e.g.* [30, 31, 32]).

2.4 Magnetism

Magnetism is displayed by all materials in some extent and can be classified in different ways. A rough subdivision can be made between diamagnetism, paramagnetism and ferro-/antiferromagnetism, whereby each of these categories can be divided into magnetism originating from localized (quasi-bond) and delocalized (quasi-free) electrons. In rare-earths, magnetism is primary mediated through free electrons in the outer s-, p- and d-orbitals. Nonetheless, the strongly localized 4f electrons should not be neglected due to the interaction with the crystalline electric field.

The magnetic susceptibility χ is a quantity indicating the linear response of the magnetization when a material is exposed to an external magnetic field. Therefore, it is defined as the ratio of magnetization M to the intensity of the applied field H:

$$\chi = \frac{M}{H} \tag{2.24}$$

The magnitude and sign of the susceptibility gives information about the predominant type of magnetism in the material.

2.4.1 Diamagentism

Every material has a diamagnetic component but only if an external magnetic field is present. The diamagnetic response originates from fully occupied orbitals. Due to the small contribution of diamagnetism to the magnetization, diamagnetism in a material can only be observed if other types of magnetism are not present, meaning the atom has no unpaired electrons (Larmor diamagnetism). According to the quantum mechanical response of the fully occupied orbital, a material seeks to counteract an external magnetic field and as a result a magnetic field in the direction opposite to the one of the applied magnetic field is induced. Every electron acquires an extra magnetic dipole moment that is always pointed opposite to the field and $\chi < 0$. In metals, the diamagnetism of delocalized electrons is described with the model of Landau diamagnetism [31, 33].

2.4.2 Paramagentism of Non-Interacting Magnetic Moments

In contrast to diamagnetism, an external magnetic field induces a magnetization which aligns along the applied magnetic field in some materials. Paramagnetism of localized non-interacting magnetic moments only appears in atoms with incompletely filled shells and which therefore have unpaired electrons (Langevin paramagnetism). As long as there is no external magnetic field, the magnetic moments in a material are randomly distributed and average to zero. Classically, the applied field which tries to align the dipoles exerts a torque on the magnetic moment and this torque accounts for paramagnetism. For paramagnets, the susceptibility is positive and its temperature dependence is given by the Curie law:

$$\chi(T) = \frac{C}{T}, \tag{2.25}$$

with C being the Curie constant.

The Brillouin function (B_J(y)) is a quantum mechanical approach to the magnetization of a paramagnet, which considers the quantized total angular momentum (J) of the particles.

$$B_{\mathrm{J}}(y) = \frac{2J+1}{2J} * coth\Big(\frac{(2J+1)*y}{2J}\Big) - \frac{1}{2J} * coth\Big(\frac{y}{2J}\Big) \tag{2.26}$$

$$y = \frac{g\mu_{\mathrm{B}}JB}{k_{\mathrm{B}}T} \tag{2.27}$$

where μ_B is the Bohr magneton, g the g-factor, B the magnetic field, k_B the Boltzmann constant and T the temperature. A derivation of the Brillouin function is presented *e.g.* in Ref. [33].

The paramagnetism of delocalized band electrons is known as Pauli paramagnetism. In an external field, the energy bands are splitted and the energy of the electrons is raised or lowered depending on their spin state. Consequently, the density of states changes and the imbalance of up and down spins create magnetization [31, 33].

2.4.3 Ferro- and Antiferromagnetism

Long-ranging interactions between magnetic moments can give rise to a magnetic ordering of the ground state in a system. The effect is based on multiple quantum mechanical exchange mechanisms. If the exchange constant for nearest neighboring localized moments is positive, all magnetic moments are aligned and the material is ferromagnetic. The orientation is maintained despite switching off the external field, but only as long as the temperature is below a critical value. An excess of this material-specific Curie temperature (T_{C}) causes the loss of permanent magnetic properties and the material becomes paramagnetic. On the other hand, if the exchange interaction between neighboring spins is negative, the material is antiferromagnetic. The spins are ordered in a way that the nearest neighbors of one spin align antiparallel. This can be seen as a composition of two interpenetrating ferromagnetic lattices with opposite magnetization. The net magnetization sums up to zero in antiferromagnets because the magnetic moments of both sublattices have the same value. This zero net magnetization is preserved until it reaches the critical Néel temperature (T_N). As in the case of ferromagnetism, the antiferromagnet transforms into a paramagnet above this temperature. The susceptibility of metallic magnetic systems is characterized by a modified Curie-Weiss law:

$$\chi(T) = \chi_0 + \frac{C}{T - \Theta_\mathrm{p}}, \tag{2.28}$$

with a temperature independent Pauli susceptibility χ_0 and a paramagnetic Curie-Weiss temperature Θ_p.

The magnetization of itinerant interacting moments is due to a spontaneous splitting of the spin-up and spin-down band by a certain energy. The rearrangement of the spin states leads to a higher kinetic energy and thus the establishment of this spontaneous ferromagnetism is only possible, if the gain in kinetic energy is compensated by a reduction of the potential energy due to the magnetization. This condition is known as Stoner criterion.

The magnetic phase transition can be impeded by various mechanisms, *e.g.* geometric frustration, competing interactions or random interactions [31, 33].

2.4.4 Spin Glass

The term "spin glass" dates back to the 1960s, when the effect of isolated impurities in metals stirred up a lot of interest. Other than in a ferromagnetic or antiferromagnetic system, in a spin glass, no conventional long-range magnetic order can be formed. A spin glass defines a magnetic system in which a new type of order is established due to random short-range interactions of the magnetic moments. If the temperature falls below the specific freezing temperature, a typical paramagnetic state transforms into a system in which the spins seem to freeze in random orientations to each other. This established metastable state is characterized by frustration and degeneration of the ground state. Therefore, a single configuration which satisfies all interactions at the same time cannot be developed and further the potential energy cannot be simultaneously minimized. The spin glass transition is identified by a continuous freezing of the spins whereby the state of equilibrium can never be reached. Thus, this continuous transition can not be equated with a phase transition [34, 35]. A theoretical approach is given by the Vogel-Fulcher law, which provides information on the frequency dependent spin-freezing temperature and the relaxation time in a spin glass, *c.f.* Ref. [36]. Surprisingly, spin glass behavior has also been observed in Pr systems with a fully ordered regular Pr sublattice. This phenomenon has been explained as a consequence of dynamic frustration of Pr moments with a singlet ground state of the crystalline electric field where all interaction results from thermal excited states which are fluctuating and thus are randomized [37].

2.4.5 Crystalline Electric Field

The multiplet degeneracy of a magnetic orbital of a free ion is lifted by its local environment in the crystal. The electric field originating from the surrounding atoms is modelled with the crystalline electric field (CEF) theory. With this theory, the interactions between the positively charged central ion of a transition metal and the overlap with orbitals of neighboring ligands is described. The basic idea of this concept considers the non-spherical symmetry of the d and f-orbitals. As a ligand approaches to the central ion, the electrostatic repulsion depends on the relative orientation of the electrons in the d or f orbitals of the transition metal and the orbitals of the ligands. As soon as the ligands approach the metal ion, the degeneracy of the electronic states in the d or f-orbitals are lifted by the repulsive forces of their immediate surrounding. Properties of transition-metal compounds such as their magnetic features, color, structure or stability can often be explained by this model [33].

The ions of the rare-earth elements are characterized by an incompletely filled 4f-shell. Due to the 4f-orbital being the best localized orbital carrying magnetic moments in metals, it is strongly shielded from the surroundings by the completely filled 5s and 5p-orbitals. Therefore, the crystal field hardly influences the 4f electrons and can be treated as perturbation. The localized 4f orbital can be described with following Hamiltonian:

$$H = \underbrace{H_0 + H_{\mathrm{ee}} + H_{\mathrm{SO}}}_{Hund'sRuleGroundState} + \underbrace{H_{\mathrm{Ze}} + H_{\mathrm{CEF}}}_{Perturbation}, \tag{2.29}$$

with the H_0 being the energy of the electrons in a spherical, radial potential, H_{ee} symbolizes the electron-electron contribution, H_{SO} the spin-orbit coupling, H_{Ze} the Zeeman splitting in presence of an external magnetic field and H_{CEF} considers the effect of the crystal field. Whereas the first three terms label the ground state of the ion and are described with Hund's rules, the Zeeman term and the crystalline electric field act as perturbation of the free ion potential. The latter two terms lift the degeneracy of the Hund's rule ground states and thus, the effective moment is modified which can influence the magnetic ground state.

While for 3d transition metals $H_{SO} \sim H_{CEF}$ holds, for rare-earth ions, $H_{SO} \gg H_{CEF}$ applies and the corresponding magnitude of the splitting of the levels is in the range of 1000 meV $\gg$ 100 meV. This is due to the weaker influence of the crystal field on the localized 4f-electrons and additionally the spin-orbit coupling strength grows with the atomic number and the localization of the orbital. The crystalline electric field is described with the crystal potential $U(\mathrm{r}_\mathrm{i})$, which is generated by the neighboring ions:

$$H_{\mathrm{CEF}} = e \sum_{n=1}^{N} U(\mathbf{r}_\mathrm{i}), \tag{2.30}$$

with the elementary charge e. As shown by Stevens [38], this expression can be reformulated under certain assumptions and with the aid of the Wigner-Eckhart theorem:

$$H_{\mathrm{CEF}} = \sum_{l,m} B_l^m O_l^m(\mathbf{J}), \tag{2.31}$$

where $O_l^m(\mathbf{J})$ correspond to the Stevens operators in terms of angular momentum operators and B_l^m are the crystal field parameters which can be evaluated by fitting experimental data with appropriate models. Several software packages, *e.g.* *McPhase* [39], offer the opportunity to analyze the impact of the crystal field on ions. The order of Eq. 2.31 is dependent on the symmetry of the crystal system. Further reading and a detailed derivation of H_{CEF} is provided in the books of Jensen-Mackintosh [40] and Newman-Ng [41].

2.5 Charge Density Waves

The first theoretical concepts of charge density waves date back to the 1930s, when Rudolph Peierls described the mechanism of a modulation of the crystalline structure and the consequent formation of an additional energy gap in a one-dimensional chain of monovalent atoms [42]. The term charge density wave was first introduced by Herbert Fröhlich in the 1950s, who tried to explain superconductivity by electron-phonon interaction [43]. Efforts were made to extend the model of Peierls to real systems. A real one-dimensional system is actually only a quasi-1D system as in nature there exists no strict one-dimensional crystal structure. In these metals the lattice is multi-dimensional, but the electronic properties behave like in a quasi-one-dimensional material. In three-dimensional crystallographic structures, the shape of the Fermi surface indicates the quasi-dimensionality. While quasi-one-dimensional materials exhibit quasi-planar Fermi surface sheets, the energy surface in quasi-2D and quasi-3D materials reveal cylindrical and isotropic energy surfaces, respectively. Charge ordering in real low-dimensional metals are often described with the Peierls' model even though experiments have shown that the mechanism is not truly analogous for quasi-2D or quasi-3D metals, as reported in Ref. [44]. Although numerous studies on CDW systems have been conducted and theories of quasi-two-dimensional and quasi-three-dimensional materials have been set up, the origin of the CDW phase transition is still disputed. Different classifications of CDWs have been proposed, *e.g.* in the Review by X. Zhu [45], in categorizing them by their dimensionality but without clear definitions of the origin of their CDW states. The underlying mechanisms in one-dimensional conductors are consistent with the metal-to-insulator transition in the Peierls' picture [46]. The second type of CDWs considers two-dimensional materials in which the CDW phases are solely induced by the electron-phonon-coupling and no metal-to-insulator transition is observed [47]. It becomes even more complicated in 3D systems. Due to interplanar interactions, a complex three-dimensional character of the CDWs is observed in these metals [48]. Charge density waves in cuprates are considered as separate type as the connection of superconductivity and the formation of CDWs is discussed [1, 27, 44, 45, 49].

The model of CDWs introduced by Peierls was exemplified with a one-dimensional chain of monovalent atoms. The atoms of the chain are equally spaced with a lattice constant a above T_{CDW} as in the left illustration on top in Fig. 1. In the sketch below, the free electron band structure with gaps at the edge of the Brillouin zone $k = \pm\frac{\pi}{a}$ is shown. The energy band is half filled and states with energies less than E_F and wave vectors less than k_F will be occupied. On the other hand, all states above these Fermi points will be empty. Below T_{CDW}, a modulation of the electron density causes the formation of a charge density wave with a periodicity of $2a$. In real space, the lattice periodicity has doubled, causing the production of an energy gap at the Fermi surface $k = \pm k_\mathrm{F} = \pm\frac{\pi}{2a}$, demonstrated in Fig. 1 on the right [14]. Also, the geometry of the Fermi surface contributes to the formation of a CDW. If parallel regions of the Fermi surface can be connected by the same wave vector, the modulation of the lattice is particularly favorable. Gaps in the Fermi surface are created at these "nested" positions if the energy gain due to the formation of the gaps overcomes the energy cost from the additional strain arising from the lattice modulation. A charge density wave is formed and the redistribution of atoms move the boundary of the Brillouin zone to k_F. The energy of the filled states will be lowered and the one of the empty states will be lifted. Consequently, in the Peierl's model a metal-to-insulator transition occurs which has a purely electronic origin. The formation of a CDW is not only driven by this so-called Fermi surface nesting. Instead, a decicive factor for the alteration of the lattice is the electron-phonon interaction. The periodicity of the CDW is determined by the Fermi surface and thus the wave vector does not inevitably have to be a rational fraction of the undistorted lattice vector. The consequential ordered crystalline phase is "incommensurate". In some materials, the modulation periodicity is temperature dependent and the incommensurate state may not be the lowest possible ground state. At lower temperatures, the wave vector of the distortion may be lock-in to a value that is an integral fraction of the underlying parental lattice and thus the lattice may undergo a "commensurate" phase transition. Therefore, two transitions can be associated with charge density waves. The normal to incommensurate phase transition is of second order and the incommensurate to commensurate transition is of first order. They can be distinguished by analyzing the lattice distortions with diffraction techniques, *i.e.* with neutrons, electrons or X-rays [14, 44, 50]. In modern theoretical approaches, the phenomenon of charge density waves is often described with *e.g.* the Lindhard function [2] or Overhauser's theory [51].

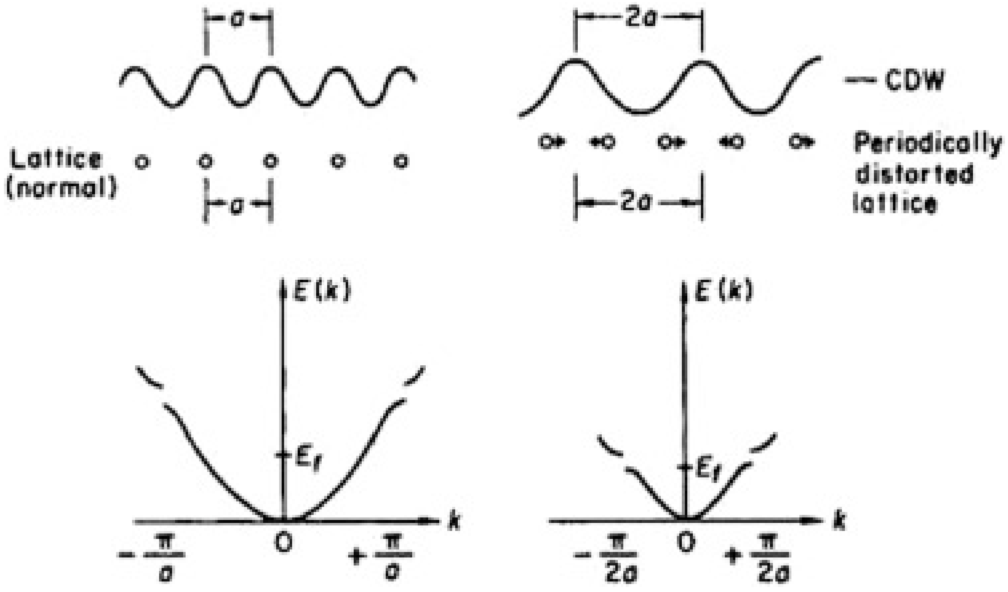

Figure 1: Left: Quasi-one-dimensional lattice with uniformly spaced atoms and the corresponding energy band. Right: Modulation of the atomic positions and energy band gap. Taken from Ref. [44].

3 Experimental Techniques

3.1 Sample Preparation

3.1.1 Radio-Frequency Induction Heating

In order to prepare sample rods for the crystal growth in the optical floating furnace, radio-frequency (RF) induction heating is used. The polycrystalline $\mathrm{RNiC_2}$ starting material was prepared by Roman [52] and in case of $\mathrm{LuNi_{1\text{-}x}Co_xC_2}$ by Levytskyy [53] *via* arc-melting technique. Prior to the melting procedure, the copper gutters, called boats, are filled with polycrystalline pieces of the desired material. Either remains of already melted rods, multiple balls of rare-earth nickel dicarbides, *c.f.* Fig. 2a, or a mixture of both were merged together for the purpose of this thesis. The copper boats are enclosed by a quartz cylinder. During the RF heating, the cylinder is flooded with an inert gas, *i.e.* argon, which prevents the unwanted reaction of the sample with oxygen. The gutter and the cylinder can be jointly shifted from left to right intending to move the loaded boats inside the coil, where the actual melting process is taking place. A high-frequency generator gives rise to time-varying magnetic fields within the coil, inducing alternating currents inside the conducting sample in the copper boats. The flow of current causes the sample to heat up and thereby to melt. The aim is to obtain rods with an homogeneous distribution of the components of the material. This is achieved by rotating, as well as flipping the rod after each melting procedure. Furthermore, a few new balls are added each time after melting in order to attain the suitable length of the rods. Another method to improve the homogeneity is to move the gutter back and forth repeatedly and slowly reduce the power of the generator when the balls are already melted together and the inside of the rod is still liquid while the outer shell is solidified by that time. One of the prepared rods is shown in Fig. 2b.

During this thesis, rods of $\mathrm{LuNi_{0.8}Co_{0.2}C_2}$, $\mathrm{LuNi_{0.86}Co_{0.14}C_2}$, $\mathrm{HoNiC_2}$ and $\mathrm{GdNiC_2}$ were prepared. It has to be mentioned that the $\mathrm{LuNi_{0.86}Co_{0.14}C_2}$ rods were prepared by melting together a 1:1 mixture of remains of $\mathrm{LuNi_{0.8}Co_{0.2}C_2}$ rods and $\mathrm{LuNi_{0.92}Co_{0.08}C_2}$ rods. The rods were cut into smaller pieces with pliers and were alternately placed into the copper boat to ensure adequate permutation. Inevitable small errors in the Ni/Co stoichiometry may be present due to imbalances of the mass ratio and crumbs that splintered off by multiply cutting the rods. Further analysis, *e.g.* by powder diffraction, could give the exact composition of the material. However, it is expected that the inequality of the mass ratio is significantly low and therefore does not alter the course of the experiments.

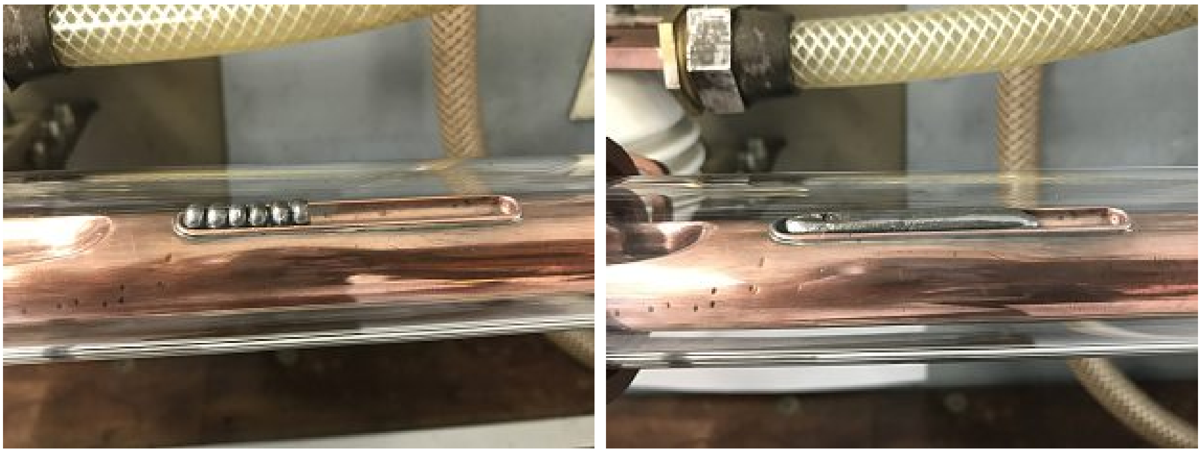

(a) (b)

Figure 2: a) $HoNiC_2$ balls inside the copper boat. b) Resulting rod after multiply adding balls and melting them together.

3.1.2 Optical Floating Zone Furnace

The optical floating zone crystal growth is based on light heating. The key components of the furnace are four high-powered bulbs and parabolic mirrors, focussing the light on two vertically mounted sample rods in the center of the furnace. An image of the inside of the used furnace by *Crystal Systems Corporation* including the rods is given in Fig. 3. If the heat provided by the bulbs is sufficiently high, a molten zone is created. Ideally, the molten zone should be in the contact zone of the bottom seed crystal and the feed crystal, which is hanging above. The two rods are encased in a quartz cylinder filled with argon gas. Apart from the initial pressure and the power which the bulbs are operated with, the rotation and vertical movement of one or both rods is a controllable parameter during crystal growth. The latter two parameters assure mixing and additionally, a more homogeneous temperature distribution in the molten zone [54].

During this thesis, two ternary single crystals, $HoNiC_2$ and $GdNiC_2$, were successfully grown. These crystals are shown in Fig. 4a and 4b respectively. Moreover, it was attempted to grow pseudo-ternary solid solutions, which is of course more challenging than growing ternary compounds. Two $LuNi_{0.8}Co_{0.2}C_2$ crystals, which are shown in Fig. 4c and 4d and one $LuNi_{0.86}Co_{0.14}C_2$ crystal, *c.f.* Fig. 4e, were grown. There has been conjecture that the Co concentration that is needed to suppress the CDW transition is in the range of 14 % to 20 %. Hence, motivation was given to grow monocrystalline $LuNi_{1\text{-}x}Co_xC_2$ crystals and to discover superconductivity.

In Fig. 5, different stages of the crystal growth in the optical floating zone furnace are shown. All crystals were grown in an argon atmosphere. The power of the light source and the movements of the shaft were adjusted to the individual growth behavior of each crystal. Whereas the $LuNi_{0.8}Co_{0.2}C_2$ rods of the first growth started to melt at 63% of the power of the four 1000 Watt light bulbs, the molten zone of the second growth was established at 60.6%. It has to be mentioned that the mirrors were cleaned between the these two growths, probably causing the needed power to diminish. The melting point of $LuNi_{0.86}Co_{0.14}C_2$ was at a similar temperature, namely at a power of 60.5%. The

Figure 3: Optical floating zone furnace with sample rods.

$HoNiC_2$ rods started to melt at a power of 54.8% and $GdNiC_2$ had the lowest melting point. Hereby, a power of 53% was sufficient to initiate the growth of the crystal. All operations and occurrences during each growth were documented and are summarized in the Appendix.

All in all, it is found that a slow and steady growth leads to the most promising results of a monocrystalline structure. During the growth of the pseudo-ternary crystals, a further difficulty due to the dependence of the local Ni/Co composition was introduced. A segregation of the Ni/Co composition lead to different melting points and the molten zone consisted of a mixture of liquid and solid chunks that could not be equilibrated again. It was one of the first times that these pseudo-ternary solid solutions were grown. Therefore, there was no possibility to rely on experience on how to prevent the segregation.

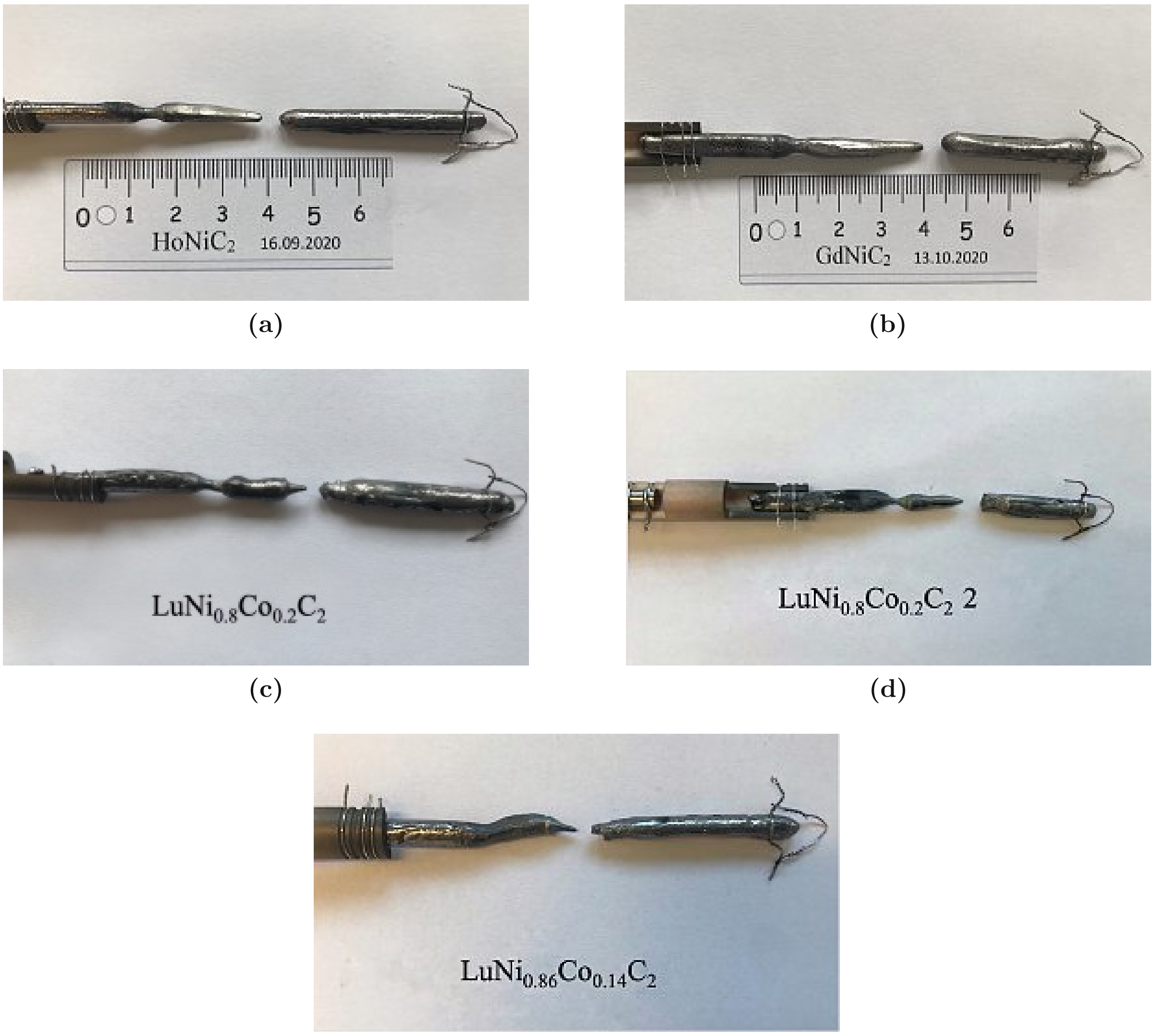

(a) (b) (c) (d) (e)

Figure 4: All grown crystals: a) $HoNiC_2$, b) $GdNiC_2$, c) first and d) second attempt to grow monocrystalline $LuNi_{0.8}Co_{0.2}C_2$ and e) $LuNi_{0.86}Co_{0.14}C_2$.

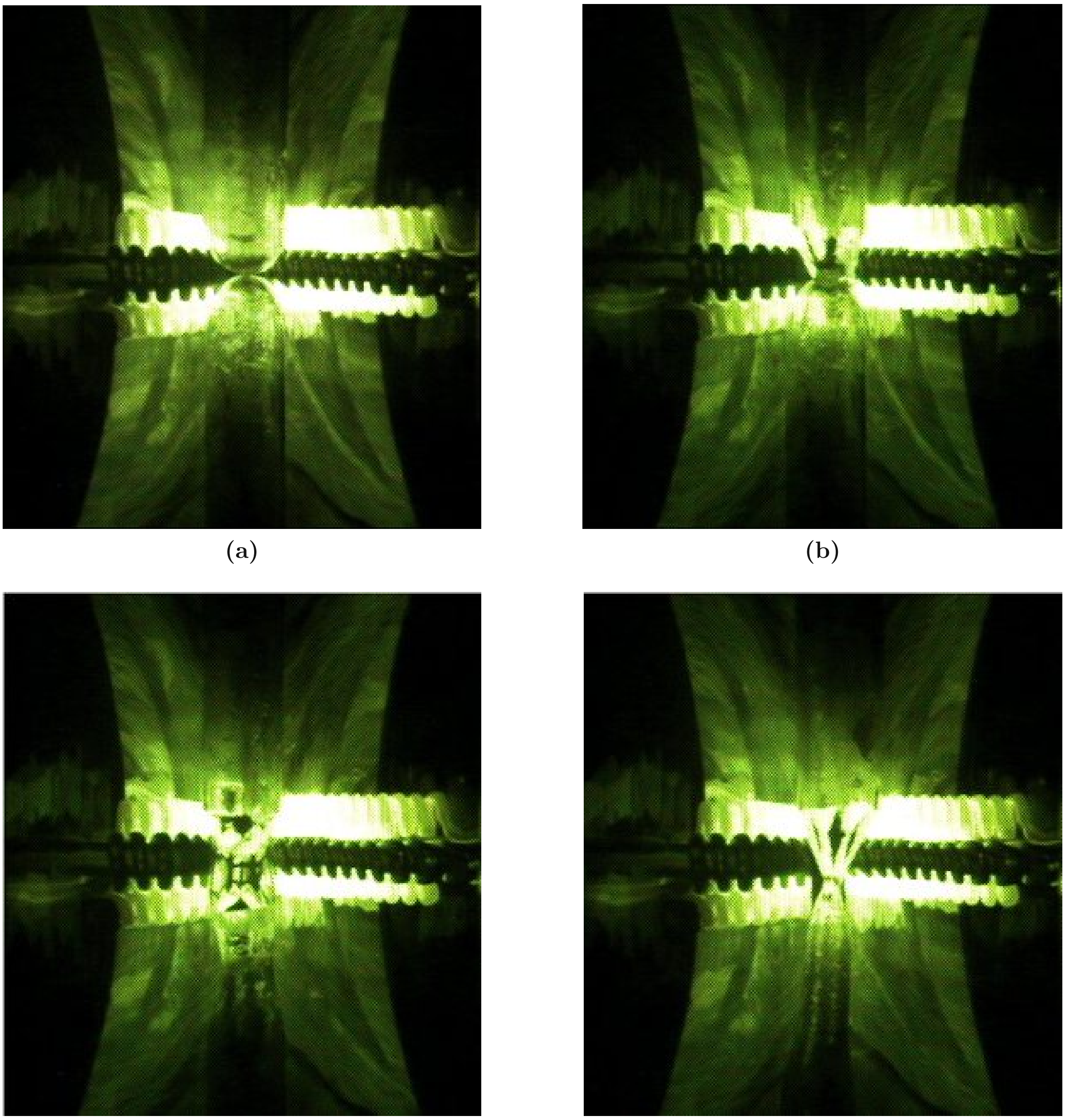

(a)

(b)

(c)

(d)

Figure 5: Stages of the crystal growth in the optical floating zone furnace: a) Shortly before the establishment of the molten zone. b) Necking. c) Growth of the single crystal. d) Shortly before finishing the growth.

3.1.3 Polarized Light Microscopy

A commonly used method to get a first impression of the internal structure of the crystal after growth is polarized light microscopy. Beforehand, a desired surface of the crystal has to be polished until it appears to be as smooth and reflecting like a mirror. This was done with a grinding and polish equipment by *Struers*. Due to their high sensitivity to water, the rare-earth nickel dicarbide samples were only polished with ethanol.

The principle of this microscopy technique is based on examining the sample surface with polarized light. Unpolarized light from a light source such as a bulb can be polarized by passing a filter that only lets through light oscillating in a specific plane, called polarizer. As soon as the polarized light impinges onto the sample, it can be altered in different ways, *i.e.* due to absorption or refraction. A second filter, the analyzer, which is placed between the objective and eyepiece is used to analyze the changes of the initially polarized light wave. Optically isotropic media, such as crystals with a cubic or periodic structure, show uniform optical behavior that is independent of the direction. As opposed to that, in anisotropic materials the orientation of incident light in dependence to the crystal orientation determines its optical properties. Changes in color or brightness may be visible when either the anisotropic material or the analyzer is rotated as a consequence of the varied orientation of the sample in the light path [55]. Different colors are a result of selective absorption of distinctive color components of white light which is linked to the crystallographic orientation of the crystal [55, 56].

In the photos in Fig. 6, segments of the two $LuNi_{0.8}Co_{0.2}C_2$ crystals grown in the optical floating zone furnace are shown. The different colors indicate a polycrystalline structure of the samples. The visible dark stripes are usually an indication of oxicarbides, which is an transparent crystalline phase that breaks during the polishing.

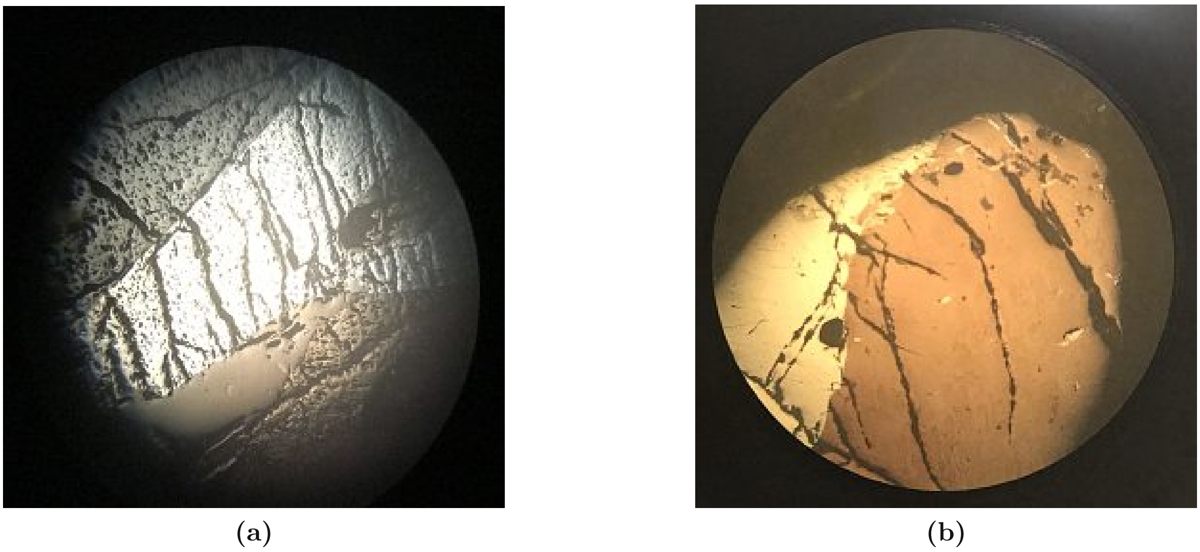
(a) (b)

Figure 6: Segments of the a) first and b) second $LuNi_{0.8}Co_{0.2}C_2$ crystal under the polarized light microscope.

3.1.4 Laue Diffraction

A more detailed information about the crystalline orientation of a sample can be revealed by Laue diffraction. This method is named after Max von Laue who was the first one to proof the wave nature of X-ray radiation by observing its diffraction on crystals [57]. In 1914, he was awarded with the Nobel Prize for this achievement [58].

The Laue method is used to identify the orientation of single crystals. A continuous X-ray spectrum is used to examine the crystal, whose lattice planes are in a fixed angle to the incoming X-rays. A detector film, which can either be placed between the crystal and the X-ray source or behind the crystal, detects a set of diffracted beams. These beams correspond to the internal symmetry of the crystal and are responsible for the formation of spot patterns that lie on curves on the detector film. Each spot correlates to a certain set of planes of the crystal that satisfies Bragg's law for the given angle between the incoming X-rays and the lattice planes. A diffraction pattern consisting of multiple dots can be identified if several sets of planes conform to the diffraction condition.

The underlying Bragg equations describe the diffraction of X-rays in a crystal lattice with translation symmetry and are a simplification of the Laue equations. They were discovered by William Henry Bragg and his son William Lawrence Bragg. For their effort, the two physicists were honored with the Nobel Prize of Physics in 1915 [59]. Experimentally, an X-ray diffraction spot is detected if constructive interference takes place. The principle is Bragg's law, illustrated in Fig. 7, which separates the planes of atoms by distances d and assumes that the incident X-ray is partially reflected at each of these planes. The beam impinges onto the sample at an angle θ and constructive interference only occurs if the path difference between the reflected beams $n\lambda$ is equal to $2dsin\theta$, with n an integer number that corresponds to the order of the reflex [31].

$$n\lambda = 2dsin\theta \tag{3.1}$$

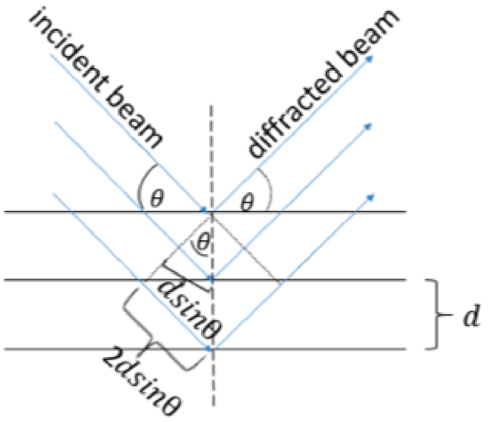

Figure 7: Illustration of Bragg's law.

Two examples of diffraction patterns produced during this master thesis by Laue method are given in Fig. 8. In Fig. 8a, an oriented single crystalline $HoNiC_2$ piece is depicted

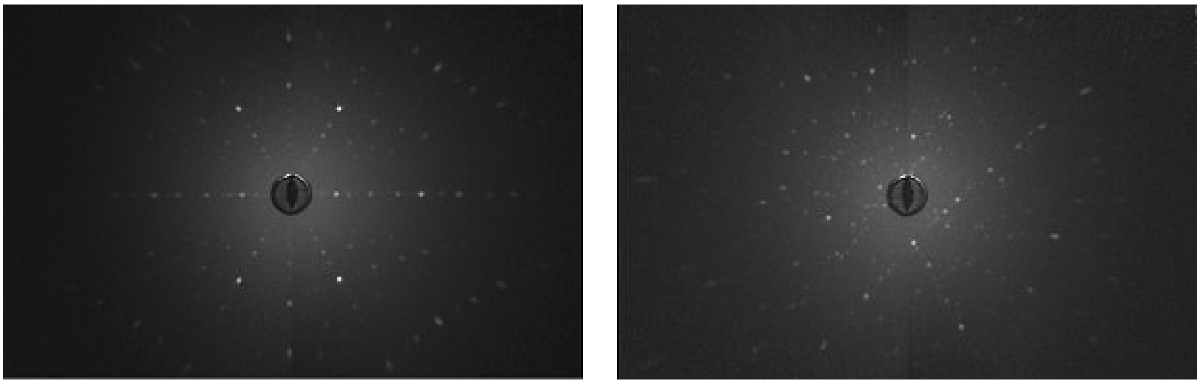

(a) (b)

Figure 8: Diffraction patterns of a) the grown $HoNiC_2$ and b) the first $LuNi_{0.8}Co_{0.2}C_2$ crystal.

and as comparison, in Fig. 8b the pattern of the first grown $LuNi_{0.8}Co_{0.2}C_2$ with no clear orientation is shown.

The software *Orient Express* [60] was used to determine the orientation of the crystal from the obtained image and then, subsequently, to adjust the orientation for cutting an appropriate sample for the measurement. After completing a data sheet with the lattice constants of the material and other parameters, such as the distance between the X-ray source and the sample, the measure of the image and the origin of the X-ray source are defined. Next, striking diffraction spots are selected and with the aid of the program, the orientation of the crystal is detected. The axes can be reoriented with the software, providing angles that enable the tuning of the goniometer onto which the sample is placed.

3.1.5 Cutting of the Samples

The cutting of the rare-earth nickel dicarbides was performed with a *Buehler* IsoMet Low Speed Saw. The saw blade is made of copper coated with diamonds and due to the water sensitivity of the samples, *IsoCut Fluid*, which is an an oil based coolant, is used during cutting. Prior to the cutting, the samples were glued to a brass block either with *Loctite* superglue or a two-component adhesive. Additionally, the apparatus is equipped with a micrometer screw to precisely cut samples with the required dimensions.

3.2 Measurement Methods

3.2.1 Electrical Resistivity

The principle of measurement is based on quantifying the voltage drop at constant current flow. With given dimensions of the sample, the specific electrical resistivity is determined in Ωm. The electrical resistivity measurements were performed with the DC resistivity option of a standard 9 T Physical Properties Measurement System (PPMS) by *Quantum Design*.

Sample Preparation and Mounting

Firstly, the examined samples were cut into bars as described in section 3.1.5 and the dimensions of the bars were determined with a micrometer screw. The bars were contacted using a four-spot welding technique with 50 μm thick gold wires. The spot welding was performed with a power of 0.38 kW and a duration of 0.32 ms. The applied current flows from I_+ to I_- and the potential difference is measured between V_+ and V_-. The welding spots were made firm with a two-component silver adhesive which was indurated in the baking oven. The samples then were attached to a sample holder called puck using a low-temperature adhesive. Prior to that, cigarette paper was glued between the sample and the puck to electrically insulate the sample from the surface of the puck. Lastly, the gold wires were connected with the puck utilizing tin-solder and the distance between V_+ and V_- was determined. An illustration of the spot welding contacts is shown in Appendix A.1. Furthermore, a list of the resistivity measurements is given.

In Fig. 9, the resistivity bar of the first grown $LuNi_{0.8}Co_{0.2}C_2$ crystal mounted to the DC resistivity puck is shown.

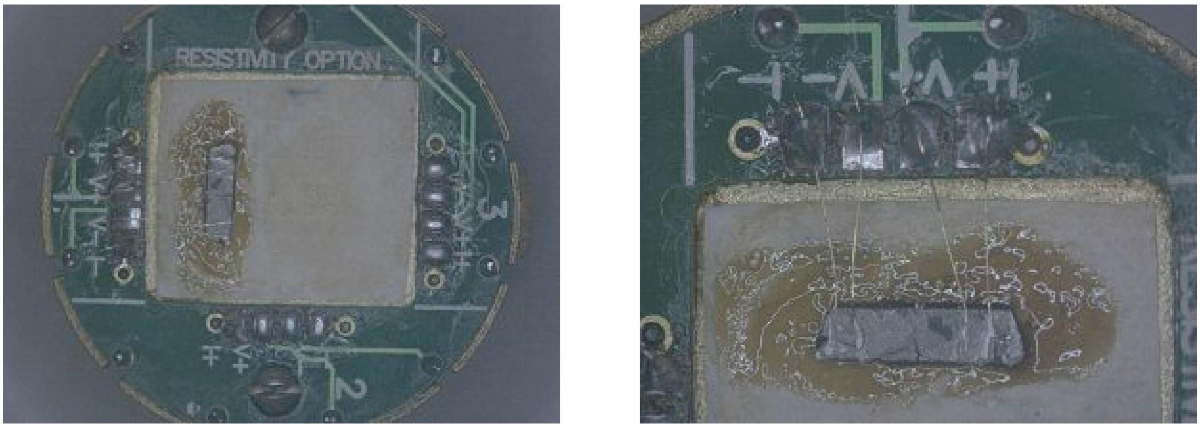

(a) (b)

Figure 9: a) Mounted $LuNi_{0.8}Co_{0.2}C_2$ sample. b) Close-up of the contacts on the sample.

3.2.2 Heat Capacity

The heat capacity of solids has already been defined in relation to thermodynamic potentials in Eq. 2.8. There are various different measurement techniques to attain the heat capacity of a sample. Nonetheless, the underlying measurement principles are similar. A known amount of heat is transferred to the sample and the change in its temperature is monitored. The heating can be realized *e.g.* by an electric heat pulse with a specific duration. Measuring the heat capacity in high vacuum ($p \to 0$), is often referred to as isobaric heat capacity (C_p) [61].

The measurements were conducted with the Helium-3 and Helium-4 heat capacity options of a Physical Properties Measurement System (PPMS), employing a relaxation type method. One measurement cycle consists of heating the sample platform for a certain time and consequently cooling it. The temperature response of the sample platform is collected and fitted to a model in a way that the specific heat of the sample is obtained. A more detailed explanation of this procedure is given in Ref. [62]. Besides, the heat capacity of one sample was additionally measured with an adiabatic calorimeter [63], employing the pulse heating technique introduced by Walther Nernst.

Sample Preparation and Mounting

As a first step, the weight of the sample is determined. For the measurement with the PPMS, a specific sample holder, called calorimeter puck, is used. Prior to mounting the sample onto the puck with *Apiezon* grease, an addenda measurement is essential to determine the heat capacity of the sample holder and the *Apiezon*. Hence, the contribution of their heat capacity can be subtracted from the total heat capacity. Schematics of the sample holder are shown in Ref. [62].

To measure the heat capacity with an adiabatic calorimeter, the sample does not need to have a specific shape as long as one side is flat. The flat side is slightly roughened with sand paper and attached to the sample holder with *Apiezon* grease. The sample holder is then enclosed with a brass covering and sealed with an indium wire. In Appendix A.2, the conducted measurements are listed.

3.2.3 Thermal Expansion

A definition of the thermal expansion has already been given in section 2.1 and the thermal expansion coefficient has been defined in Eq. 2.10. The earliest developed techniques to measure the thermal expansion of matter rely on mechanical dilatometry. Modern methods to study the change in length of a sample include optical or electronic measurement principles. Moreover, the evaluation of the crystal lattice parameter of a material at different temperatures with X-rays, electrons or neutrons gives an insight into the change of the atomic spacings inside a sample. A dilatometer that is based on determining the thermal expansion by measuring alterations in the capacitance, is the most sensitive instrument. Commonly, these dilatometers consist of two parallel plate capacitors with one moveable plate while the other one is stationary. The sample is placed between these plates and an elongation of the sample will cause the gap between the plates to enhance. Due to the inverse relation of the capacitance and the size of the gap, the change in length of the sample can be evaluated.

A custom-made miniature capacitance dilatometer was used for the thermal expansion measurements that are presented in this thesis. It consists of a plate capacitor with tilted plates. While one of the plates is moveable, the other one is fixed. A schematic drawing of the capacitance dilatometer with tilted plates is shown in Fig. 10. The dilatometer cell consists of two main parts and is primarily made of silver, due to its high thermal conductivity. The sample cube is placed onto a small sapphire washer, which serves for the purpose to electrically isolate the capacitor plates in the case of a conducting sample. For each measurement, an appropriate silver spacer, which is dependent on the side length of the sample that is examined, has to be chosen to ensure the fixation of the two capacitor plates without contact to each other. If the length of the sample alters, one capacitor plate is tilted which leads to a change of the gap, or more precisely, the inclination between the two plates. Hence, the capacity is modified which is inversely proportional to the size of the gap. The capacity is measured with a high-precision capacity bridge (Andeen Hagerling 2500 A 1 kHz Capacity Bridge) and the change in capacity originating from thermal expansion comprises four different contributions, as stated in Ref. [64]. These include the change of the radii of the capacitor plates as a function of temperature, as well as of the silver plate holders and of the length of the sample. Additionally, the change of thickness of the capacitor plates and the sapphire washers do have an influence on the measured capacity. With the aid of the obtained capacity C(T), the distance between the tilted capacitor plates d(T), *c.f.* Fig. 10, is calculated with the following equation:

$$C(T) = \frac{2\epsilon_0}{d(T)}\left[A_0(T)\frac{(1-\sqrt{1-{\gamma^2}_0})}{{\gamma^2}_0} - A_\mathrm{i}(T)\frac{(1-\sqrt{1-{\gamma^2}_\mathrm{i}})}{{\gamma^2}_\mathrm{i}}\right], \tag{3.2}$$

whereby ϵ_0 is the vacuum permittivity and in γ_0 and γ_i, the radii of the capacitor plates and the distance b between the center of the capacitor and the pivot, *c.f.* Fig. 10, are contained. Moreover, in these two parameters the thickness of the sapphire washers and literature values of the thermal expansion of silver ($\Delta l_\text{Ag-Lit}/l$ (T)) and sapphire are included as well. The parameters A_0(T) and A_i(T) denote the inner and outer capacitance area in dependence of the temperature. After numerically computing the variable d(T) for all measured temperatures, the change in length of the sample

$\Delta l_{\text{Sample}}/l$ (T) is evaluated with the following relation:

$$\frac{\Delta l_{\text{Sample}}}{l}(T) = \frac{\Delta d_{\text{Sample}}}{l_{\text{Sample}}}(T) - \frac{\Delta d_{\text{Ag-Sample}}}{l_{\text{Ag-Sample}}}(T) + \frac{\Delta l_{\text{Ag-Lit}}}{l}(T), \tag{3.3}$$

with $\Delta d = d(\text{T}) - d(\text{T}_0)$, $\Delta d_{\text{Sample}}(\text{T})$ being the measurement of the examined sample and $\Delta d_{\text{Ag-Sample}}(\text{T})$ being the measurement of a silver sample used for calibration. The absolute resolution of the dilatometer is around 1 Å. In Ref. [64], the custom-made dilatometer, its advantages and calibration are elucidated in greater detail.

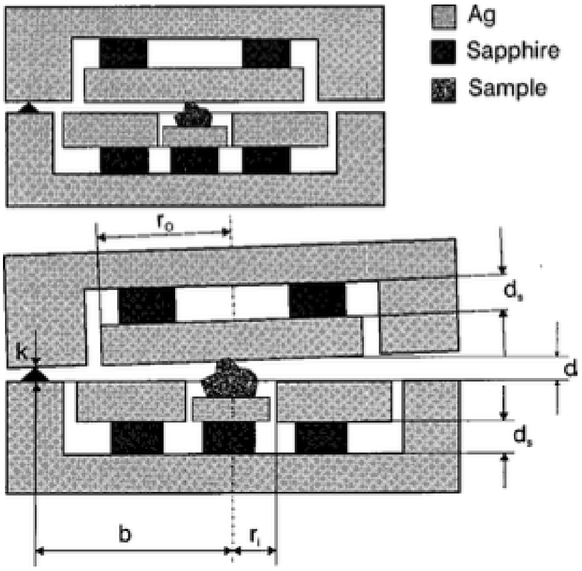

Figure 10: Schematic drawing of the custom-made miniature capacitance dilatometer with tilted plates. Adapted from Ref. [64].

Sample Preparation and Mounting

The aim was to analyze the thermal expansion and the influence of the different phase transitions the intermetallic rare-earth crystals undergo during the measurement. For that reason, single crystalline cubes were cut with a *Buehler* IsoMet Low Speed Saw. After ascertaining the dimension of the cube, the sample was placed onto the sapphire washer and it was ensured that the cube sits stable on the washer and cannot tilt. The suitable silver spacer and the upper part of the dilatometer cell was put on top. Having fixed the sample inside the dilatometer cell, it was attached to the sample holder with the corresponding ports needed to read out the measured signals. In Fig. 11, the mentioned custom-made miniature capacitance dilatometer is shown. In panel a) the sample has already been mounted and the second half of the silver cell was put on top and in panel b) the part with the sapphire plate where the sample is placed onto is presented. To get the dilatometer cell in panel a) ready for attaching it to the rest of the sample holder, one nut has to be used to fix the two parts of the cell and the coax cable has to be soldered to the visible solder joint.

The performed measurements and the corresponding dimensions of the single crystalline cubes are summarized in Appendix A.3.

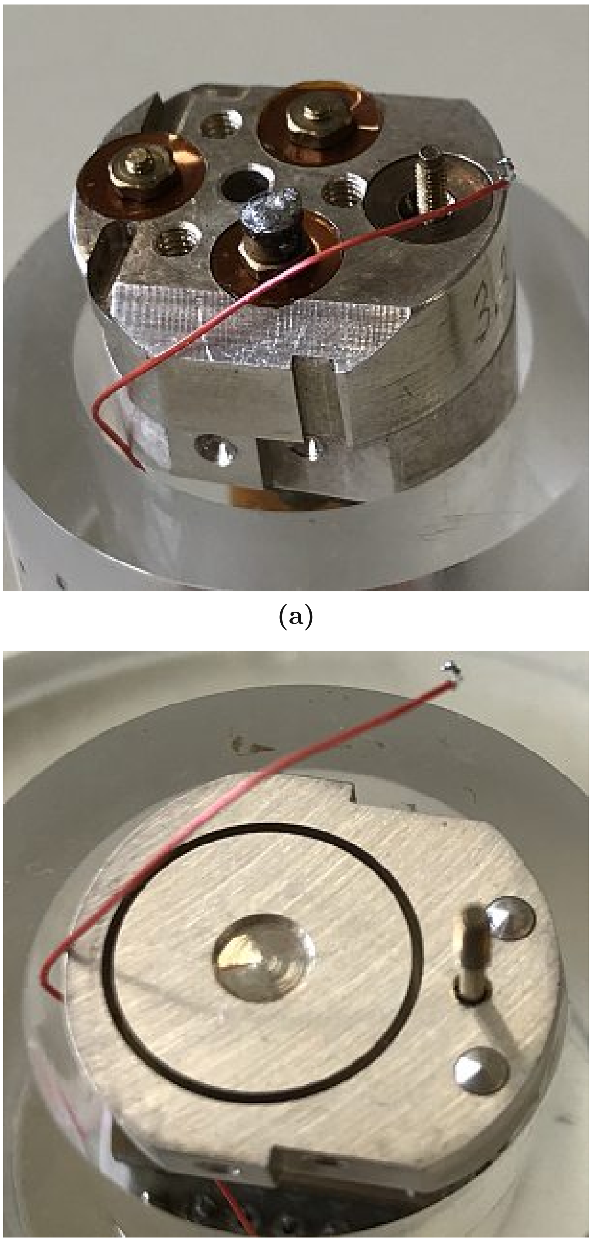

(a)

(b)

Figure 11: a) View onto the closed dilatometer cell and b) onto the opened miniature dilatometer cell with the sapphire plate in the middle.

3.2.4 Magnetic Measurements

There are two main classifications for the acquisition of the magnetic properties of a material. The Faraday balance is an example of the force method. A sample is attached to a balance and placed between the poles of a magnet with known field gradient. Due to the magnetic field, the specimen experiences a force. By comparing the mass of the sample with and without the influence of the external magnetic field, its magnetic susceptibility can be determined. The force can also be quantified with the use of a pendulum or a cantilever. The second category are induction measurements, including for example the Vibrating Sample Magnetometer and the AC Susceptometer, which were used to explore the magnetic features of the samples mentioned in this thesis. These techniques are based on inducting a voltage or current in a pick-up coil by altering the magnetic flux. A more detailed explanation will be given below. The most sensitive magnetometer, which is based on superconducting Josephson tunneling effects and was also used during this thesis, is the Superconducting Quantum Interference Device. In 1973, Josephson was rewarded with the Nobel Prize for his theoretical predictions of supercurrent flowing through a tunnelling barrier [65].

Vibrating Sample Magnetometer

With the VSM option, the PPMS by *Quantum Design* operates as sensitive DC magnetometer. In general, it consists of a motor to control the oscillation of the sample, a coil-set puck as sample holder and electronics for the motor and detecting the induced voltage in the pickup coils. The basic concept of the measurement is placing the sample in a homogeneous magnetic field, created by a superconducting primary coil, and oscillating it sinusoidally in the near of a pickup coil. The sample is magnetized in the homogeneous field and as the sample is moved up and down, a change of the magnetic flux emerges which, according to Faraday's law, will induce a voltage in the pickup coil that is proportional to the magnetic moment of the sample. A lock-in amplifier technique is used for signal detection. In this manner, the magnetization at constant temperature and changing external field, $M(\mathrm{H})$, or the magnetization at constant field and alternating temperature, $M(\mathrm{T})$, can be determined. Additional information can be received from Ref. [66].

To mount the sample, the single crystalline cube is placed into the sample holder which is made out of brass and two quartz cylinders are added. For a better grip in the sample holder, two small circular pieces of paper which fitted perfectly into the sample holder are glued on top and at the bottom of the crystal with *Loctite* superglue. A symbolic sketch of the brass sample holder and the following standard procedure of measuring the offset and can be looked up in Ref. [66].

In Appendix A.4, the conducted measurements are listed and a photo of the mounted cube is shown.

Superconducting Quantum Interference Device

The used SQUID is a standard commercial instrument operating as DC magnetometer likewise the VSM. The advantage of a SQUID over a VSM is the higher sensitivity and measurement accuracy, making it possible to measure hysteresis loops in small external magnetic fields. The operating mode of a SQUID is based on macroscopic quantum effects which only appear in superconducting materials and superfluid helium. This involves the tunnelling of Cooper pairs through thin electrically isolating or normally conducting material (Josephson junctions) without a voltage drop. Secondly, the flux within a superconducting ring is quantized, meaning the magnetic flux in a superconducting loop can only be altered in discrete steps, in fact in multiples of the flux quantum. For the measurement, a sample is moved through detection coils that are connected with the SQUID via superconducting wires and that are located in a liquid-helium-cooled chamber between magnets. The change of flux is precisely detected *via* a feedback circuit. A detailed description of the underlying physical mechanisms is provided in Ref. [31, 67, 68].

To install the sample in the SQUID, it is glued to a custom-made sample holder with *Loctite* superglue at a certain distance (5 cm) from one end of the sample holder. This ensures the correct position of the sample with respect to the pickup coils. A picture of one mounted sample is shown in Appendix A.4, as well as a list of the measured samples.

AC Susceptometer

Dynamic magnetic effects can be revealed by an AC susceptibility measurement which could remain undiscovered in a DC susceptibility measurement. The susceptibility measurements were carried out with a modified *LakeShore* Model AC 7000. Due to damages of the central control unit of the original commercial measurement instrument, Georg Binder elaborated a modified instrumentation and a new software to restore the complete functionality of the measurement system [69].

The cryostat consists of three chambers lying in one another to ensure thermal isolation. In the sketch in Fig. 12, the setup of the AC susceptometer is shown. The outermost chamber functions as dewar to isolate the experimental setup from environmental influences. Inside, the helium chamber is situated. The chamber can be filled with helium in order to serve as thermal bath. The primary coil is located in the innermost chamber, also referred to as vacuum chamber. A magnetic field is generated by an alternating current that flows through the primary coil with defined frequency and amplitude. On the inside of the primary coil, two identical pick-up coils with opposite windings are installed. The sample holder is mounted inside a sapphire cylinder which is surrounded by these coils. The heater for the temperature control is also attached to the cylinder [69].

A graphic of the cross-section of the vacuum chamber is given in Fig. 13. An alternating current flows through a primary coil and gives rise to a magnetic alternating field. The resulting time-dependent magnetic moment of the sample induces a current in a secondary pickup coil which can be evaluated without a motion of the sample. The used susceptometer consists of two pickup coils and during the measurement, the sample is consecutively positioned in the midst the upper or the lower coil with a stepper motor. In this way, the compensation of voltages which are generated by perturbations or the alternating magnetic field is possible. Due to losses originating from the remagnetization of the sample and eddy currents, the sample magnetization and the generated magnetic

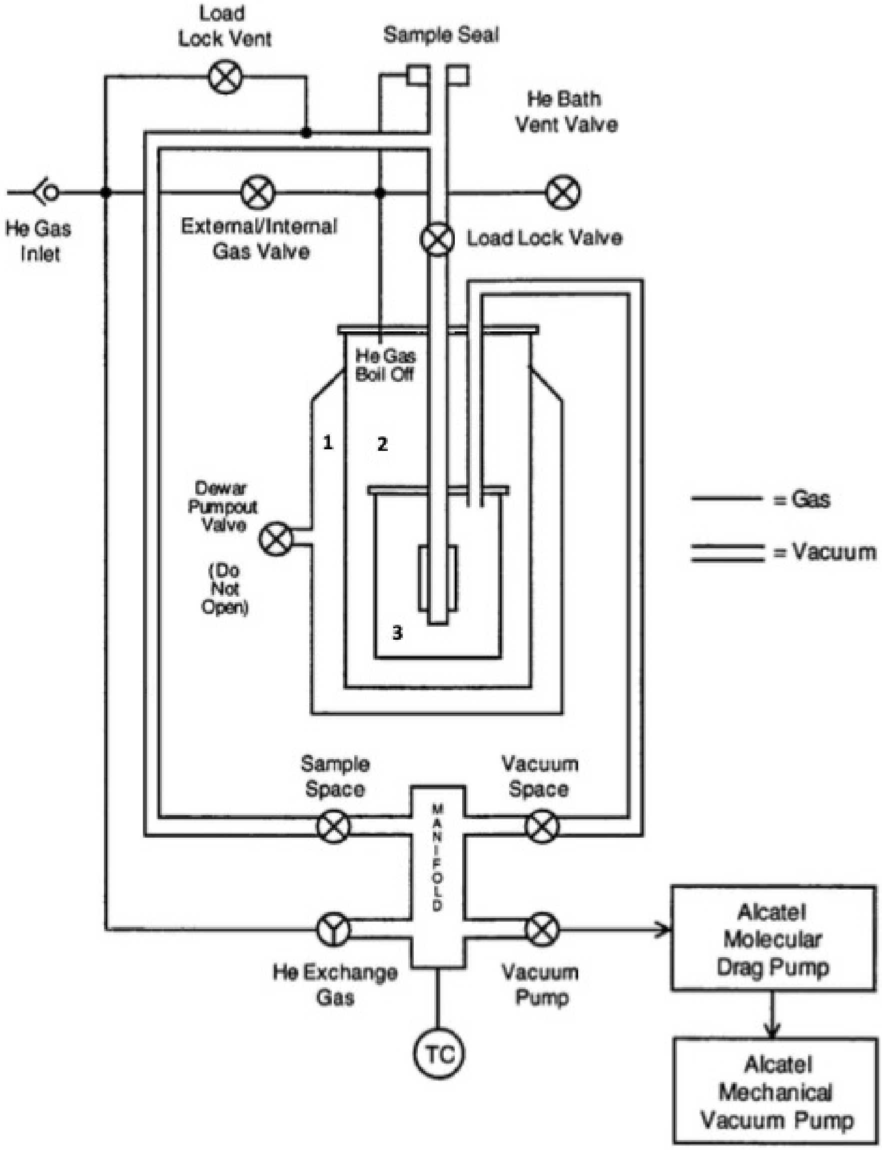

Figure 12: Schematic sketch of the different chambers of the AC susceptometer. 1) Dewar, 2) Helium chamber and 3) Vakuum chamber. Adapted from Ref. [70].

field are out-of-phase. Therefore, the susceptibility can be separated in an in-phase and out-phase component. The phase shifts of the measured voltage amplitudes are analyzed by comparing the signal of the secondary coils to a reference signal of the lock-in amplifier. The real part (χ') and imaginary part (χ") of the susceptibility is evaluated from the measured inphase (U') and out-phase (U") voltage components:

$$\chi' = \frac{\alpha U'}{VfH} \tag{3.4}$$

$$\chi" = -\frac{\alpha U"}{VfH}, \tag{3.5}$$

where α corresponds to a calibration constant which depends on the coil geometry and is given by the manufacturer. The parameter V refers to the volume of the sample, f is the frequency of the AC field and H denotes the root mean square value of the alternating magnetic field produced by the primary coil. As it is often more convenient to determine the mass (m) of the sample rather than the volume, the susceptibility can be specified as mass susceptibility by incorporating the density of the sample material:

$$\chi_{\mathrm{m}} = \frac{\chi}{\rho} = \frac{\alpha U}{mfH} \tag{3.6}$$

In the *Lakeshore* 7000 Series System User's Manual [70] and in Binder's master thesis [69] further information on the measurement system and the implemented modifications is provided.

For mounting the sample, it does not have to have a specific shape as long as it fits into the sample holder. The latter is a hollow cylinder made out of plastic material. If it is desired to measure the susceptibility of a sample in a specific crystalline direction, the crystal can be attached to a paper strip with *Loctite* superglue in order to support an accurate alignment. Another method to fix the specimen is to fill the empty space of the cylinder with cotton-wool. The cylinder is then affixed to a stick which is inserted into the cryostat. The sample material and the dimension of the examined crystalline cube is given in Appendix A.4.

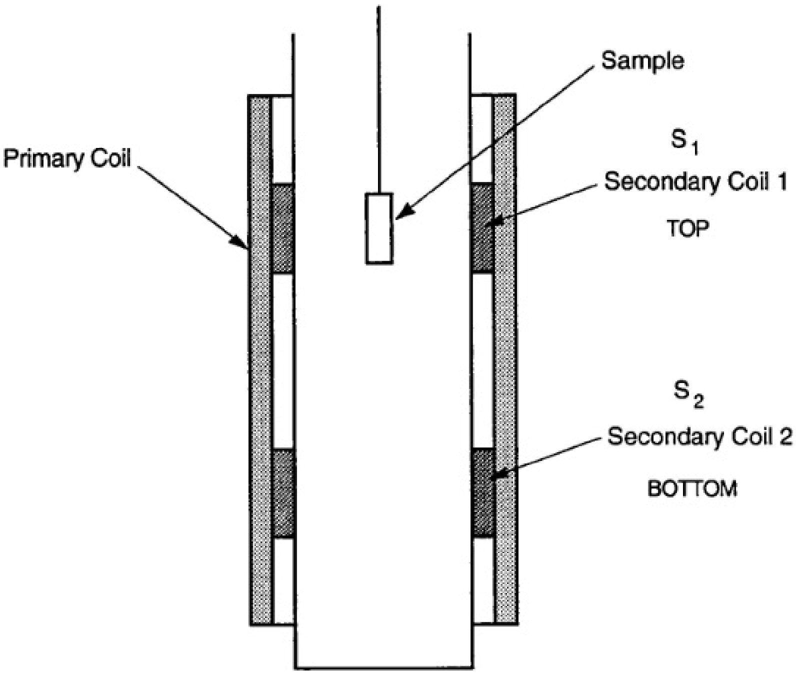

Figure 13: Sketch of the coils inside the vacuum chamber. Taken from Ref. [70].

3.3 Calibration of the AC Susceptometer for $T < 4.2$ K

Blank Signal Correction

Before the AC susceptibility of samples can be measured, an addenda measurement, or also called blank signal (BS) measurement, had to be made once in order to cancel out contributions to the measured signal originating from *e.g.* the sample holder or additionally used tools to fix the sample. The blank signal measurement was only implemented down to 4.2 K by Georg Binder [69]. As the measurements conducted in this work started at lower temperatures, an additional blank signal correction for the temperature range of $T < 4.2$ K had to be carried out.

To clarify, in the following explanation the terms "original", "automatically corrected" or a similar expression correspond to the data that is corrected with the previously measured blank signal which was done by Georg Binder. Whereas "(twice) corrected" signifies that the before-mentioned data was corrected again by the means of the blank signal measurement conducted in the course of this thesis.

Firstly, an addenda measurement with a capsule solely filled with a paper strip of similar length to the one used for the previous measurements with the $PrNiC_2$ cube and cotton wool was performed. The same values of the magnetic field and frequencies, as in the measurements that were already carried out with a sample, were adjusted. More precisely, this means the measurement was conducted at 400 A/m and frequencies of 11 Hz, 22 Hz, 40 Hz, 90 Hz, 222 Hz, 400 Hz and 889 Hz. Then, the automatically blank signal corrected inphase and outphase susceptibilities of the previous and the new addenda measurements were compared to get an initial assessment of the error. Moreover, a reasonable temperature range for the fit, with which the obtained data will be corrected for the second time subsequently, could be determined. As a next step, the original inphase and outphase voltages of the new blank signal measurement were plotted for each frequency. Optimally, this voltage is zero for all temperatures because this would mean the previous blank signal calibration implemented by Georg Binder holds for all temperatures. The data is shown in Fig. 14 and it is visible that below 4 K the deviation from the desired value zero augments towards lower temperatures for both, the inphase and outphase component. A strong and similar frequency dependence is revealed. The higher the frequency, the higher the deviation from the optimal calibration.

Each one of these curves was fitted up to 5 K in order to slowly approximate the fit to zero and to prevent sharp kinks at the transition between the corrected and the original data. Independently of the fitted component and the frequency, the same function suited best for the fits:

$$y = a + be^{\text{-x}} \tag{3.7}$$

Only the fit parameters a and b varied. The parameters for each frequency are listed in Table 1 and Table 2 for the original inphase and outphase voltage component, respectively. For both components, it can be seen that the parameter a successively increases and b decreases with increasing frequency. The orders of magnitude are comparable for both components but the parameters of the outphase component are slightly smaller than those of the inphase voltage component. One fit of the inphase and outphase voltage component measured at 889 Hz is depicted in Fig. 15. In Fig. 16, the original and

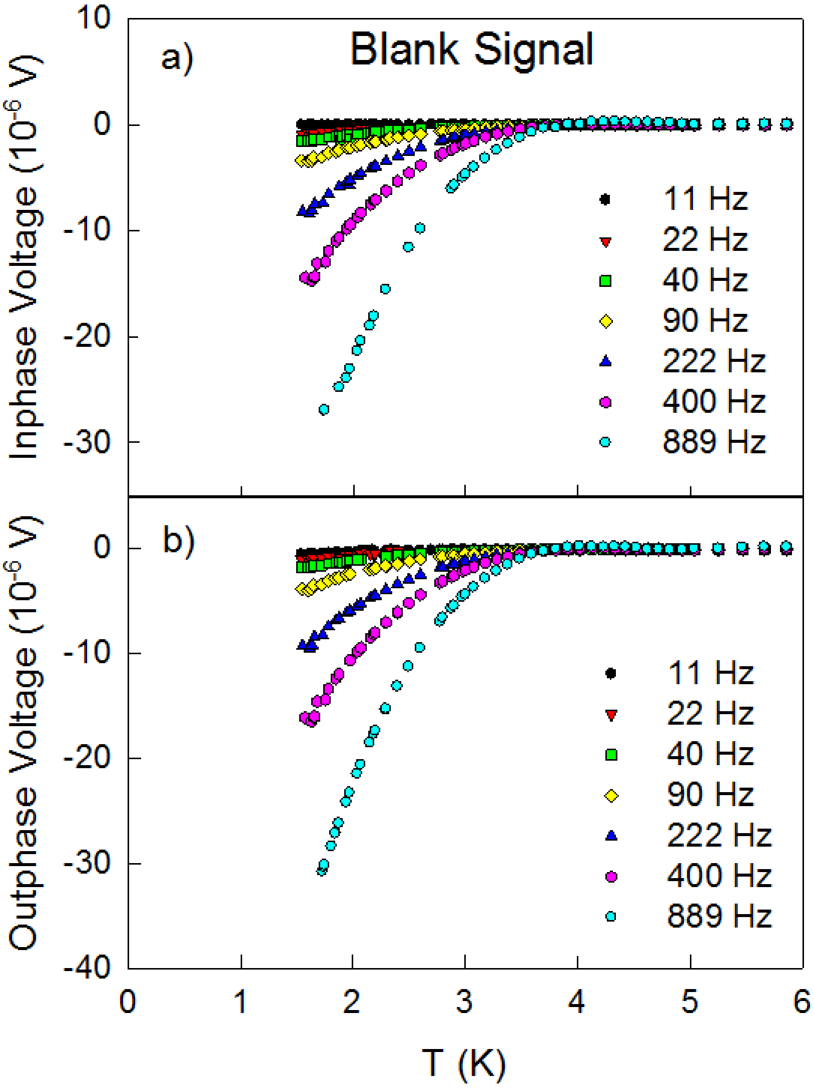

Figure 14: Original a) inphase and b) outphase voltage component of the new blank signal measurement.

corrected voltage for both components at 889 Hz is plotted. The fits and the voltage data of the measurements at other frequencies do not differ significantly one from the other. After the second correction, the curve approximates zero, as intended, but small over- or undercompensations are visible, especially at the temperatures where the fit deviates from the data.

Table 1: Fit parameters of the inphase component fit of the original voltage.

Inphase Component Fit		
Frequency in Hz	a [10^{-6} V]	b [10^{-6} V]
11	0.0397318	-2.27460
22	0.0678011	-4.22720
40	0.128512	-7.76210
90	0.287996	-17.2160
222	1.14868	-45.1900
400	1.44796	-77.7690
889	3.09238	-165.300

Table 2: Fit parameters of the outphase component fit of the original voltage.

Outphase Component Fit		
Frequency in Hz	a [10^{-6} V]	b [10^{-6} V]
11	0.0813236	-2.77930
22	0.144397	-5.28580
40	0.231163	-9.27130
90	0.506005	-20.6270
222	1.26485	-50.7130
400	2.60387	-95.3660
889	5.43657	-204.510

By means of this new blank signal correction, all obtained data was adjusted and the corrected susceptibility was calculated. The procedure will be outlined in this paragraph. After finishing the AC susceptibility measurement with a sample in the capsule, the automatically corrected inphase and outphase voltages of each frequency are corrected for the second time. Firstly, the values of the fit, given in Eq. 3.7, for the measured sample temperatures (x-value) and with the corresponding parameters a and b are calculated but only as far as the obtained y-value is negative. Then, the absolute value of this result is added to the automatically corrected voltage. Next, the conversion factor for calculating the susceptibility from the voltage, which is amongst others dependent on the mass of the sample and the frequency, *c.f.* Eq. 3.6, is evaluated. This is done by dividing the automatically corrected susceptibility given in the data file by the automatically corrected voltage component. By multiplying this conversion factor with the voltage data which has just been corrected with the blank signal fit, the final susceptibility results.

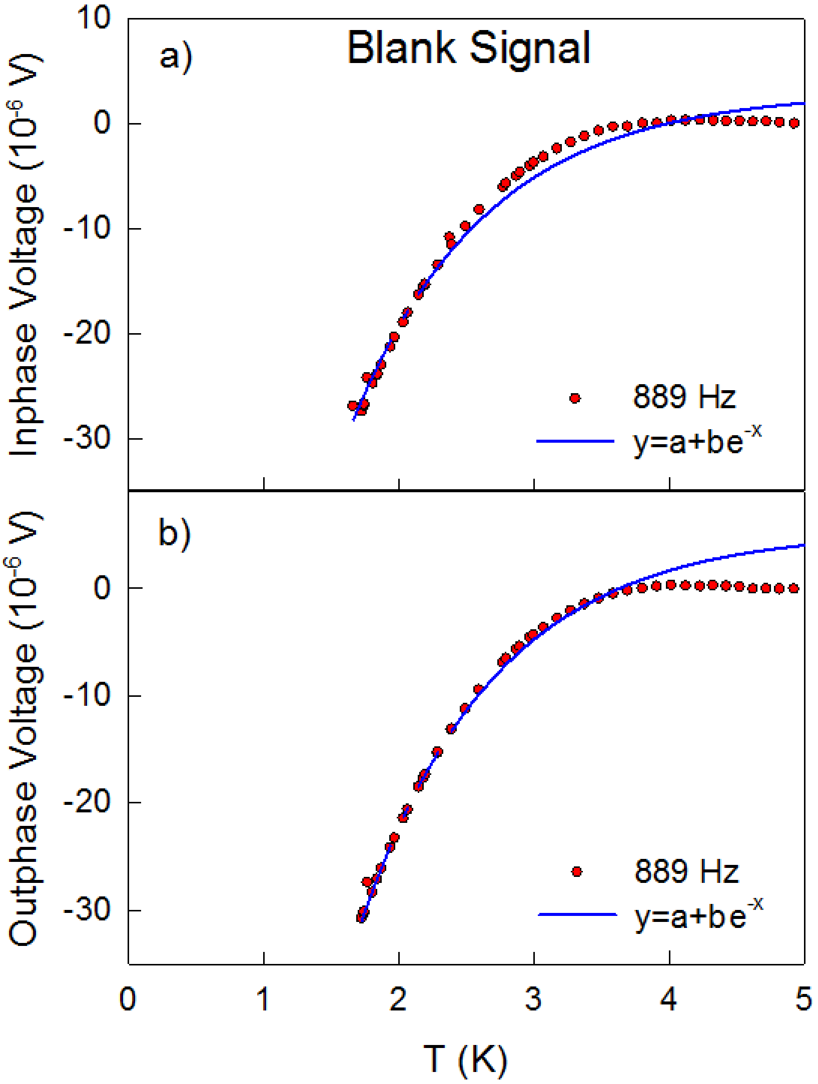

Figure 15: Original a) inphase and b) outphase component of the voltages of the blank signal at 889 Hz with a fit.

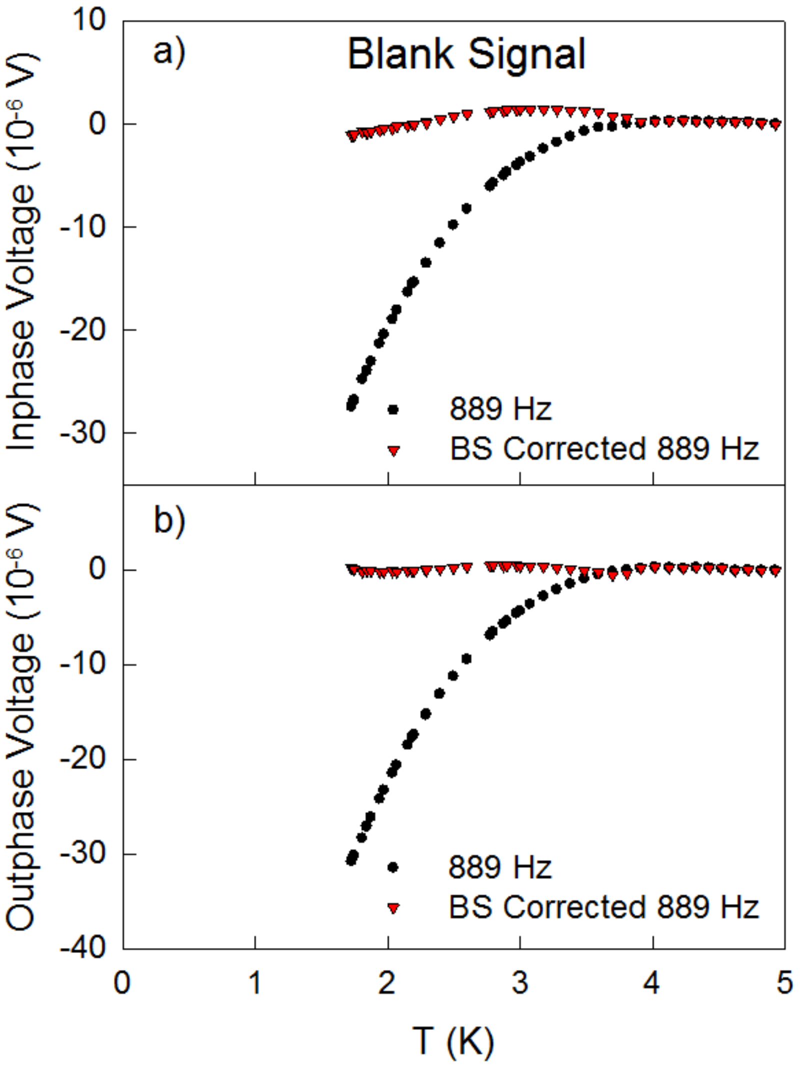

Figure 16: Automatically corrected and twice corrected voltages of the a) inphase and b) outphase blank signal measurement at 889 Hz.

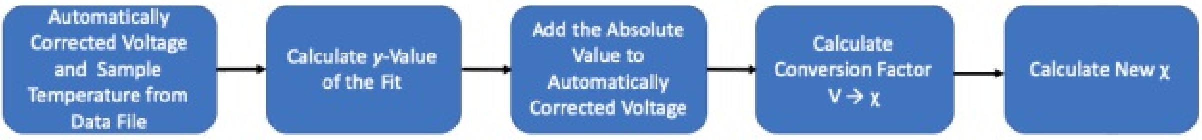

Figure 17: Procedure to calculate the blank signal corrected susceptibility.

Temperature Calibration

In addition to the incomplete implementation of the blank signal, it was figured out that the temperature calibration at low temperatures is incorrect. Due to this circumstance, after correcting the voltage data, the measured temperature had to be adjusted as well.

As a first step, a reference measurement with $Gd_2(SO_4)_3*8H_2O$ (Gadolinium(III) sulfate octahydrate) was conducted. This material is often used for reference measurements because its nearly ideal paramagnetic properties follow the Curie law rather accurately. A sample with a mass of 86.920 mg was examined with a magnetic alternating field of 400 A/m and a frequency of 889 Hz at temperatures ranging from ~ 1.6 K to room temperature. Initially, the susceptibility was corrected in the manner which was explained in the previous section. In Fig. 18, the real part of the original and the BS corrected inverse susceptibility in mol-Gd/emu are plotted. It can be seen that the correction is hardly noticeable at temperatures above 2 K. Nonetheless, below 5 K a deviation from the Curie law is recognizable, as the slope changes and the data does not follow a straight line. This is an indicator that the temperature calibration of the measurement system is not correct at lowest temperatures. There may be a variety of reasons for this, *e.g.* the fact that the used measurement device is about 30 years old and has never been recalibrated or the deviations originate from the temperature sensors as they are not directly placed at the sample or maybe the sample holder has an influence and displays a temperature offset which deserves being corrected.

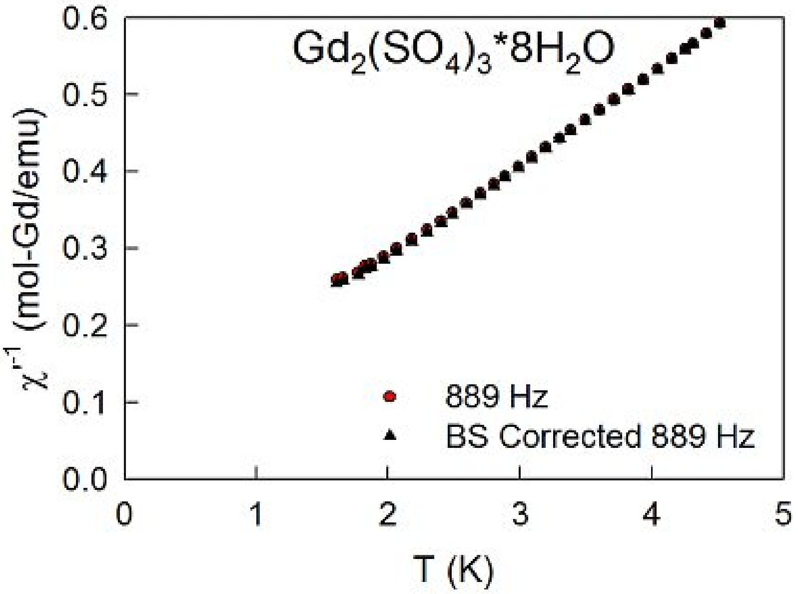

Figure 18: Original and blank signal corrected inverse susceptibility on the basis of the new addenda measurement.

The aim is to correct the temperature and therefore shift the divergent data points. At first, a Curie fit between 4.2 K and 100 K was made to evaluate the Curie constant, *cf.* Eq. 2.25. After obtaining the value of $C = 7.6995$ emuK/mol-Gd, it was used to calculate the temperature that is expected for the measured susceptibility using the Curie law once more. Then, the difference of the measured and the expected temperature value (ΔT) was determined and plotted against the measured temperature. This curve was fitted between 1.6 K and 7.5 K with the following equation:

$$y = c + \frac{d}{x^{1.5}} \tag{3.8}$$

The parameters are: c = -0.03646448 and d = 0.766554100. The plot of the temperature difference against the temperature and the corresponding fit is given in Fig. 19.

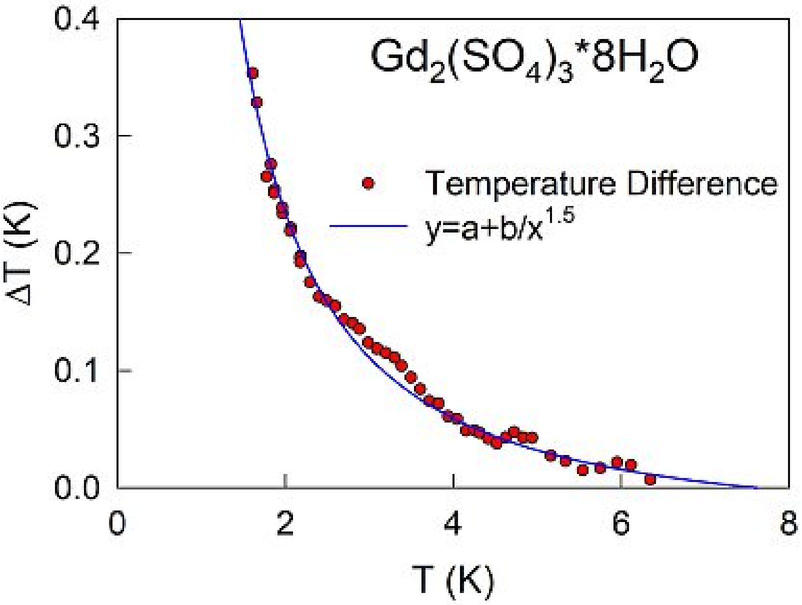

Figure 19: Temperature difference and corresponding fit.

In the last step, with the use of the fit (Eq. 3.8) the corresponding value of ΔT is calculated and added to the measured temperature if it is below 7.5 K. The final result is depicted in Fig. 20. The inverse susceptibility, the Curie fit and the temperature corrected inverse susceptibility are demonstrated. The corrected data now follows the Curie law as expected. Hence, for all measured data only this last step has to be followed to acquire the correct temperature.

To summarize this chapter, the different techniques of sample preparation starting from melting rods with induction heating, over growing crystals in the optical floating zone furnace and subsequently examining the crystalline structure with polarized light and Laue diffraction were outlined. Further, methods and experimental setups to explore the electric, thermoelastic and magnetic properties of the rare-earth samples were described. In the last section, the procedure of correcting the AC susceptibility data due to a missing blank signal measurement and a deficient temperature calibration below 4 K were described. The conducted measurements including the sample dimensions and masses, as well as additional graphics and an exemplary excel sheet with formulas to correct the original susceptibility data are collected in Appendix A and G.

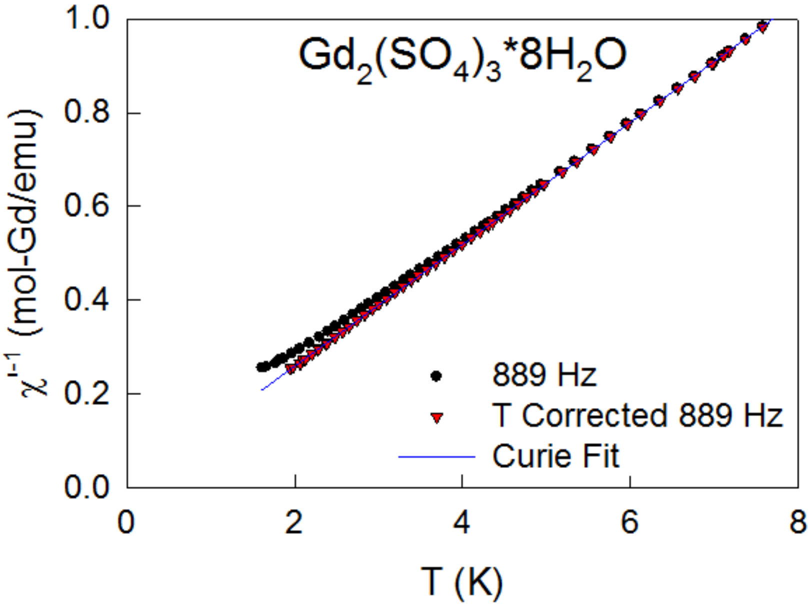

Figure 20: Susceptibility data of $Gd_2(SO_4)_3$*8H_2O, Curie fit and the temperature corrected data.

4 Suppression of CDW in $LuNiC_2$ by Co Substitution

4.1 Motivation and State of the Art

In recent years, the suppression of the charge density wave by pressure or substitution has been witnessed in several systems. At the quantum critical point in the limit of $T_{CDW} \to 0$, superconductivity that is associated with quantum fluctuations has already been observed in *e.g.* $LaNiC_2$ [10, 11] and $Lu(Pt_{1\text{-x}}Pd_x)_2$ [71]. Whereas in $LuNiC_2$, the commensurate charge density wave transition was discovered at around 450 K, in $LuCoC_2$, no indications of this phase transition was found above 0.4 K [4]. Along with the findings of Vock [72], which indicate that $LuNi_{1\text{-x}}Co_xC_2$ is an isostructural system, this would suggest the existence of a quantum critical point that is related to the suppression of the CDW. Therefore, the emphasis was to discover this quantum critical point and to search for the emergence of superconductivity.

In the last few years, several project works dealt with the partial substitution of Ni by Co in $LuNiC_2$. The crystallographic structure of $LuNi_{1\text{-x}}Co_xC_2$ with $x = 0.75$, 0.50, 0.20 or 0.10 was analyzed with powder X-ray diffraction by Vock [72]. Additional data, with $x = 1$, 0.66, 0.5 and 0.33, was provided by Levytskyy [73]. With these powder diffraction measurements, only the orthorhombic structure was investigated and with the employed method the charge density wave superstucture cannot be observed but it was found that the structure of the high-temperature system is not modified. It was discovered that the structural dependence of the lattice parameters is based on electrical effects and the $LuNi_{1\text{-x}}Co_xC_2$ system continuously exists with the substitution by Co. However, in none of the conducted resistivity or heat capacity measurements, a CDW transition was identified. It was suggested that replacing Ni with Co suppresses the formation of a charge density wave and in mixtures with less Co a CDW transition might be visible. During the project work of Fritthum [74], $LuNi_{0.92}Co_{0.08}C_2$ was grown and analyzed. A resistivity measurement with the current being applied parallel to the a-axis of a single crystalline piece uncovered a CDW transition in $LuNi_{1\text{-x}}Co_xC_2$ for the first time. The Peierls temperature was found at $\sim$ 301 K, which is lower than transition temperature of $LuNiC_2$. The resistivity measurement conducted by Fritthum [74], is shown in Fig. 21 with an additional inset in which the CDW temperature in dependence of the fraction of Ni versus Co in %-Co is extrapolated. The two dots indicate measured values of $LuNiC_2$ and $LuNi_{0.92}Co_{0.08}C_2$ and the line is a fit of the estimated T_{CDW} of the different compositions. Based on this approximation, the critical point that is associated with the suppression of the CDW is considered to be in the range of 14 %-Co to 20 %-Co. Therefore, the commenced study is complemented with further resistivity, heat capacity and magnetic measurements of crystals from the $LuNi_xCo_{1\text{-x}}C_2$ solid solution with a Co fraction at the Ni site of 8 %, 14 % and 20 %.

4.2 Resistivity

The temperature dependent electrical resistivities of the two floating-zone-grown $LuNi_{0.8}Co_{0.2}C_2$ and $LuNi_{0.86}Co_{0.14}C_2$ samples, all poly- rather than single crystalline, were measured. Due to uncertainties with respect to the effective geometry in the case of cracks inside the sample and with respect to the referential orientation, the absolute

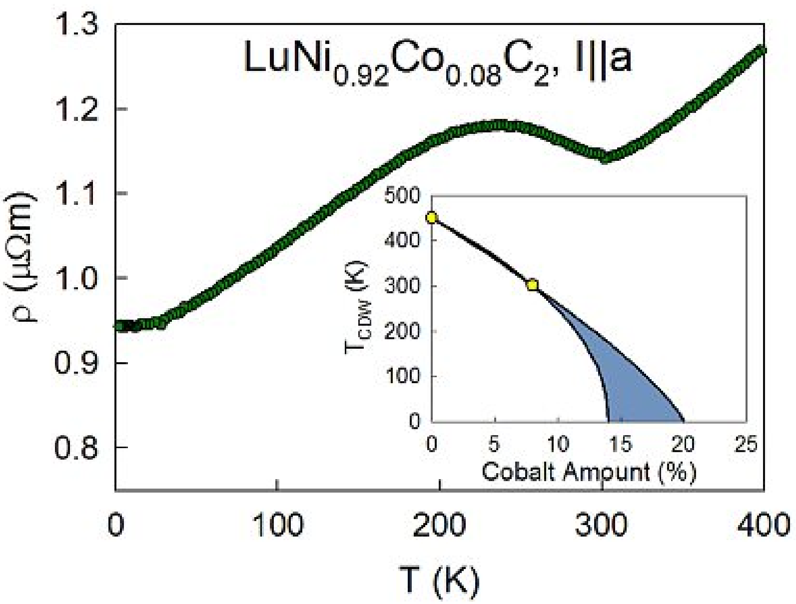

Figure 21: Resistivity ρ in $\mu\Omega$m in dependence of the temperature T of the $\mathrm{LuNi_{0.92}Co_{0.08}C_2}$ single crystal with $I||a$. The measurement was performed by Fritthum [74]. The inset shows the expected charge density wave temperature in dependence of the Co fraction.

values of the resistivities of the three samples are rather high and it is more convenient to plot the resistivity normalized to the resistivity measured at 350 K, *c.f.* Fig. 22. The resistivity increases with rising temperature for all three samples and uncover a simple metallic behavior. The slope of the $\mathrm{LuNi_{0.86}Co_{0.14}C_2}$ crystal is steepest and the slope of the first grown $\mathrm{LuNi_{0.8}Co_{0.2}C_2}$ is the flattest one. The absolute residual resistivity ρ_0 of the first $\mathrm{LuNi_{0.8}Co_{0.2}C_2}$ crystal accounts for approximately 2.43 $\mu\Omega$m, ρ_0 of the second crystal of its kind is $\sim$ 1.27 $\mu\Omega$m and for $\mathrm{LuNi_{0.86}Co_{0.14}C_2}$, ρ_0 accounts for approximately 0.47 $\mu\Omega$m. In Ref. [4], the residual resistivities of single crystalline $\mathrm{LuCoC_2}$ and $\mathrm{LuNiC_2}$ are given with $\sim$ 0.07 $\mu\Omega$m and $\sim$ 0.4 $\mu\Omega$m respectively. The behavior of the residual resistivity in dependence of the fraction of Co roughly conforms to the expectations based on Nordheim's rule [75]. However, the deviating values of ρ_0 of the two $\mathrm{LuNi_{0.8}Co_{0.2}C_2}$ samples confirm the above-mentioned uncertainties.

At $\sim$ 50 K and 100 K two minor kinks are remarkable in the $\mathrm{LuNi_{0.86}Co_{0.14}C_2}$ data. At approximately 120 K, the same data reveals a clear anomaly that matches to the predicted T_{CDW}, *c.f.* Fig. 21, and thus very likely corresponds to a charge density wave transition. $\mathrm{LuNi_{0.8}Co_{0.2}C_2}$ displays just a smooth bending towards residual resistivity at low temperatures with no indication of CDW ordering. In the inset of Fig. 22, the extrapolation of T_{CDW} in dependence of %-Co of the solid solution based on the three already discovered transition temperatures is presented.

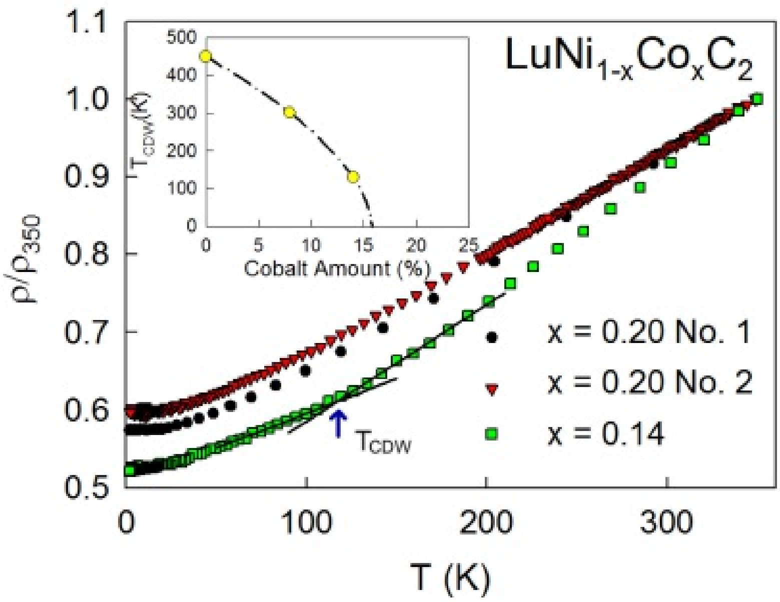

Figure 22: Resistivity normalized to ρ at 350 K in dependence of the temperature T of the three floating zone grown $LuNi_{1-x}Co_xC_2$ samples with an inset of the updated expected charge density wave temperatures in dependence of the amount of Co in %.

4.3 Heat Capacity

In Fig. 23, the temperature dependent specific heat capacity of single crystalline $LuNi_{0.92}Co_{0.08}C_2$ and the secondly grown multidomain crystals of $LuNi_{0.86}Co_{0.14}C_2$ and $LuNi_{0.8}Co_{0.2}C_2$, are shown. A metallic behavior is noticeable for all samples and C_p increases with the augmentation of the temperature. The difference between the curves of different materials is minimal. Concerning $LuNi_{0.92}Co_{0.08}C_2$, both, the heating and the cooling process, were investigated. The two curves are identical at all temperatures except between $\sim$ 290 K and $\sim$ 320 K, which is shown in Fig. 24. These kinks are very likely connected to the resistivity anomaly that has already been observed in the resistivity measurement that was conducted by Fritthum [74]. No other kinks or anomalies, which could point at a phase transition, can be distinguished in the measured temperature range for the three samples. Due to limited availability of experimental time, the addenda measurement for $LuNi_{0.8}Co_{0.2}C_2$ was omitted and the heat capacity data was corrected with a generic addenda which could have minor influences on the obtained results.

In the paper by Steiner *et al.* [4], experimentally obtained values of the Sommerfeld coefficient γ of $LuNiC_2$, as well as DFT *ab initio* calculated $\gamma_{DFT} = N(E_F)k_B^2\pi^2/3$, with $N(E_F)$ the density of states at the Fermi level, have already been studied. The DFT calculated Sommerfeld coefficient of the orthorhombic parent structure without CDW was given with $\gamma_{DFT} = 2.43$ mJ/molK^2 but experimentally $\gamma = 0.83(5)$ mJ/molK^2 was revealed. The computed Sommerfeld coefficient γ_{DFT}^{CDW} of the CDW modulated structure accounted for 0.90 mJ/molK^2 which showed a close agreement with the experimental findings. It was demonstrated that the CDW superstructure causes the formation of a partial gap in the density of states at the Fermi level [4]. On the basis of this result, the Sommerfeld coefficient and the Debye temperature were evaluated for all three samples

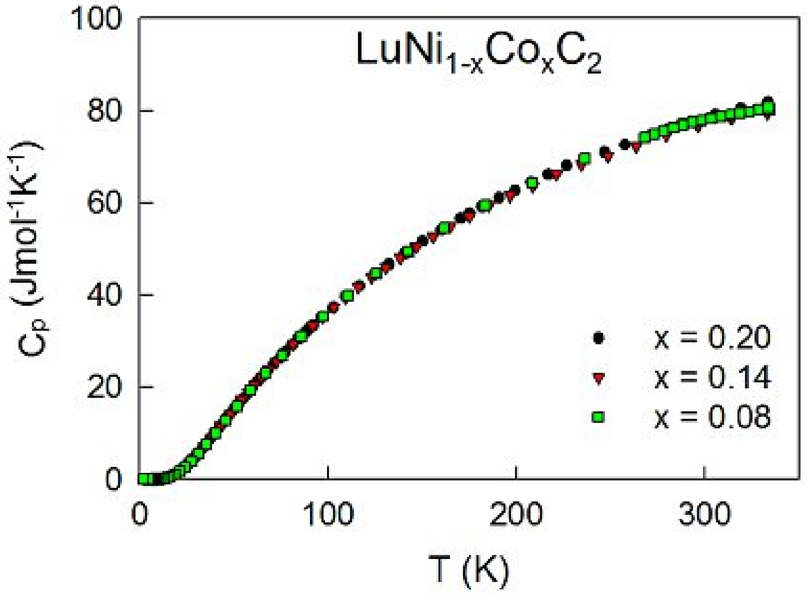

Figure 23: Specific heat capacity of polycrystalline $LuNi_{1-x}Co_xC_2$.

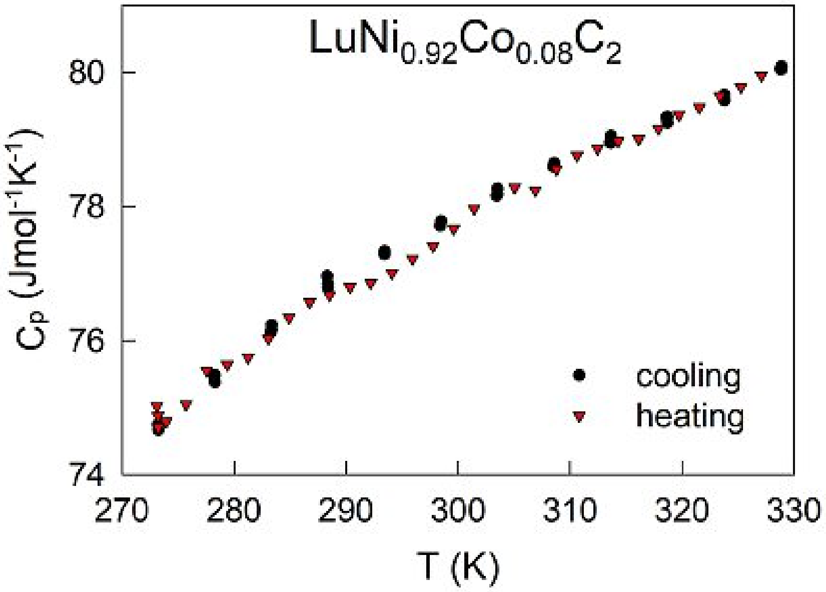

Figure 24: Specific heat capacity of $LuNi_{0.92}Co_{0.08}C_2$ during heating and cooling in the range of 270 K to 330 K.

of $LuNi_{1-x}Co_xC_2$ in the manner which was described in section 2.3. In Fig. 25, the heat capacity is plotted as C/T versus T^2. In addition to the measured data, the fit of the data points and extrapolation for T → 0 is depicted. The T^2 range that was used for the fit considered data below 40 K^2, as from then on the deviation of the data points from a straight line was apparent. With the fit, γ and β were evaluated. Consequently, the obtained Sommerfeld coefficient γ accounts for 1.91(1) $mJ/molK^2$ and the coefficient β is 7.178×10^{-5} $J/molK^4$ for $LuNi_{0.92}Co_{0.08}C_2$. Regarding $LuNi_{0.86}Co_{0.14}C_2$, the Sommerfeld coefficient accounts for 2.48(9) $mJ/molK^2$ and $\beta = 8.530\times10^{-5}$ $J/molK^4$. Lastly, γ of $LuNi_{0.8}Co_{0.2}C_2$ accounts for 2.54(9) $mJ/molK^2$ and $\beta = 7.621\times10^{-5}$ $J/molK^4$. Subsequently, the Debye temperatures were calculated using Eq. 2.23. The number of atoms per formula unit (N) of $LuNi_{1-x}Co_xC_2$ is 4. Hence, the Debye temperatures are Θ_D = 477(5) K, Θ_D = 450(1) K and Θ_D = 467(2) K for $LuNi_{0.92}Co_{0.08}C_2$, $LuNi_{0.86}Co_{0.14}C_2$ and $LuNi_{0.8}Co_{0.2}C_2$, respectively. These seem to be reasonable values, when comparing to the findings of Ref. [4], where Θ_D = 444(8) K for $LuCoC_2$ and Θ_D = 500(10) K for $LuNiC_2$. Moreover, also the obtained values for γ are in the same order of magnitude and lie between the values of the Sommerfeld coefficients reported in Ref. [4]. A trend that γ increases and Θ_D decreases with increasing amount of Co is remarkable. This finding also conforms to the results of the heat capacity measurements of Vock [72]. While the obtained Sommerfeld coefficients of $LuNi_{0.86}Co_{0.14}C_2$ and $LuNi_{0.8}Co_{0.2}C_2$ strongly converge towards $\gamma_{DFT} = 2.43$ $mJ/molK^2$ and thus imply a vanishing of the CDW gap, the γ of $LuNi_{0.92}Co_{0.08}C_2$ indicates that a partial energy gap is formed. The Debye temperature of $LuNi_{0.8}Co_{0.2}C_2$ does not fit correctly into the order when comparing it to Θ_D of the other two measured samples. This deviation is most likely an artefact of the missing addenda measurement and the insufficiently precise way of how the data was corrected. The cited and all measured Sommerfeld coefficients, as well as Debye temperatures which were obtained during the course of this thesis, are listed in Table 3.

Table 3: Sommerfeld coefficients and Debye temperatures of $LuNi_{0.92}Co_{0.08}C_2$, $LuNi_{0.86}Co_{0.14}C_2$ and $LuNi_{0.8}Co_{0.2}C_2$ of the present work and $LuNiC_2$ as well as $LuCoC_2$ according to Ref. [4].

Sample	Sommerfeld Coefficient [$mJ/molK^2$]	Debye Temperature [K]
$LuNiC_2$	0.83(5)	500(10)
$LuNi_{0.92}Co_{0.08}C_2$	1.91(1)	477(5)
$LuNi_{0.86}Co_{0.14}C_2$	2.48(9)	450(1)
$LuNi_{0.8}Co_{0.2}C_2$	2.54(9)	467(2)
$LuCoC_2$	5.9(1)	444(8)

4.4 Magnetization

The oriented $LuNi_{0.92}Co_{0.08}C_2$ cube was examined in a Vibrating Sample Magnetometer in order to identify magnetic properties of this material. The sample was mounted with the a-axis parallel to the applied magnetic field. The magnetization against the magnetic field for three temperatures is displayed in Fig. 26. In Fig. 27, the temperature dependent measurement with a constant field of 1 T is presented.

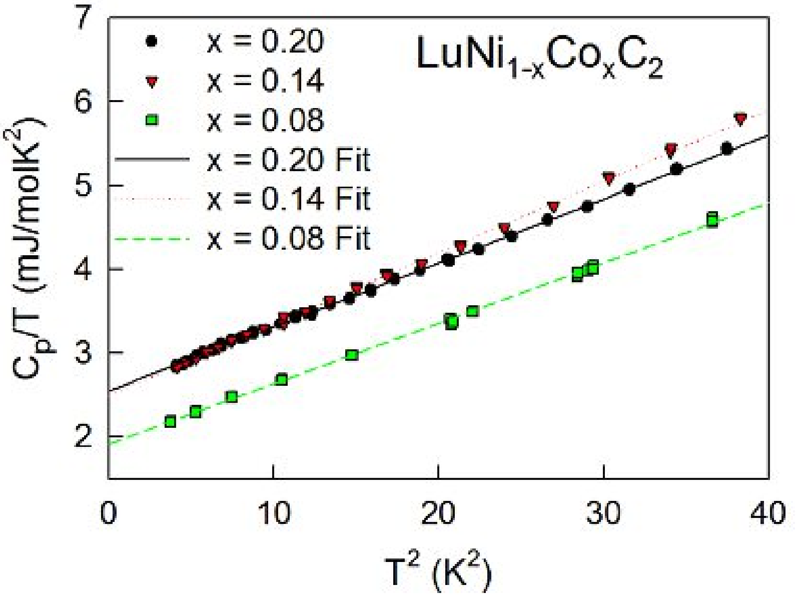

Figure 25: Low-temperature heat capacity and extrapolation for T → 0 of the polycrystalline LuNi$_{1\text{-x}}$Co$_\text{x}$C$_2$ samples.

The field dependent measurements in Fig. 26 reveal different magnetic contributions of the measured signal. The paramagnetic contribution can be identified due to the curve following a Brillouin function, which describes the magnetization in dependence of the applied magnetic field for an idealized paramagnet, *c.f.* Eq. 2.26. The negative values of the magnetization indicate a diamagnetic influence, as the magnetization in dependence of the field for an idealized diamagnet follows a straight line with negative slope and negative magnetization values. According to Ref. [76], the core-diamagnetic susceptibility of LuNiC$_2$ is expected to be $\chi_{core} \sim$ -3×10^{-5} cm^3/mol. The measured magnetic susceptibility of LuNi$_{0.92}$Co$_{0.08}$C$_2$ accounts for ∼ -10×10^{-5} cm^3/mol and indicates a stronger diamagnetic component which cannot be explained by the Ni/Co composition. It is assumed that leftovers of *Apiezon* grease from previous measurements influence the result. In general, the magnetization measured at 2 K resembles the one at 3 K and the magnetization is only slightly higher. A significantly greater difference is remarkable when comparing these measurements to the measurement at 25 K. The curvature of the magnetization nearly disappears completely and resembles a straight line. The transitions from positive to negative magnetization values occur at magnetic fields of approximately 1.7 T, 1.4 T and 0.2 T for measurements at 2 K, 3 K and 25 K, respectively.

The temperature dependent magnetization in Fig. 27 shows a distinctive cusp at ∼ 50 K. It is assumed that this dent originates from an impurity in the crystal. The upturn at low temperatures is due to small contaminations of the sample with magnetic rare-earth elements such as Gd. Apart from this, no other anomalies can be noted.

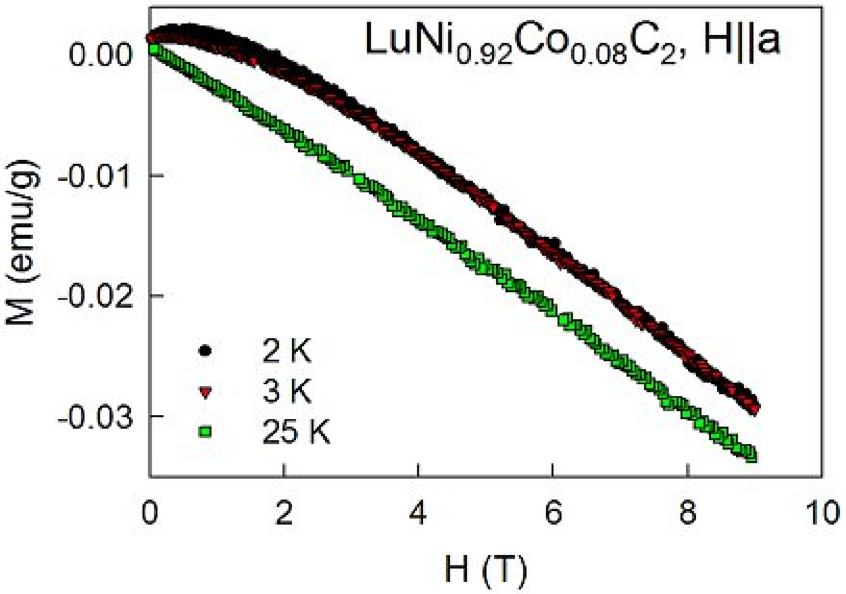

Figure 26: Field dependent magnetization of LuNi$_{0.92}$Co$_{0.08}$C$_2$.

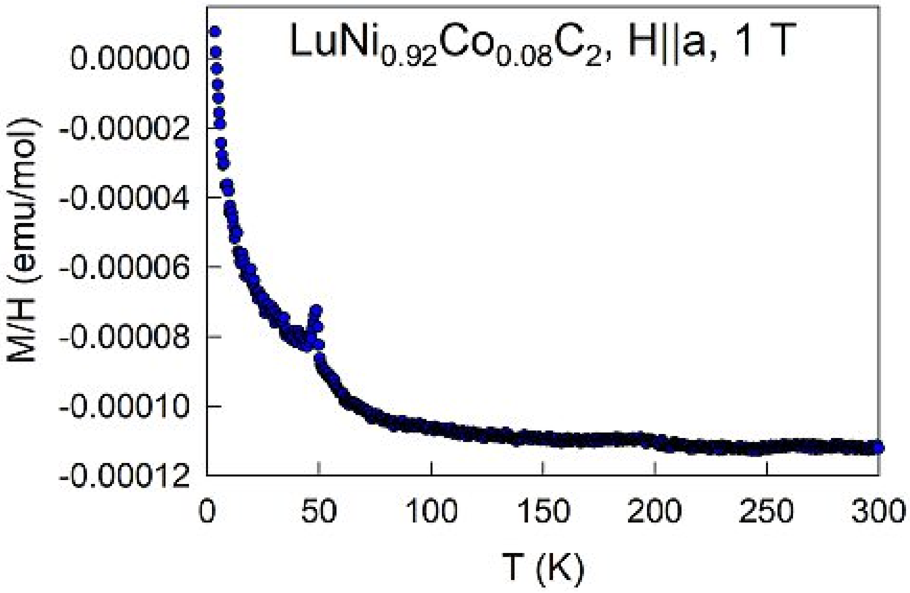

Figure 27: Temperature dependent magnetic measurement of LuNi$_{0.92}$Co$_{0.08}$C$_2$ with H parallel to a.

In addition, one piece of the second crystal of $LuNi_{0.8}Co_{0.2}C_2$ was examined with the SQUID. The magnetization against the magnetic field measured at two temperatures is depicted in Fig. 28. It is apparent that the ferromagnetic contribution dominates. This might originate from ferromagnetic impurities in the material. The magnetization rapidly increases and reaches saturation at roughly 1 T. The noise of the signal continuously augments with the enlargement of the magnetic field. The saturation magnetization at 20 K is slightly lower than M measured at 10 K.

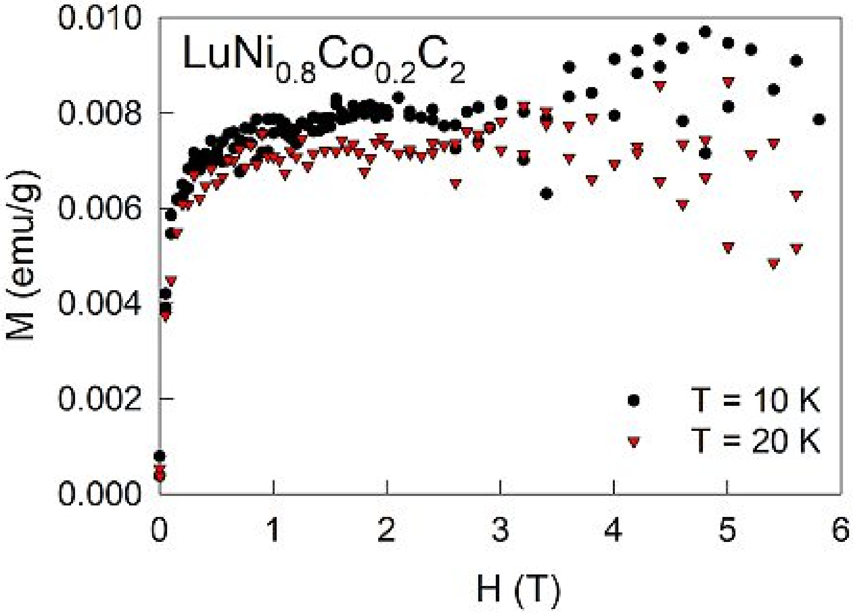

Figure 28: *M-H* measurement of $LuNi_{0.8}Co_{0.2}C_2$ at 10 K and 20 K.

Summary

The resistivity, as well as the specific heat confirm a metallic behavior of the three examined $LuNi_{1-x}Co_xC_2$ solid solutions with Co concentrations at the Ni site of 8 %, 14 % and 20 %. Superconductivity above 2 K is not discovered in any of these solid solutions. A charge density wave transition is observed for $LuNi_{0.86}Co_{0.14}C_2$ at approximately 120 K. The experimentally determined Sommerfeld coefficients conform to the tendency of a raising γ with increasing amount of Co in the $LuNi_{1-x}Co_xC_2$ solid solutions. In comparison with γ_{DFT} of Ref. [4], it is found that the partial CDW energy gap that is formed in $LuNiC_2$ closes gradually with increasing amount of Co. While in $LuNi_{0.92}Co_{0.08}C_2$ the obtained γ indicates that a partial energy gap is still present, the measured Sommerfeld coefficients of the other two compounds are in close agreement to γ_{DFT} of the orthorhombic parent structure without CDW. On the basis of these findings, evidence is growing that the critical point that is associated with the suppression of the CDW is in the range of 15 %-Co to 20 %-Co at the Ni site. The search for the emergency of superconductivity should be extended in the concentration range from 16 %-Co to 18 %-Co and to lower temperatures for $LuNi_{0.8}Co_{0.2}C_2$.

5 Magnetic Ground State of $PrNiC_2$

5.1 State of the Art and Motivation of the Present Study

Several groups working in the field of CDW systems or rather more specific rare-earth nickel dicarbides have already explored characteristic features of $PrNiC_2$. Onodera *et al.* [77], studied the magnetic properties of the material and confirmed the findings of Kotsanidis *et al.* [78], stating that $PrNiC_2$ is a Van Vleck paramagnet. According to Onodera *et al.*, no magnetic ordering is found down to 2 K. In the paper of Yamamoto *et. al* [79], it is reported about structural and electrical properties. In the most recent publication of Kolincio *et. al* [15], specific heat, magnetic and transport measurements were presented and the interplay with regard to the charge density wave was discussed. The Peierls transition of $PrNiC_2$ is specified at 89 K.

The aim of the present study was to probe whether a spin glass behavior, due to a dynamic frustration as in $PrAu_2Si_2$, which was discovered by Krimmel *et al.* [18] and Goremychkin *et al.* [37], could also be identified in $PrNiC_2$. Spin glasses display an AC susceptibility with a frequency dependent peak of its real part (the lower the excitation frequency, the lower the freezing temperature T_f). The latter would be a key indicator of a spin glass phase, as this characterizes the continuous transition from a paramagnetic to a spin glass phase. Another characteristic feature of a spin glass ground state is a large quasi-linear contribution to the low-temperature heat capacity with a smooth maximum at around $\sim T_f/2$ [80, 81]. For that reason, extensive magnetic measurements were undertaken, starting with AC susceptibility. The first AC susceptibility measurements of the $PrNiC_2$ cube were conducted before the blank signal correction and the temperature calibration of the AC susceptometer which is described in section 3.3. The susceptibility measurements of all directions of the crystal revealed a smooth frequency dependent maximum, which could point at a spin glass phase, but the imaginary part of χ pointed towards an artefact caused by a continuous phase shift at temperatures below 4 K, see Appendix H for initial uncalibrated data. While performing the additional calibration measurements, the magnetic properties of $PrNiC_2$ were studied with a SQUID magnetometer and the VSM option of the PPMS as well. Furthermore, the crystalline electric field of $PrNiC_2$ was analyzed. To do this, the magnetic data acquired with the VSM and the magnetic heat capacity data were fitted with the software *McPhase* [39] whereby the crystal field parameters were estimated.

5.2 Magnetic and Thermodynamic Properties

The susceptibility was measured for all three crystallographic axes and with six frequencies ranging from 22 to 889 Hz. In the following, the susceptibility measured with H applied parallel to the a-axis is labelled as χ_a and analogous definitions apply for χ_b and χ_c. The data of the real part susceptibility χ' and the imaginary susceptibility χ" in m^3/kg in dependence of the temperature are shown in Fig. 29. No clear phase transitions are found down to 1.9 K. According to Onodera *et al.* [77], $PrNiC_2$ is a Van-Vleck paramagnet down to 2 K. The paramagnetic behavior of the susceptibility is also apparent in the present measurements. A very weak frequency dependence is visible which further weakens with raising temperature. A kink that was observed by Kolincio *et al.* [15] at 8 K in polycrystalline $PrNiC_2$ is not traceable in the present single crystal data. An irregularity at around 4 K (small kink) is most likely due to the rough correction of the addenda as deviations of the fits from the original data lead to errors. The strong frequency dependence of χ" throughout the whole measured temperature range signalizes that eddy currents are induced in the sample. The eddy currents diminish with lower excitation frequencies.

The low-temperature heat capacity as C/T and the resistivity ρ, which has been measured earlier [82], are depicted in Fig. 31. A quasi-exponential increase of the heat capacity with a maximum above 4 K is identifiable but no corresponding anomaly at $\sim$ 8 K is revealed in the AC susceptibility. This specific heat maximum originates from crystal field effects as, apart from a moderately enhanced T-linear contribution which is theoretically predicted for Pr singlet states by Fulde [83] and is observed in comparable systems in similar magnitude [84], it can be described rather well with the crystalline electric field model which will be shown in the next section. Upon cooling, the resistivity decreases and thus the conductivity increases which could provoke an ascent in χ".

The acquired DC susceptibility and magnetization data obtained with a VSM are presented in Fig. 32. The field dependent magnetization for two temperatures, 2 K and 20 K, is depicted for the three principle orthorhombic orientations of the crystal in the external magnetic field. The paramagnetic nature of the magnetization is apparent, as it follows a Brillouin function for $H||b$ and $H||c$. A kink in the magnetization of the $H||a$ orientation at $\sim$ 2 T is visible in panel a) and is attributed to a level crossing effect among the two lowest energy CEF singlets. The easy axis of magnetization is a, the hardest axis is b. The obtained results are in close accordance with the findings of Onodera *et al.* [77].

The temperature dependent measurements at fields ranging from 0.1 to 3 T are presented in Fig. 33 in panels a), b) and c) respectively. In a field of a 0.1 T and at temperatures below 5.5 K, the magnetization along the crystallographic c-axis dominates. At above 5.5 K, a becomes the easy axis of magnetization. A similar behavior is observed in the measurements at 1 T and 3 T. Solely the crossing points of the curves are shifted to higher temperatures. With an external field of 1 T, the transition of a to become the easy axis is moved to 6.9 K and at a field of 3 T it is shifted to 9.5 K. Again, these findings conform to the studies by Onodera *et al.* [77].

In order to further analyze the low-field DC susceptibility behavior in closer detail, SQUID measurements were conducted with a low-field option (using a high-precision Keithley current source). Ahead of each measurement, a low-B degaussing of the superconducting magnet was performed to ensure, that no remanent magnetization of the superconducting magnet influences the outcomes. A unique characteristic of the spin glass phase is the irreversible magnetic behavior after cooling down with a non-zero magnetic field versus cooling down with a zero magnetic field. Therefore, the comparison of the zero-field-cooled (ZFC) and field-cooled (FC) magnetization is an instructive measure as a splitting of the ZFC and FC magnetization indicates the presence of a spin glass phase.

In Fig. 34, the ZFC and FC M-T curves measured with H parallel to the three crystallographic axes are shown with an applied field of 3 mT and 30 mT. Considering the a-axis,

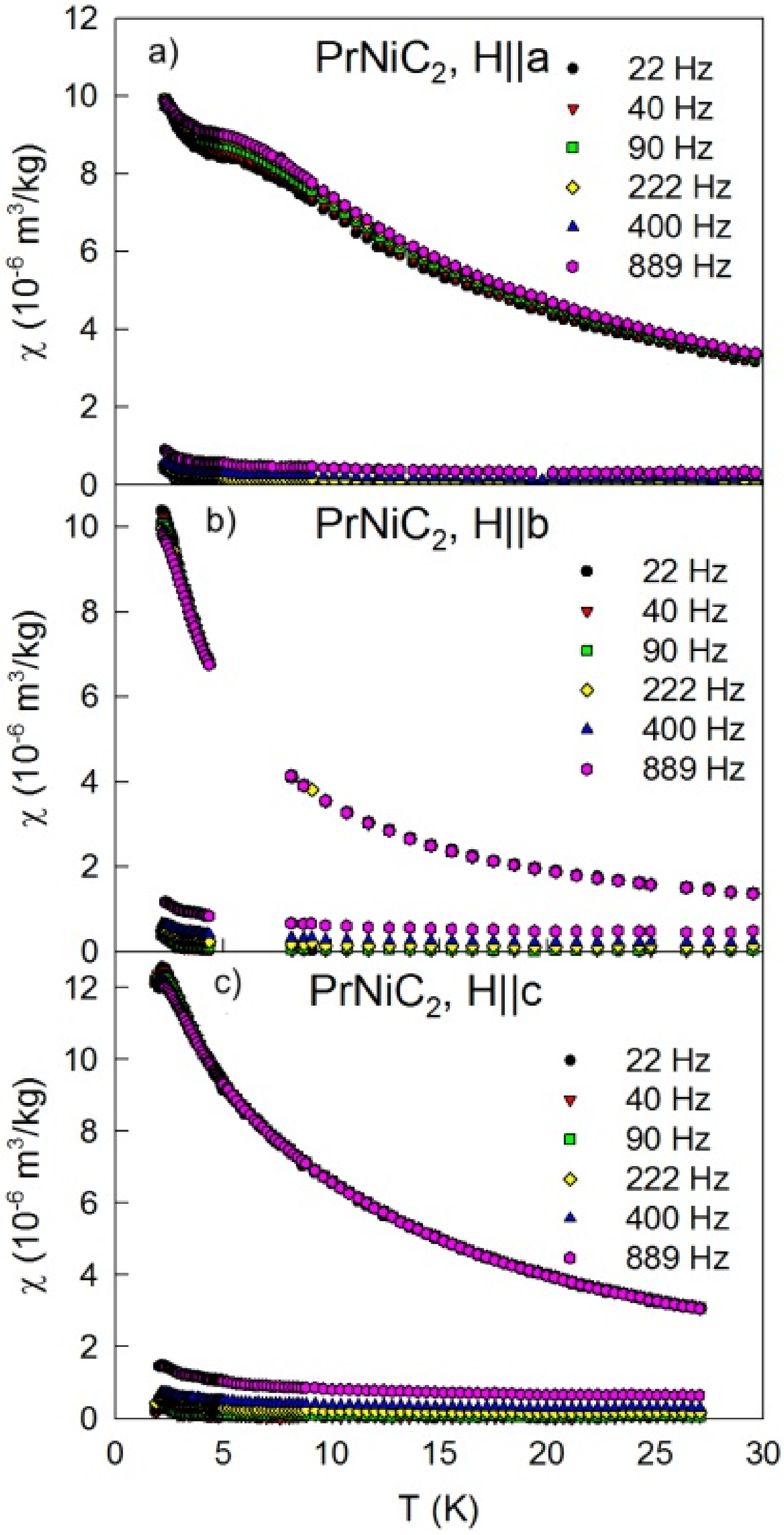

Figure 29: AC susceptibility of $PrNiC_2$ with a) $H||a$. b) $H||b$. c) $H||c$.

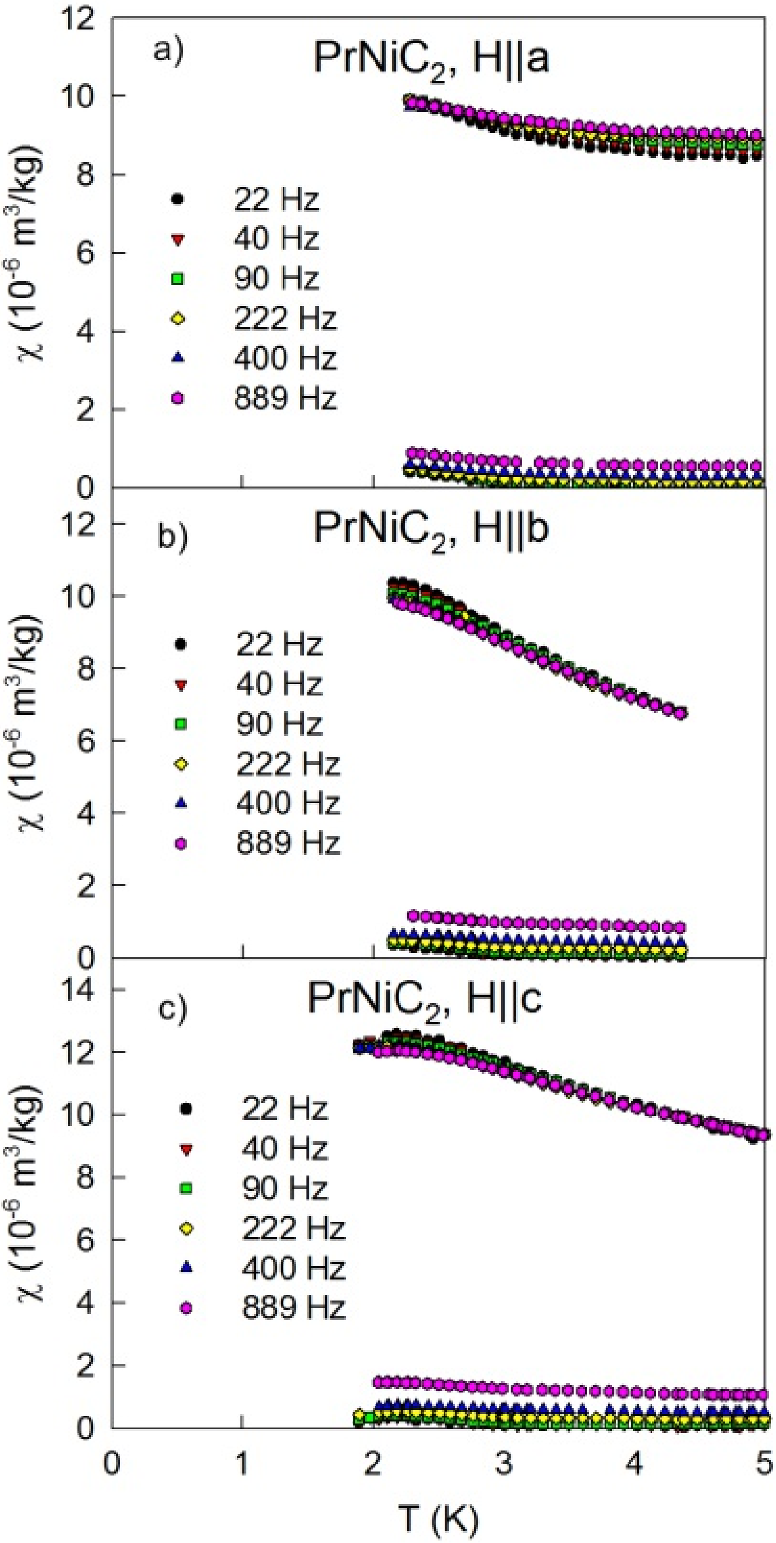

Figure 30: Close-up of the low-temperature AC susceptibility of $PrNiC_2$ with a) $H||a$. b) $H||b$. c) $H||c$.

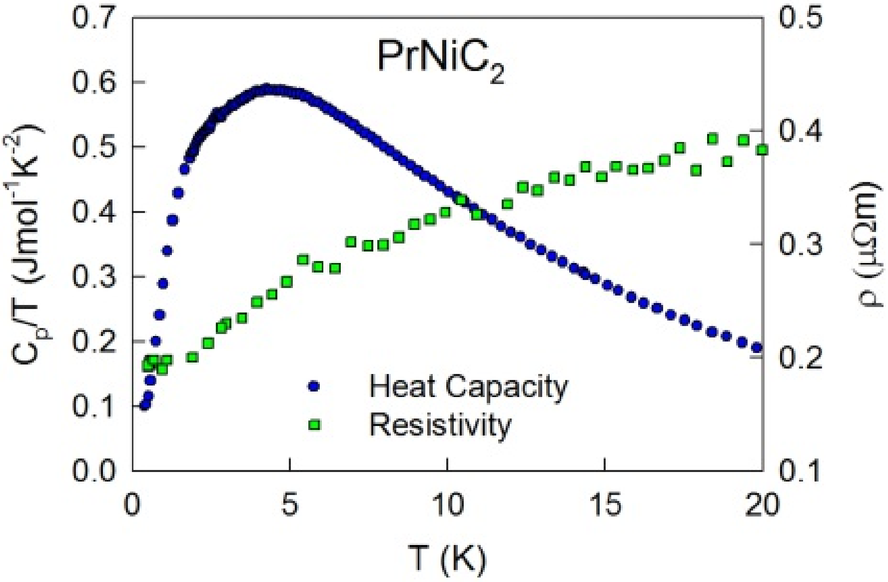

Figure 31: Temperature dependent low-temperature heat capacity and resistivity of PrNiC$_2$ [82].

a minimal difference between the ZFC and FC magnetizations is visible. The difference in magnetization of the first commonly measured data point at approximately 3.3 K accounts for 0.0029 emu/g and the same quantity of the 30 mT magnetization at the same temperature amounts to 0.0042 emu/g. In comparison to the absolute magnetization values, this splitting is small and does not signify a spin glass phase. The temperature at which the ZFC magnetization starts to deviate from the FC magnetization is at 8 K which coincides with the anomaly reported by Kolincio *et al.* [15] and most likely corresponds to crystalline precipitations. The splitting of the FC and ZFC magnetizations with H being parallel to the orthorhombic b-axis, as well as parallel to the c-axis, is hardly remarkable for both measured strengths of the magnetic field. These measurements prove that in PrNiC$_2$, no spin glass phase is present in the examined temperature range.

The last aspect that needed to be clarified is the suspicious behavior of the imaginary part of χ which would suggest a hysteretic nature of the material. In order to check this effect, M-H measurements for all axes of the cube were carried out in the SQUID. The obtained data is displayed in Fig. 35 for H parallel to the a-, b- and c-axis, in the panels a), b) and c) respectively. The main concern during the measurement was the stabilization of the temperature. The temperature differences between the data points of each measurement amount to a maximum of 0.16 K, which can be considered as sufficiently stable. To visualize possible hysteretic features, in the insets of each panel, a smaller range of the magnetic field around 0 T is shown. Here, a straight line is drawn to demonstrate the deviation of the up and down loops. An opening of the hysteresis is only visible in M-H measurement with $H||a$. The opening is not sufficiently pronounced to explain the observed behavior of the imaginary susceptibility at low temperatures. Consequently, from these results it is disproved that the hysteretic nature of the material evokes the low temperature upturn in χ" that was observed in the AC susceptibility measurements. Therefore, the temperature dependent behavior of the resistivity, *c.f.* Fig. 31, is connected to that of χ".

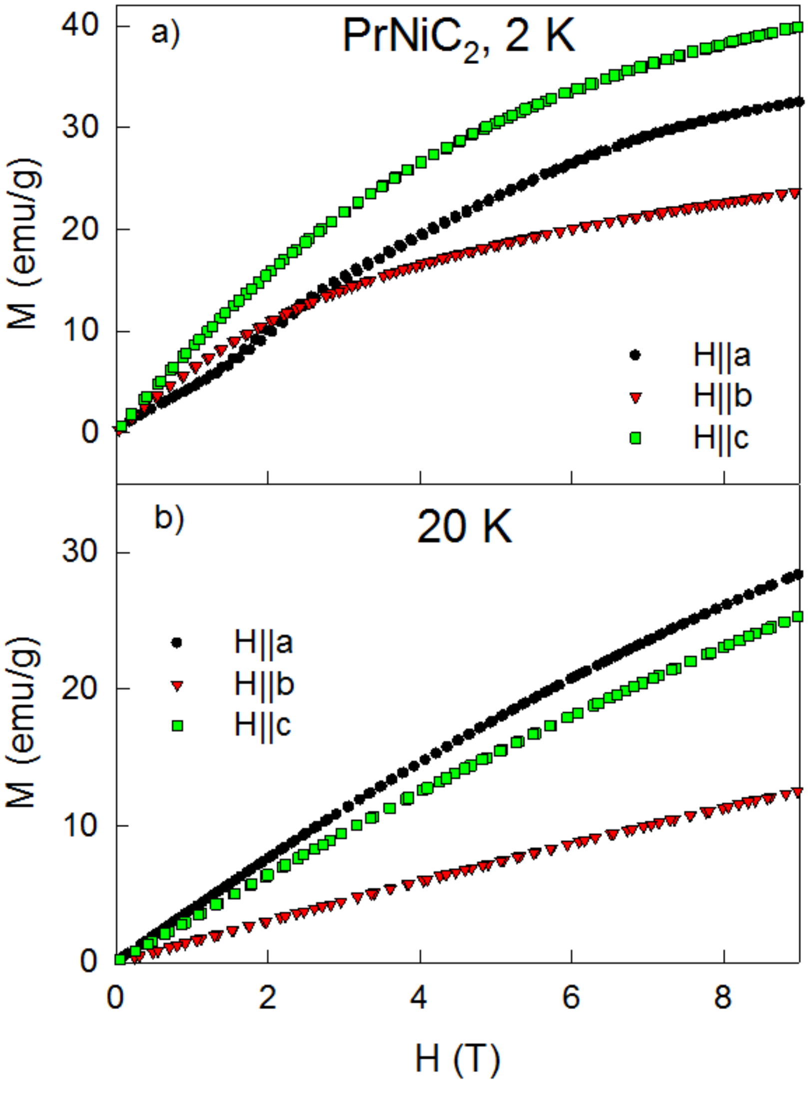

Figure 32: Magnetic field dependent magnetization of $PrNiC_2$ measured for all crystallographic axis at a) 2 K and b) 20 K.

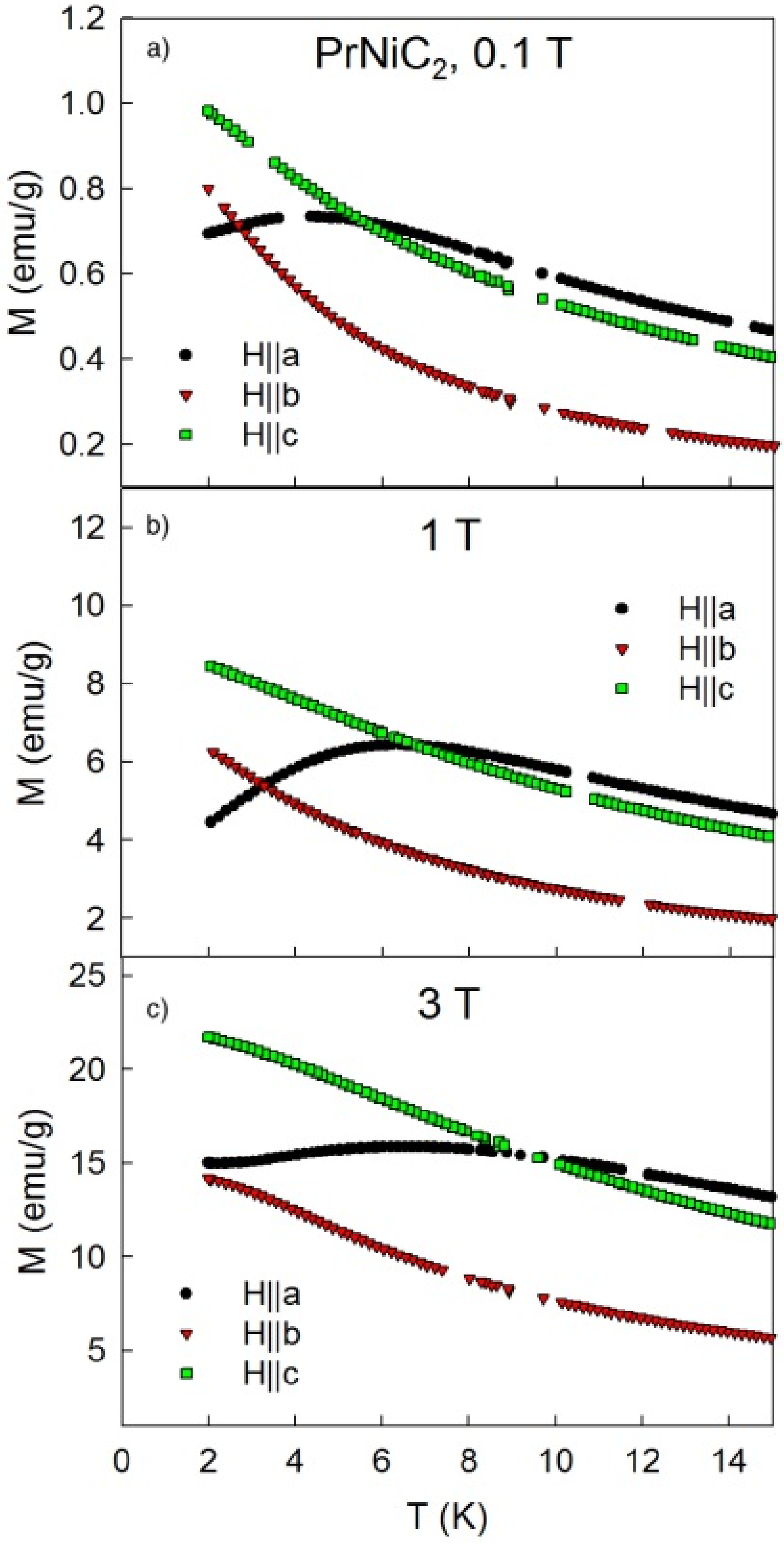

Figure 33: Temperature dependent magnetization of $PrNiC_2$ measured with H parallel to all crystallographic axis with an external magnetic field of a) 0.1 T, b) 1 T and c) 3 T.

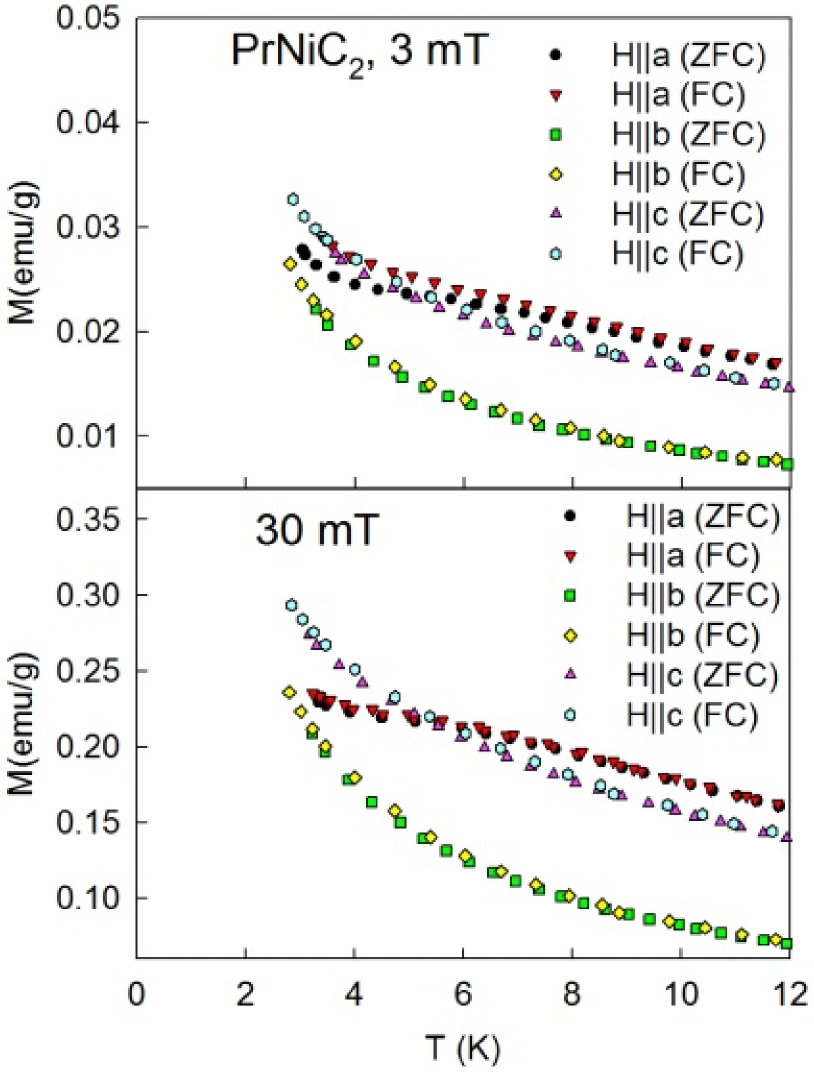

Figure 34: ZFC and FC magnetization with H parallel to the three axes of $PrNiC_2$ with a magnetic field of a) 3 mT and b) 30 mT.

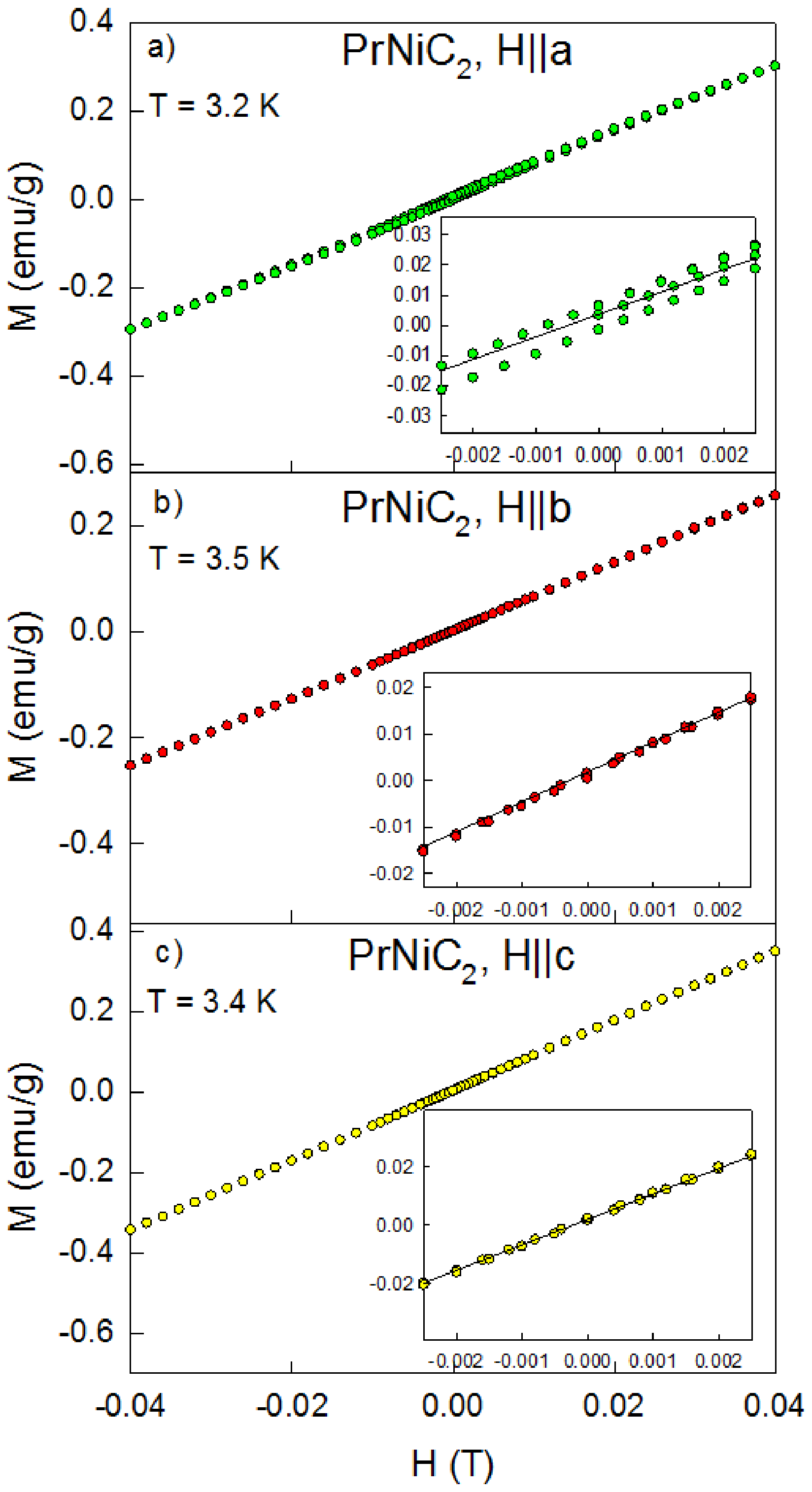

Figure 35: Field dependent, low-field magnetization loop of all three orthorhombic axes of PrNiC$_2$. a) $H||a$. b) $H||b$. c) $H||c$.

5.3 Fitting of the Crystalline Electric Field Parameters

For the purpose of evaluating the influence of the crystal field on the 9-fold degenerate ground state of the $4f^2$ orbital of the Pr^{3+} ion, and obtaining crystal field parameters that were introduced in chapter 2.4.5, experimental data of $PrNiC_2$ was fitted with the software *McPhase* [39]. The experimental data includes the inverse susceptibility obtained from VSM measurements at 1 T and the 4f magnetic specific heat (C_m) as well as the 4f magnetic entropy (S_m). The 4f magnetic specific heat contributions of $PrNiC_2$ are evaluated by subtracting the conduction electron and lattice contributions from the total heat capacity. This can be realized by subtracting the specific heat of $LaNiC_2$ from the measured specific heat of $PrNiC_2$. It is necessary to note, that the Debye temperatures of those two compounds are not the same. In general, the relation of Debye temperatures of two different $RNiC_2$ compounds is dependent on the atomic masses and the volumes per molecular unit. An approximation can be made with following equation:

$$\left(\frac{\Theta_{\mathrm{D}}(A)}{\Theta_{\mathrm{D}}(B)}\right) = \left(\frac{m_{\mathrm{A}}}{m_{\mathrm{B}}}\right)^{\frac{1}{2}} \left(\frac{V_{\mathrm{B}}}{V_{\mathrm{A}}}\right)^{\frac{1}{3}}, \tag{5.1}$$

whereby Θ_{D} is the Debye temperature, m is the molecular mass of the compound and V represents volume per molecular unit. This approximation is based on relations of physical quantities under consideration of a linear chain of atoms, whereby $\Theta_D \propto \omega_D = c * \sqrt[3]{N/V}$ and $c \propto 1/\sqrt{m}$, with the Debye frequency ω_D, the velocity of sound c and the number of atoms N. In the case of $PrNiC_2$, before subtracting the heat capacity of $LaNiC_2$, the temperature grid points of $LaNiC_2$ have to be shifted by the factor ~ 1.02 in order to correctly scale the Debye temperature Subsequently, the magnetic entropy is calculated with:

$$S_{\mathrm{m}}(T) = \int_0^T \frac{C_{\mathrm{m}}}{T'}\, dT' \tag{5.2}$$

The total entropy gain at room temperature $S_m(300\mathrm{K}) = 16.8$ J/molK closely approaches the total expected magnetic entropy gain of the $J = 4$ ground state multiplet $S_{mtot} = \mathrm{Rln}(9) = 18.3$ J/molK, with $R = 8.314$ J/molK being the gas constant.

Using *McPhase* [39], simultaneous fits of the inverse susceptibilities χ^{-1} of all three orientations ($H||a$, $H||b$, $H||c$), the magnetic entropy S_m(T) and the magnetic specific heat contribution C_m(T) were performed with respect to the nine CEF parameters B_l^m by which the non-spheric Coulomb potential acting on the 4f ground state of Pr^{3+} is described. The software uses a simulated annealing algorithm to fit the experimental data with the CEF model. This is an iterative optimization method that uses random walk through a user-defined parameter space in order to find a minimum of the mean quadratic deviation (χ^2). Starting with an initial set of parameters, the Hamiltonian which was discussed in chapter 2.4.5, and on that basis χ^{-1}, C_m and S_m are computed and compared to the measurement data *via* χ^2. The initial parameters are changed by a randomly generated step width and χ^2 is calculated with the new parameter set once more. With an acceptance function that is proportional to the statistical temperature, it is decided whether the new point is accepted or rejected. A more detailed explanation of the simulated annealing algorithm is given in Ref. [85].

Table 4: Energy splitting computed with the aid of *McPhase* [39].

Energy Level	Energyeigenstate [meV]
Δ_0	0
Δ_1	1.09
Δ_2	3.40
Δ_3	6.44
Δ_4	29.33
Δ_5	31.33
Δ_6	31.53
Δ_7	33.00
Δ_8	46.46

For the fits, a temperature independent Pauli paramagnetic component of 3.8×10^{-4} emu/mol was considered. For the sake of limiting the number of parameters to a minimum, molecular field parameters were not yet taken into account. The best fits of the inverse susceptibilities, as well as of the concurrently fitted C_m and S_m are shown in Fig. 36 and Fig. 37 respectively. The CEF parameters of this fit were identified with $B_2^0 \simeq$ -7.7×10^{-2} meV, $B_2^2 \simeq$ -3.2×10^{-1} meV, $B_4^0 \simeq 1.7\times10^{-2}$ meV, $B_4^2 \simeq$ -2.7×10^{-3} meV, $B_4^4 \simeq$ -1.7×10^{-2} meV, $B_6^0 \simeq$ -2.2×10^{-4} meV, $B_6^2 \simeq 1.0\times10^{-4}$ meV, $B_6^4 \simeq$ -8.0×10^{-6} meV and $B_6^6 \simeq$ -2.2×10^{-4} meV. This fit reveals an energy level scheme of 9 singlet states. The corresponding splitting of the energy states is given in Table 4, whereby more precise information on the higher-order crystal field parameters is necessary to evaluate the energy splitting more accurately.

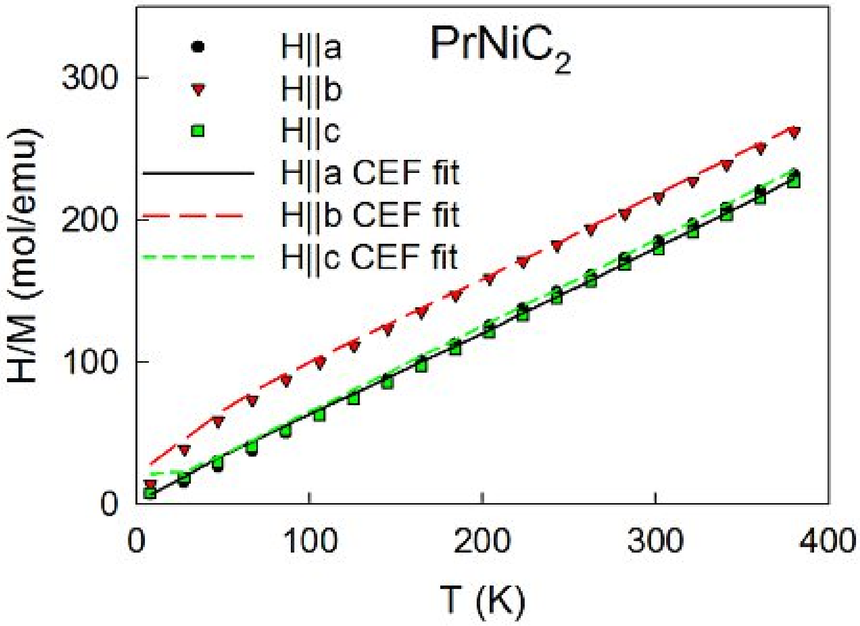

Figure 36: Temperature dependent inverse susceptibility of $PrNiC_2$ given as symbols and the CEF fits indicated with lines.

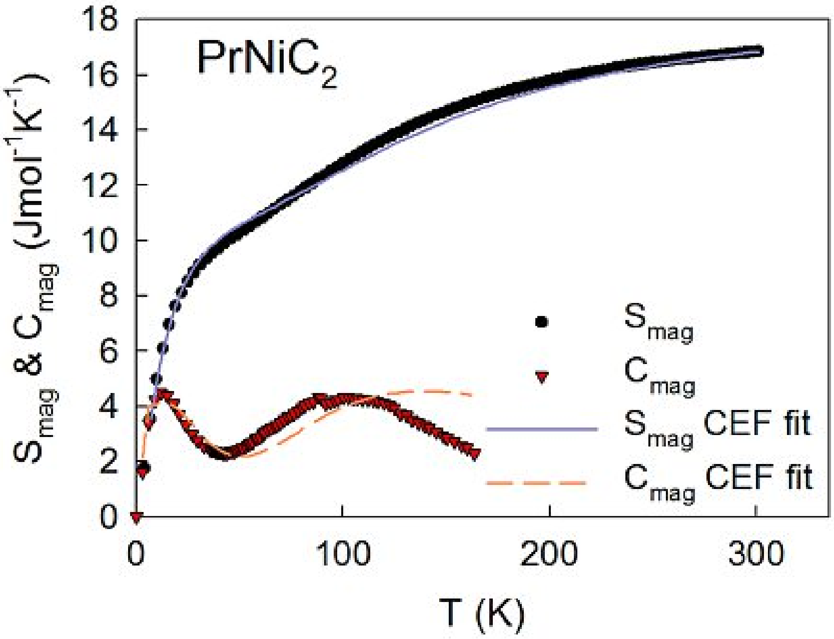

Figure 37: Temperature dependent magnetic entropy and magnetic specific heat of PrNiC$_2$ given as symbols (see text for details of evaluation) and the CEF fits indicated with lines.

Summary

Studies of magnetic and thermodynamic properties of PrNiC$_2$ reveal a paramagnetic behavior above 0.4 K and no spin glass phase can be identified. The inverse magnetic susceptibility, the magnetic entropy and magnetic specific heat were fitted with the CEF model implemented in *McPhase* [39] using a simulated annealing algorithm. The crystalline electric field lifts the degeneracy of the 9-fold 4f^2 ground state into 9 singlets with an approximate splitting of 1 meV to the first excited state and a total splitting of about 50 meV.

6 Thermodynamic and Dilatometric Characterization of CDW and Magnetic Phase Transitions

In section 2.1, variables which are of relevance for this chapter have already been defined. The motivation is to observe the impact of magnetic and lattice symmetry changes that are revealed by thermal expansion measurements. With this method, a high-precision determination of the length change and the thermal expansion coefficient is enabled. Therefore, complementary key information is provided by this technique in addition to heat capacity measurements, in which the entropy change is disclosed and single crystal X-ray diffraction at various temperatures, which is carried out by Berthold Stöger at the X-ray center of the TU Wien, revealing that in the incommensurate CDW phase Ni atom displacements (as compared to the orthorhombic parent structure positions) appear only in the orthorhombic bc-plane [86], whereas in the commensurate CDW phase, Ni atom displacements have been demonstrated to occur predominantly along the a-axis [4] while displacements in the bc-plane are negligible. The advantages of thermal expansion measurements over X-ray diffraction include a much enhanced relative temperature dependent resolution of length changes and a more precise temperature regulation.

6.1 State of the Art of Thermal Expansion Studies of CDW Systems

Despite extensive studies of intermetallic rare-earth nickel dicarbides already exist in literature, there focus is predominantly set on the magnetic and electric properties rather than on the thermoelastic characteristics of these materials. On the contrary, for other charge density wave systems like $NbSe_2$ [87] or $LaPt_2Si_2$ [88], thermal expansion measurements have been undertaken and analyzed, also with regard to the Ehrenfest relation. Most recently, the coexistence of the superconducting state and the charge density wave state in $Lu(Pt_{1x}Pd_x)_2In$ attracted a lot of attention [89]. In Ref. [89, 90] it is reported about an increase of the CDW temperature with the application of pressure, which is stated to be an unusual feature of these compounds. Furthermore, phenomenological approaches of the thermodynamic properties of CDW systems have been published, *c.f.* Ref. [27, 28]. Thermal expansion measurements do not only give insight into the nature of first and second order CDW transitions but also into magnetic ordering transitions which are accompanied by a lattice deformation due to spontaneous magnetostriction. Whereas a phase transition of first order is usually manifested by a step-like anomaly, the transition of second order is characterized by a kink-like anomaly. The distinction between incommensurate and commensurate phase transitions is made feasible by the available X-ray diffraction results [7, 17, 86, 91].

At the institute, a few thermal expansion studies of single crystalline $RNiC_2$ cubes have been conducted before by Marta Roman [92]. These include crystals of $YNiC_2$, $NdNiC_2$ and $LuNiC_2$. During this master thesis, the data was complemented with studies of $PrNiC_2$, $GdNiC_2$, $DyNiC_2$, $HoNiC_2$ and $LuNi_{0.92}Co_{0.08}C_2$ and available resistivity measurements that have been conducted earlier at the institute, will be shown. Therefore, a broad spectrum of different materials containing light and heavy rare-earth elements and magnetic as well as non-magnetic compounds were investigated. All these samples were single crystal cubes and the length changes of all three orthorhombic crystalline orientations was measured in order to reveal the distinctive behavior at a phase transition. The presentation of the obtained experimental data is split into three parts. The first part will cover the characteristics of the first and second order charge density wave transitions. Then, the Clausius-Clapeyron (Eq. 2.12) and a modified Ehrenfest relation (Eq. 2.18) will be used to determine the pressure and stress dependencies of the charge density wave temperatures ($T_{lock-in}$ and T_{CDW}) of three materials in each case, where for $PrNiC_2$, $GdNiC_2$, $DyNiC_2$, $HoNiC_2$ and $YNiC_2$ the $T_{lock-in}$ and T_{CDW} correspond to commensurate CDW to incommensurate CDW and incommensurate CDW to orthorhombic transition, respectively. Lastly, the low temperature data which reveals magnetic phase transitions will be discussed.

6.2 Characteristic Features of Commensurate and Incommensurate CDW Phase Transitions in $RNiC_2$

$PrNiC_2$

After Murase *et al.* [7] firstly observed anomalies in the electrical resistivity and, *via* X-ray diffraction, in the lattice constants for several $RNiC_2$ in 2004, Yamamoto *et al.* [79] reported about a CDW transition of $PrNiC_2$ at 89 K. At this temperature, the orthorhombic parental lattice undergoes a incommensurate CDW transition. The magnetic properties were studied by Onodera *et al.* [77]. $PrNiC_2$ is considered to be a van Vleck paramagnet and no magnetic ordering could be identified for temperatures above 2 K.

Firstly, the results of the thermal expansion measurements of all three crystallographic orientations of $PrNiC_2$ are presented. In panel a) of Fig. 38, the temperature dependent specific heat as C/T is shown and in b) and c) the relative length change dl/l as well as the thermal expansion coefficient α are plotted respectively. While the a-axis steadily increases with rising temperatures, the b-axis only elongates minimally. Upon warming, between 4.2 K and approximately 70 K, the c-axis continuously shortens, whereas afterwards it lengthens monotonically. At 300 K, the elongation of the a-axis is largest, followed by c and b. Rather significant length changes are observed for $T < 50$ K and attributed to crystalline electric field effects when approaching the singlet ground state.

A charge density wave transition of second order is remarkable in the present measurements at a temperature of about 89 K. The transition is highlighted in insert of panel c) in Fig. 38 showing α, whereas in dl/l, the small change in slope is not easily visible. As defined in chapter 2.1, the thermal expansion coefficient corresponds to the first derivative of the change in length with respect to temperature $\alpha = 1/l * dl/dT$. According to above-mentioned diffraction study [79], this CDW transition corresponds to an orthorhombic to incommensurate structure phase transition, meaning the periodic displacement of atoms in the CDW cannot be described with a rational factor of the lattice vector but with an irrational factor. At the phase transition, the dimensions of a and b shorten while c is enlarged. It is apparent that the modifications of the b- and c-axis are larger than the one of a-axis which seems to manifest a characteristic feature of this orthorhombic to monoclinic phase transition.

The thermal expansion of the *b*-axis was measured twice, as puzzling small anomalies at $\sim$ 50 K, $\sim$ 151 K, $\sim$ 184 K and $\sim$ 273 K. These anomalies display a magnitude of the order of 10^{-6} or smaller which is a typical magnitude of artefacts of *e.g.* H_2O at 273 K or maybe result from friction or tilting effects of the sample inside the dilatometer cell. These anomalies have no obvious correspondence to any other measured quantities as *e.g.* the heat capacity or resistivity. Therefore, the charge density wave transition remains the only identifiable phase transition in the thermal expansion of $PrNiC_2$.

An electrical resistivity measurement of $PrNiC_2$ with the current applied along the orthorhombic *a*-axis has already been measured earlier [82] and the data is shown in Fig. 39. The resistivity increases with rising temperatures. The temperature independent residual resistivity ρ_0 accounts for approximately 0.18 $\mu\Omega$m. Likewise, only the incommensurate charge density wave transition at 89 K is visible. Upon warming through the CDW, the resistivity of the *a*-axis decreases abruptly which signifies the closing of the CDW gap when entering the unmodulated orthorhombic symmetry.

The thermal expansion of $NdNiC_2$ measurements that have been conducted by Marta Roman [92] show similar characteristics of the second order charge density wave transition at 121 K. The thermal expansion coefficient reveals a smaller modification of the *a*-axis than of the *b*- and *c*-axis.

$GdNiC_2$

In literature, the transition temperatures $T_{lock\text{-}in}$ and T_{CDW} of $GdNiC_2$ were initially reported by Murase *et al.* [7] and were confirmed by Shimomura *et al.* [91]. At 205 K, the orthorhombic to incommensurate CDW and at 90 K, the incommensurate CDW to commensurate CDW phase transition was observed with X-ray diffraction [91]. An antiferromagnetic ground state is displayed below the magnetic transition temperature $T_N = 20$ K [91].

In Fig. 40, the temperature dependent specific heat, the thermal expansion and the thermal expansion coefficient of $GdNiC_2$ are depicted in panels a), b) and c) respectively. The antiferromagnetic ordering transition is detected at $\sim$ 22 K. In the high-temperature range, two anomalies are remarkable. Firstly, the kink at $\sim$ 86 K marks a phase transition of first order which corresponds to the lock-in transition [91]. At this temperature, the wave length of the CDW modulation can be expressed by a rational fraction that has the same periodicity as the basis structure of the crystal lattice and is therefore commensurate. The transition is often is designated as commensurate CDW to incommensurate CDW transition [28]. While upon warming, the lattice parameters *a* and *c* are elongated, the *b*-axis dimension shortens. The first order lock-in transition is more distinctive than the second order charge density wave transition and can be easily identified not only in α but also in dl/l. From the measurements, the step-like second order phase transition is identifiable at approximately 200 K which is in accordance with the observed orthorhombic to incommensurate CDW structure transition in Ref. [91]. At this temperature, the side lengths *a* and *b* of the cube increase and *c* decreases. The same above-mentioned characteristic of *b* and *c* changing in a greater extent than *a* is noticeable. This observation conforms to the results of single crystal X-ray diffraction

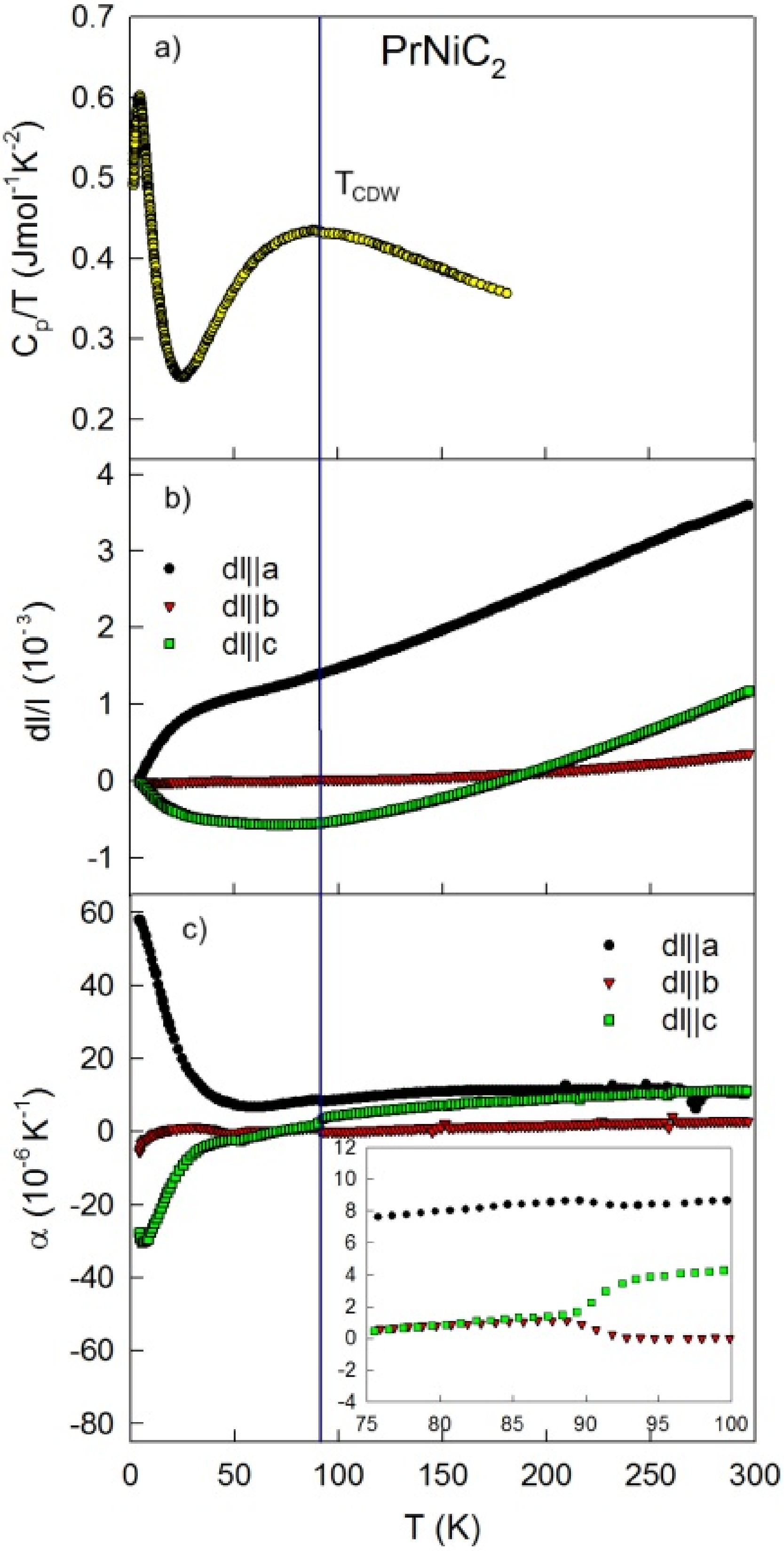

Figure 38: a) Temperature dependent specific heat of PrNiC$_2$ divided by T. b) Relative length change and c) thermal expansion coefficient α with a close-up in the inset.

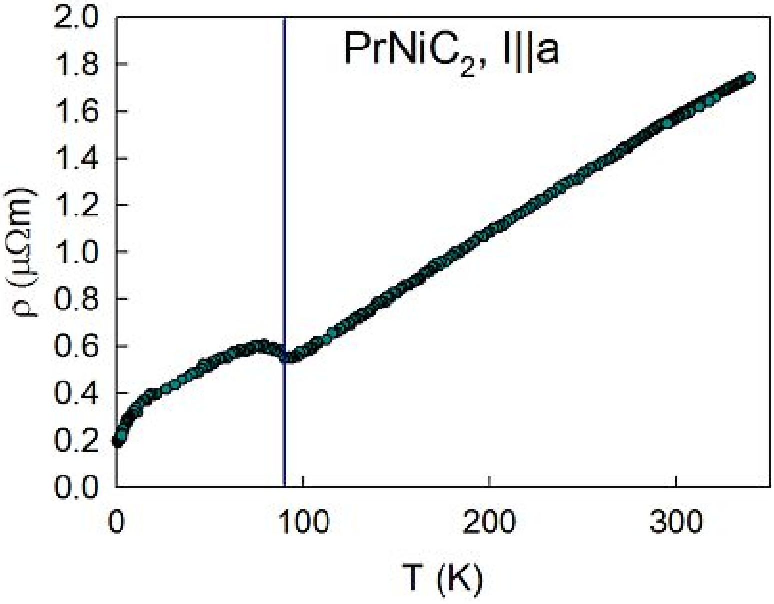

Figure 39: Resistivity of $PrNiC_2$ with current applied along the a-axis [82].

that the significant displacements occur at the orthorhombic to incommensurate transition within the bc-plane rather than along the a-axis. Subtracting the influence of magnetism at low temperatures, the relative length changes of each lattice parameter at room temperature account for $\sim 3\times10^{-3}$ for a and approximately 1×10^{-3} for b and c.

$DyNiC_2$

Roman *et al.* [8] firstly reported about the CDW transitions of polycrystalline $DyNiC_2$ at temperatures of $T_{lock\text{-}in} = 232$ K and $T_{CDW} = 284$ K. Maeda *et al.* [17] initially performed single-crystal X-ray-diffraction experiments of $DyNiC_2$ and observed the orthorhombic to incommensurate phase transition at 270 K and a commensurate satellite reflection at 225 K. $DyNiC_2$ exhibits an antiferromagnetic ground state below 7.6 K [93].

The heat capacity, the thermal expansion and the thermal expansion coefficient are shown in Fig. 41 in panels a), b) and c) respectively. The heat capacity measurement was conducted by Michael Sandrieser [94]. The magnetic phase transition is discovered at 7.6 K which conforms to the above-mentioned T_N. Like in $GdNiC_2$, at room temperature the axis with the largest length change is a, then b and c. The first order lock-in transition, as well as the second order phase transition are also both apparent in the thermal expansion measurements of $DyNiC_2$. The distinctive kink at 219 K points at the lock-in transition. The a- and b-axis are expanding abruptly, while the c-axis shortens. It is identifiable that the positive changes in length of a and b are in total greater than the shortening of the orthorhombic c-axis. Hence, a change in volume arises at this transition temperature. The step-like anomaly at 291 K indicates the second order phase transition. Other than at the lock-in transition, at T_{CDW}, the a and c orientations of the single crystalline cube elongate and b decreases in size. Again, the length change of a is smaller than the change of b and c.

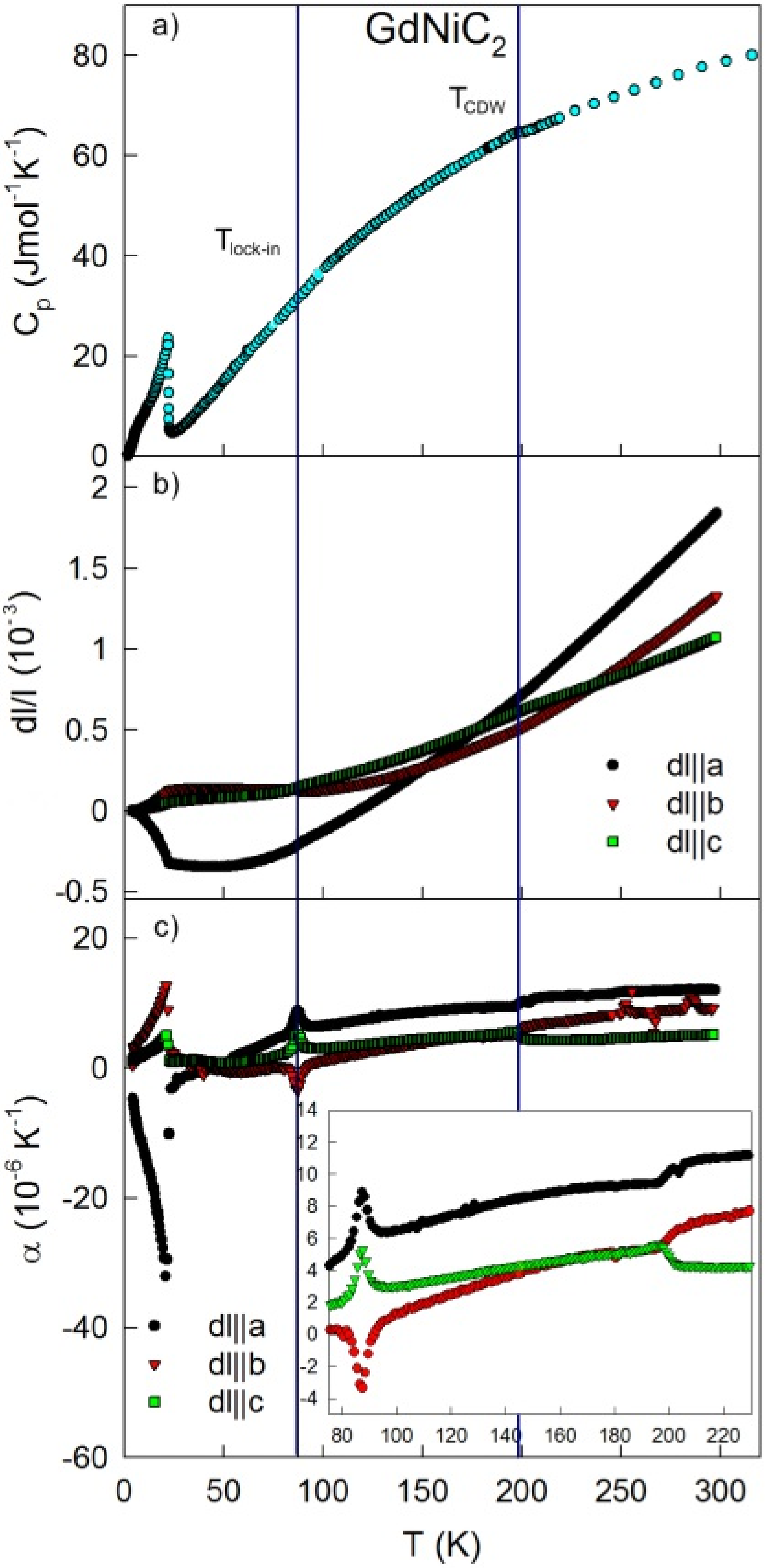

Figure 40: a) Temperature dependent specific heat of GdNiC$_2$, b) relative length change and c) thermal expansion coefficient α with a close-up in the inset.

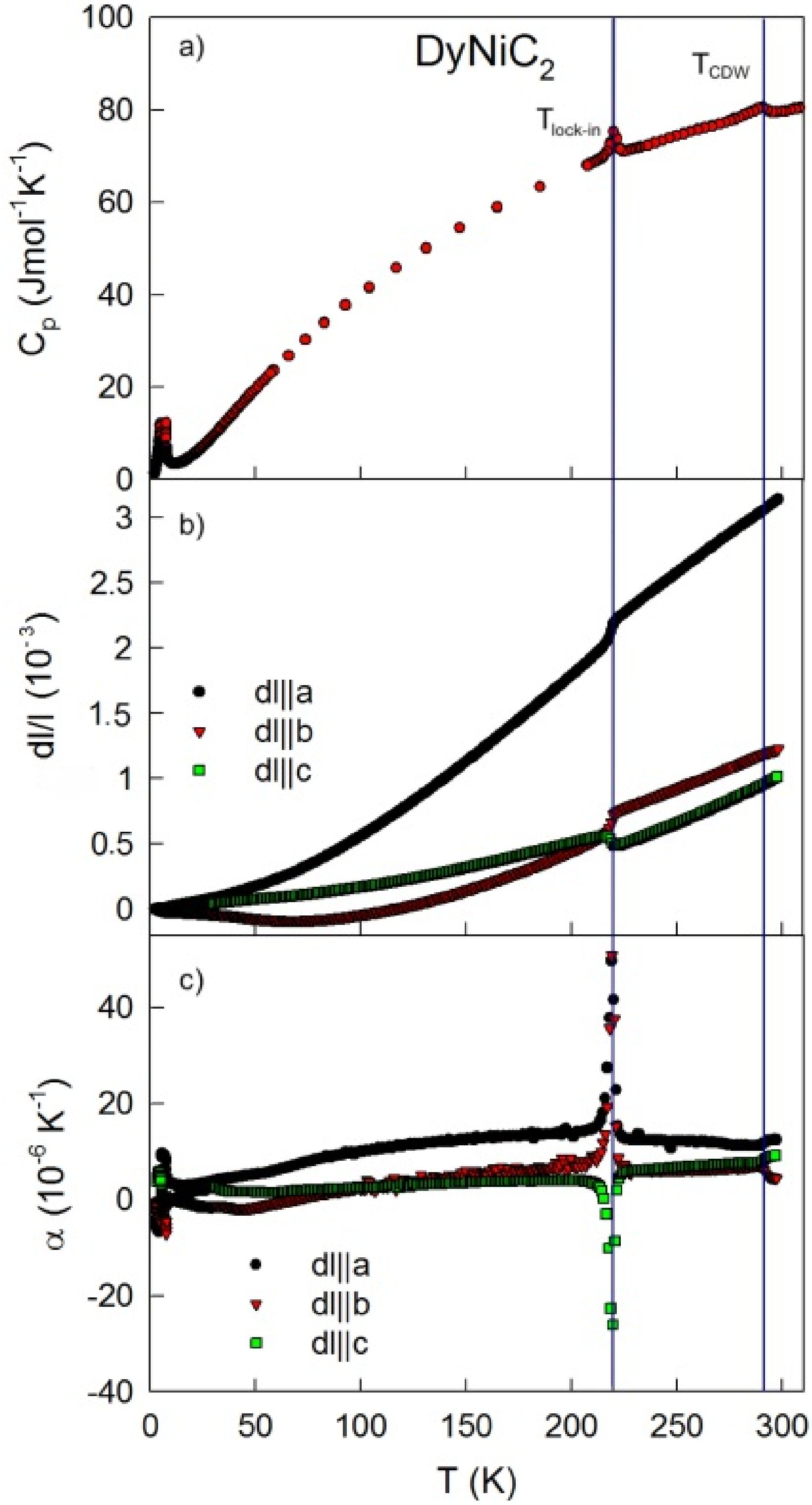

Figure 41: a) Temperature dependent specific heat of $DyNiC_2$ which was measured by Sandrieser [94], b) relative length change and c) thermal expansion coefficient α.

$HoNiC_2$

$HoNiC_2$ exhibits an antiferromagnetic ground state with a Néel temperature of 2.78(6) K [95, 96]. In Ref. [96], a second order charge density wave transition of polycrystalline $HoNiC_2$ was initially observed at 317 K and a lock-in transition was identified at 291 K [8]. Maeda *et al.* [17] reported about a commensurate phase transition in single crystalline $HoNiC_2$ at 295 K.

Due to the high Peierls temperature of $HoNiC_2$, the thermal expansion measurements could only track the lock-in transition. The results of the second single crystalline $HoNiC_2$ cube are presented in Fig. 42, whereby in a) the specific heat, in b) the temperature dependent relative length change and in c) α is plotted. The first $HoNiC_2$ crystal that was intended to be measured had cracks which consequently lead to a damage of the cube. Therefore, merely the expansion of one side length could be examined. Consequently, a second crystal had to be grown and the thermal expansion of all three crystallographic axes could be measured. The comparison of the thermal expansion measurements of the b-axis of both crystals will be presented in Appendix I. While upon warming, the change in length is constantly positive for the a- and b-axis throughout the measured temperature range, the c-axis displays a non-monotonous behavior. For all temperatures, the expansion of the crystallographic a direction is largest, followed by b and subsequently c. At room temperature, the relative length change of a amounts to 3×10^{-3} and dl/l of b and c accounts for $\sim 1\times10^{-3}$. An anomaly is remarkable at approximately 295 K which indicates the first order lock-in transition. At this phase transition, a and b significantly enlarge to a higher extent than c shortens. It is remarkable that the change in length of the lattice parameter a is largest. The charge density wave transition is not visible in these measurements as it is discovered at higher temperatures of around 315 K as mentioned above. Multiple small other kinks are observable, *i.e.* at 43 K, 181 K or 228 K. These irregularities can be identified to be measurement errors and thus have no significance.

$LuNi_{0.92}Co_{0.08}C_2$

While for $LuNiC_2$ the commensurate CDW transition was ascertained at 450 K [4], for $LuNi_{0.92}Co_{0.08}C_2$ this transition was measured at a temperature of $\sim$ 301 K [74]. No long-range magnetic ordering is expected nor found in these materials [4].

According to the 4f electron count, the single crystalline cube of $LuNi_{0.92}Co_{0.08}C_2$ was the final one that was measured in the miniature capacitance dilatometer during this master thesis. The relative change in length and the thermal expansion coefficient are shown in panels a) and b) of Fig. 43 respectively. In general, the relative expansion of the cube along the orthorhombic a-axis is largest with 3×10^{-3} at room temperature. The thermal expansions of the b-axis and c-axis display a similar behavior. Above $\sim$ 210 K, the b-axis starts to elongate stronger than the c-axis. The thermal expansions of all three orientations are nearly indistinguishable below 30 K. Above 30 K, the elongation of the a-axis gets more pronounced. At 50 K, an abrupt change in the slope is remarkable for all three crystallographic directions. It is believed that this bump is due to ferromagnetic impurities in the crystal. In magnetic susceptibility measurements, which were discussed in chapter 4, this anomaly was visible as well. An anomalous behavior

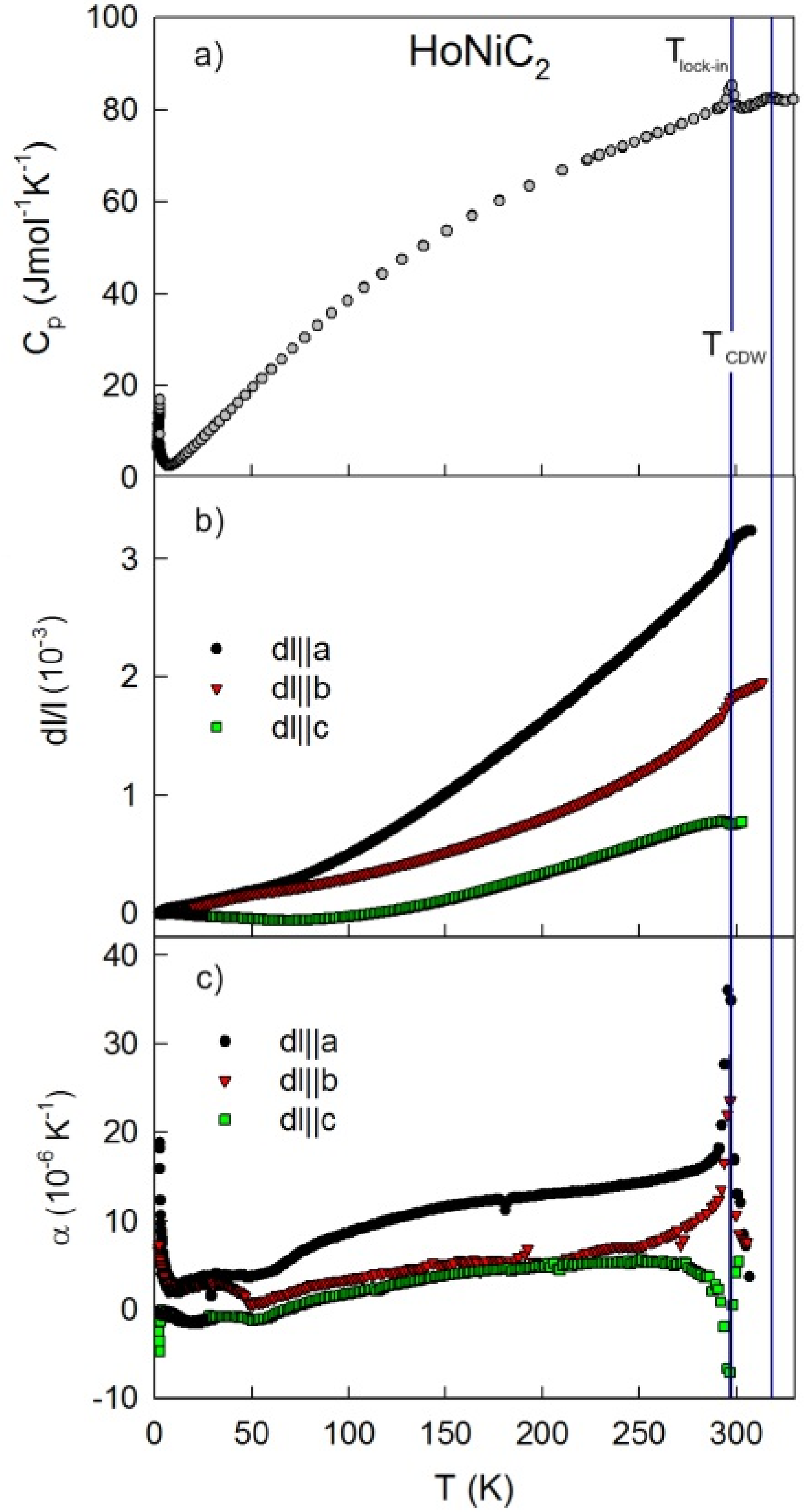

Figure 42: a) Temperature dependent specific heat of $HoNiC_2$, b) relative length change and c) thermal expansion coefficient α.

near room temperature is observed which conforms with the anomalies in resistivity and heat capacity. The thermal expansion coefficient reveals broad transitions in the a and b dimensions and a sharp double transition in c, whereby one of the kinks in the double transition may be an artefact due to H_2O. This broad anomaly may be linked to the charge density wave transition.

At the institute, the thermoelastic properties of two other single crystalline cubes, including $LuNiC_2$ and $YNiC_2$, were investigated by Marta Roman [92]. For $LuNiC_2$, only the thermal expansion of the orthorhombic a direction was measured but due to the comparably high transition temperature of 450 K, *c.f.* Ref. [4], the charge density wave transition could not be discovered. Moreover, no other anomalies that could point at a phase transition were identified. Extensive studies of both, the thermal expansion and the resistivity of all three axes were performed for $YNiC_2$. Not only the lock-in but also the incommensurate charge density wave transition is apparent in the acquired data. This behavior has already been observed in $GdNiC_2$, $HoNiC_2$ and $DyNiC_2$. Furthermore, similarities of a more distinct change in the length of the b and c lattice parameters at T_{CDW} in contrast to a was discovered. Oppositely, at the lock-in transition the length change of a was noticed to be most pronounced.

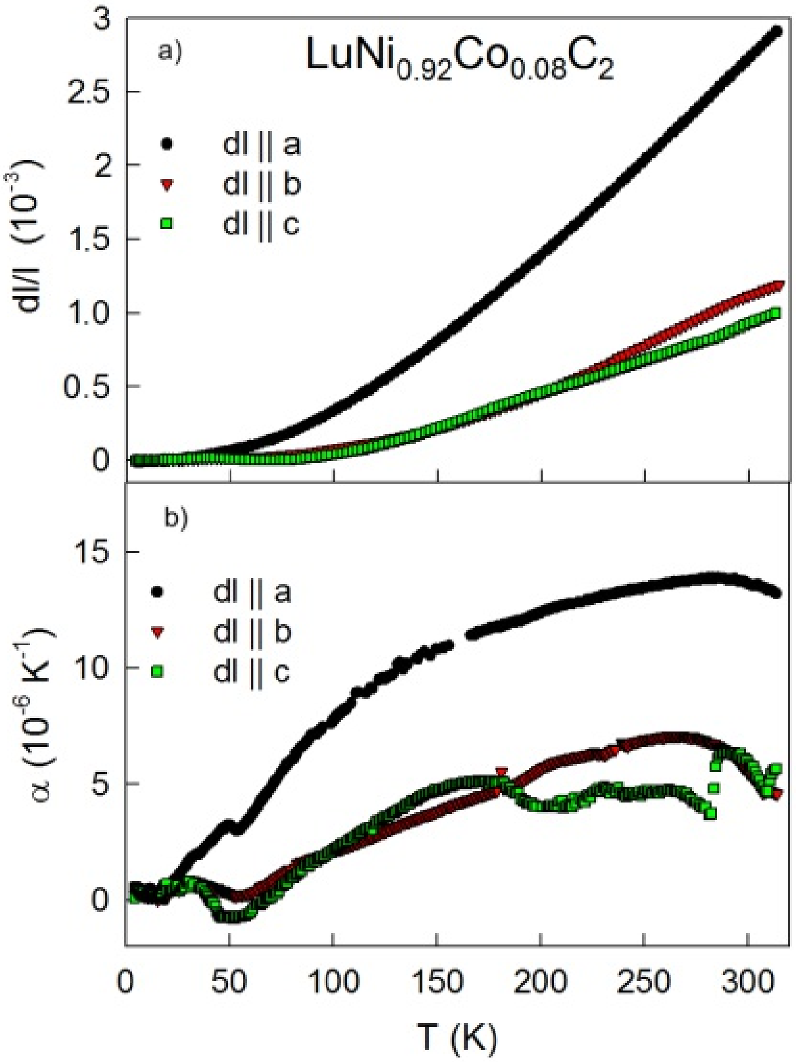

Figure 43: Thermal expansion of the $LuNi_{0.92}Co_{0.08}C_2$ single crystalline cube. a) Relative length change and b) thermal expansion coefficient α.

6.3 Application of the Clausius-Clapeyron and Ehrenfest Relation

The Clausius-Clapeyron relation, which applies to a reversible phase transition of first order was introduced in chapter 2.2. Furthermore, a modified Ehrenfest relation for second order phase transitions at the charge density wave temperature for low-dimensional metals was schematically reviewed in the same chapter. Eq. 2.18 can be rewritten in order to determine the uniaxial pressure (strain) derivative of the CDW transition temperature from experimental results of the specific heat and thermal expansion measurements:

$$\frac{\partial T_{\mathrm{CDW}}}{\partial \sigma_{\mathrm{i}}} = \Delta\alpha_{\mathrm{i}} V_{\mathrm{m}} \frac{T_{\mathrm{CDW}}}{\Delta C_{\mathrm{p}}} \tag{6.1}$$

In the following passage, the procedure of determining the required variables for calculating dT/dp and $\partial T_{CDW}/\partial\sigma_i$ will be explained.

The molar volume of the $\mathrm{RNiC_2}$ compounds is evaluated by:

$$V_{\mathrm{m}} = \frac{V_{\mathrm{cell}}}{2} * N_{\mathrm{A}}, \tag{6.2}$$

with the Avogadro constant N_A and the volume of the unit cell (V_{cell}) of the material which can be attained *e.g.* from Ref. [97]. Due to the structure of the orthorhombic unit cell, which contains two formula units ($\mathrm{R_2Ni_2C_4}$), a division by two is necessary.

The change in entropy at the first-order charge density wave transition is determined by plotting C_p/T in dependence of the temperature and estimating the area under the curve at the anomaly, as shown in Fig. 44 for $\mathrm{DyNiC_2}$.

The change in volume at the first order phase transition is determined by adding up the relative length changes of all three crystallographic directions at the transition. As ΔS was evaluated graphically in the units of J/molK, the sum has to be multiplied by the molar volume of the material. The relative length changes at $T_{lock-in}$ are estimated in an analogous manner as ΔC_p and $\Delta\alpha$, which will be described below.

Acquiring the jump in the specific heat capacity and in the thermal expansion coefficient will be demonstrated by the example of $\mathrm{GdNiC_2}$. In Fig. 45, a close-up of the heat capacity around T_{CDW} in J/molK is shown. Appropriate temperature ranges above and below T_{CDW} were selected to approximate the data points with two separate linear fits in the best possible way. These fits are represented with the solid and dashed lines. Then, the difference between the specific heat at T_{CDW} is computed using the fits. The vertical solid line symbolizes an idealized transition yielding ΔC_{p}.

The jump in the thermal expansion coefficient is evaluated in the exactly same manner. The experimental data of $\mathrm{GdNiC_2}$ with the elongation in length measured parallel to the c-axis is presented in Fig. 46. Based on these two examples, it appears that the accuracy of the calculated values of ΔC_{p} and $\Delta\alpha$ is highly dependent on the quality of the measurements. A signal that is too noisy is accountable for a more imprecise linear fit and thus for an inaccurately evaluated difference. Another detail that is of importance is the density of the measurement points. The estimation of the charge density wave temperature will be eased with closer data points.

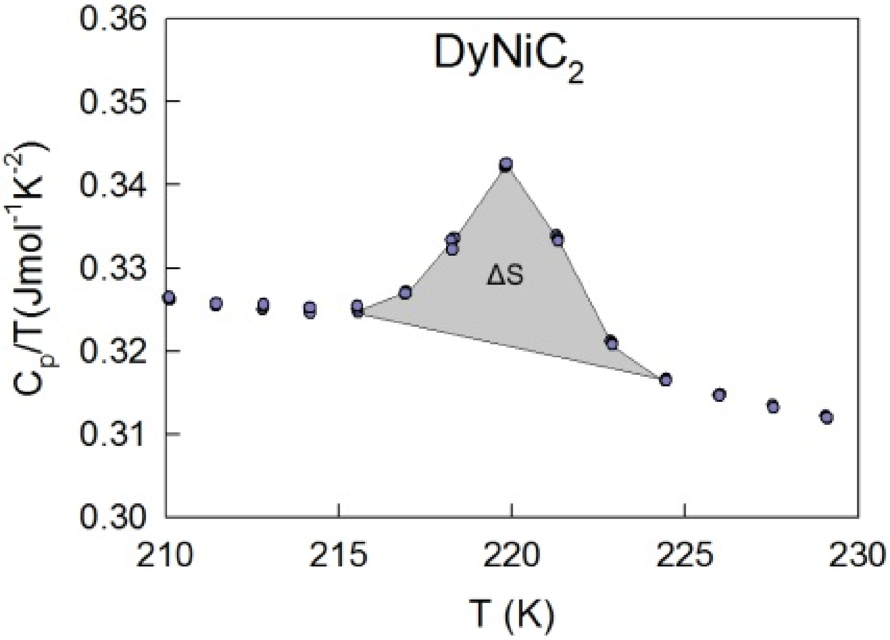

Figure 44: Graphical evaluation of ΔS at the first order CDW phase transition of DyNiC$_2$.

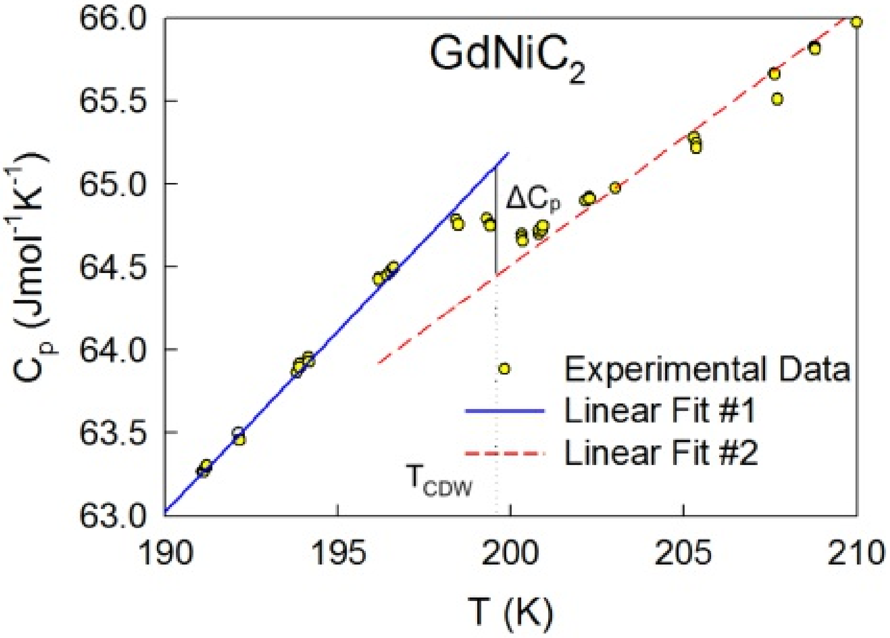

Figure 45: Graphical evaluation of ΔC_p at the second order CDW phase transition of GdNiC$_2$.

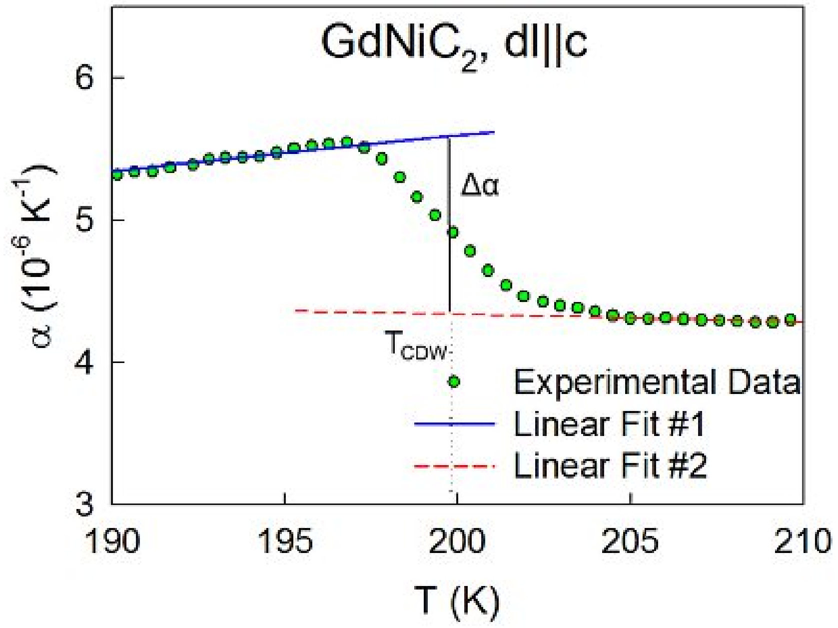

Figure 46: Graphical evaluation of $\Delta\alpha_\mathrm{c}$ at the second order CDW phase transition of GdNiC$_2$.

Clausius-Clapeyron Relation

The first order phase transition at $T_{lock-in}$ was investigated for GdNiC$_2$, DyNiC$_2$ and HoNiC$_2$. The pressure dependence of the critical temperature was calculated with the inverse of the Clausius-Clapeyron relation (Eq. 2.12). The estimated values of ΔS and ΔV and the subsequently calculated relation between the pressure and the temperature are listed in Table 5. Upon cooling, the change in entropy at the transition is negative as well as the change in volume and thus the pressure dependence of the critical temperature is positive. As a consequence, the first order charge density wave transition can be shifted to a higher temperature with an increase in pressure.

Table 5: Change in entropy, ΔV and calculated dT/dp of GdNiC$_2$, DyNiC$_2$ and HoNiC$_2$ at $T_{lock-in}$.

Material	ΔS [J/molK]	ΔV [10^{-9} m^3/mol]	$dT_{lock-in}/dp$ [K/kbar]
GdNiC$_2$	-0.0010(2)	-0.575(60)	56(1)
DyNiC$_2$	-0.075(10)	-3.95(40)	5.3(5)
HoNiC$_2$	-0.045(7)	-6.58(70)	14.7(8)

Modified Ehrenfest Relation

The discontinuities at T_{CDW} were examined for PrNiC$_2$, GdNiC$_2$ and DyNiC$_2$. For these materials, the specific heat measurement as well as the thermal expansion measurements were conducted up to the Peierls temperature. In Table 6, the molar volume of the compound, T_{CDW}, the evaluated ΔC_p and $\Delta\alpha_\mathrm{i}$ upon cooling are listed. The resulting uniaxial pressure derivatives of T_{CDW} are given in Table 7.

Table 6: Molar volume, T_{CDW}, ΔC_p and $\Delta\alpha_\mathrm{i}$ of $PrNiC_2$, $GdNiC_2$ and $DyNiC_2$.

Material	V_m [10^{-6} m^3/mol]	T_{CDW} [K]	ΔC_p [J/molK]	$\Delta\alpha_\mathrm{i}$ [10^{-6} 1/K]		
				a	b	c
$PrNiC_2$	32.20	89	0.095(15)	0.61(7)	0.45(5)	-1.93(20)
$GdNiC_2$	30.17	200	0.698(104)	-0.81(12)	-1.06(16)	1.27(18)
$DyNiC_2$	29.11	292	1.462(198)	-1.08(16)	2.20(34)	-1.24(18)

Table 7: Stress and pressure dependence deduced at the charge density temperature.

Material	$\partial T_{CDW}/\partial\sigma_i$ [$10^{-9}$$m^2$K/N]			$\partial T_\mathrm{CDW}/\partial p$ [K/kbar]
	a	b	c	
$PrNiC_2$	19(3)	14(2)	-58(10)	-2.6(1)
$GdNiC_2$	-7(2)	-9(1)	1.1(3)	-0.52(2)
$DyNiC_2$	-6(1)	-13(3)	7(2)	-0.09(1)

One the one hand, it is observed that the absolute value of ΔC_p augments with higher charge density wave temperatures and on the other hand, the absolute values of $\Delta\alpha_\mathrm{i}$ do not depend on T_{CDW} and are in the same magnitude for the investigated materials. As a consequence, the pressure dependence of T_{CDW} is higher the lower the charge density wave temperature is. When evaluating jump in the volume coefficient of thermal expansion by summing up the components of each orientation and inserting it into Eq. 6.1, the isotropic pressure dependency can be calculated. The coefficient $\Delta\beta = \text{-}0.87(9)\times10^{-6}$ 1/K for $PrNiC_2$, $\Delta\beta$ = -0.6(1)$\times10^{-6}$ 1/K for $GdNiC_2$ and $\Delta\beta$ = -0.12(1)$\times10^{-6}$ 1/K for $DyNiC_2$. It is apparent, that upon cooling the volume of each compound is shortened at the second order phase transition and the total change of the volume coefficient depends on T_{CDW}. Moreover, following pressure dependencies result: $\partial T_\mathrm{CDW}/\partial p = \text{-}2.6(1)$K/kbar for $PrNiC_2$, $\partial T_\mathrm{CDW}/\partial p = \text{-}5.2(2)\times10^{-1}$ K/kbar for $GdNiC_2$ and $\partial T_\mathrm{CDW}/\partial p = \text{-}9(1)\times10^{-2}$ K/kbar for $DyNiC_2$. The same tendency of a lower pressure dependence with higher charge density wave transition temperature is not only predicted by the anisotropic but also the isotropic thermal expansion coefficient. The pressure dependence of the second order phase transition is negative which conforms to the expectations but signifies an opposing effect to $dT_{lock-in}/dp$ of the first order phase transition.

6.4 Magnetic Phase Transitions

Whereas $PrNiC_2$ exhibits a paramagnetic Pr 4f singlet ground state which leads to a significant electric field effect on the thermal expansion, most of the rare-earth nickel dicarbides display an antiferromagnetic ground state [3, 13, 15]. The magnetic ordering expresses a significant change in the unit cell dimensions of the material which can be noticed in thermal expansion and the corresponding entropy change in the specific heat measurements.

$GdNiC_2$

The low-temperature thermal expansion and heat capacity of $GdNiC_2$ are shown in Fig. 47. In panel a) the specific heat and in b) the temperature dependent relative length change are plotted. In comparison to the already mentioned Néel temperature given in literature, the measured transiton temperature at 22 K is in good accordance. The antiferromagnetic ordering is clearly discernible in both measurements. The easy axis of the magnetic moments is tilted away by 18° from the c-axis and 45° from the a-axis [3]. The magnitude of the magnetic anomaly largely dominates the length changes at the CDW transition and the relative change in length of a is largest. Due to $L = 0$ for Gd^{3+}, it can be excluded that this effect originates from the influences of the crystalline electric field or the particular orientation of the magnetic moments. Instead, the so-called exchange-striction plays a key role in the magnetovolume effects in Gd systems, as reviewed by Lindbaum and Rotter [98]. Magnetic exchange interactions of magnetic moments in the conduction band or of the d-electrons of other elements of the compound are the reason for this magnetostructural effect [98]. It is expected that the exchange-striction of $GdNiC_2$ is largest among the rare-earth nickel dicarbides, as the Gd^{3+} ion has the largest de Gennes factor. The de Gennes factor is defined as: $(g_J - 1)^2 J(J+1)$, whereby g_J labels the Landé factor and it is proportional to the transition temperature.

$DyNiC_2$

The low-temperature thermal expansion and the specific heat of $DyNiC_3$ are displayed in the same manner as for $GdNiC_2$ in Fig. 48. The specific heat was measured by Michael Sandrieser [94]. The observed Néel temperature of 7.7 K conforms to the critical temperature reported in Ref. [93]. The magnetic moments are tilted 45° away from the c-axis and 77° away from a- toward the b-axis [3]. The anomaly at the antiferromagnetic transition is notably smaller than in $GdNiC_2$, whereby also the exchange interaction and thus also the Néel temperature is smaller. Moreover, in comparison to the lock-in transition, the magnetic ordering transition of the quasi-quartet ground state is less pronounced.

$HoNiC_2$

Lastly, the heat capacity and the thermal expansion of $HoNiC_2$ are presented in Fig. 49. Again, the measured Néel temperature at ~ 2.8 K is in high accordance with the already mentioned value in literature. It is remarkable that, in comparison to the other two discussed magnetic transitions, the anomaly of $HoNiC_2$ is the smallest. The low Néel temperature goes hand in hand with a low exchange energy and the transition is less distinct than the first order lock-in transition.

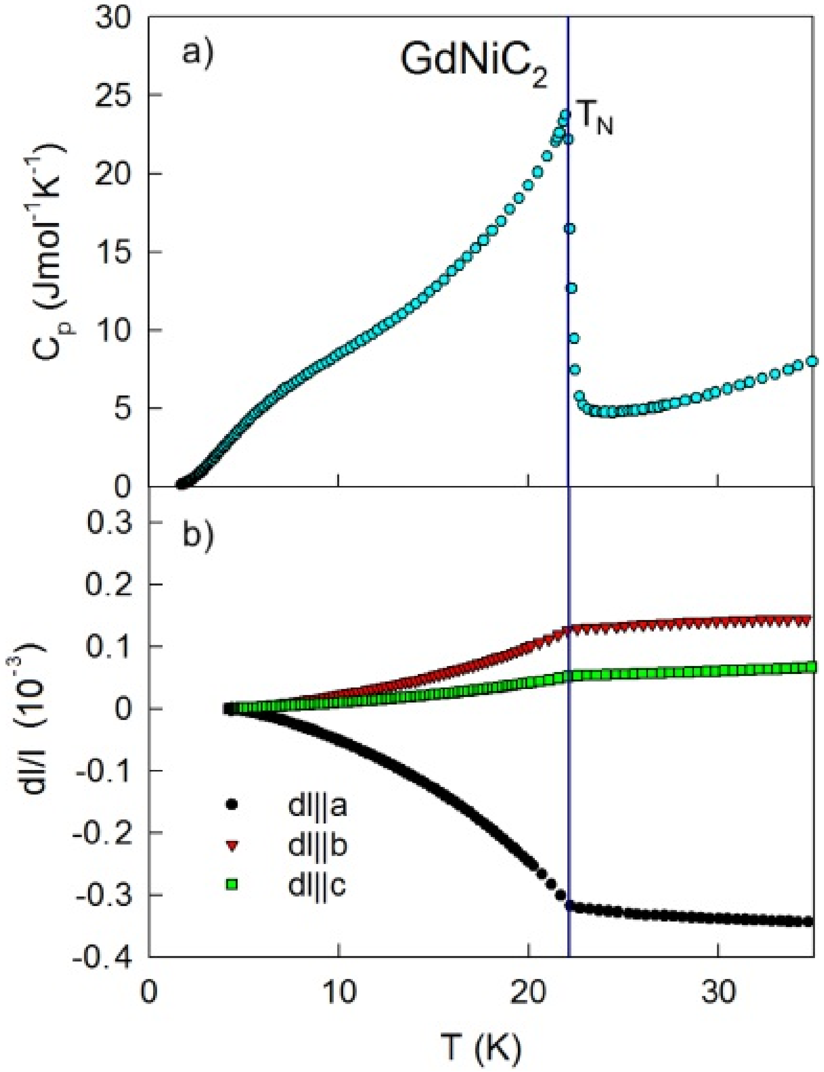

Figure 47: a) Temperature dependent specific heat and b) relative length change of $GdNiC_2$ around the Néel temperature.

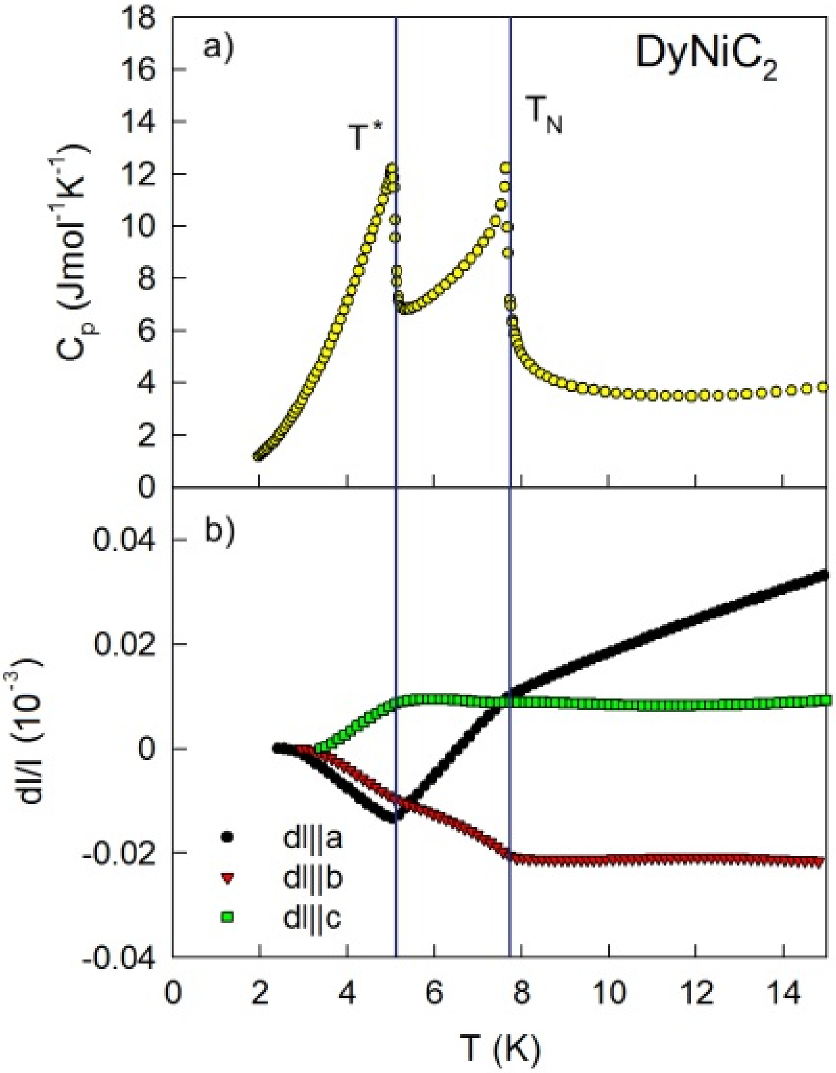

Figure 48: a) Temperature dependent specific heat [94] and b) relative length change of DyNiC$_2$ around the Néel temperature.

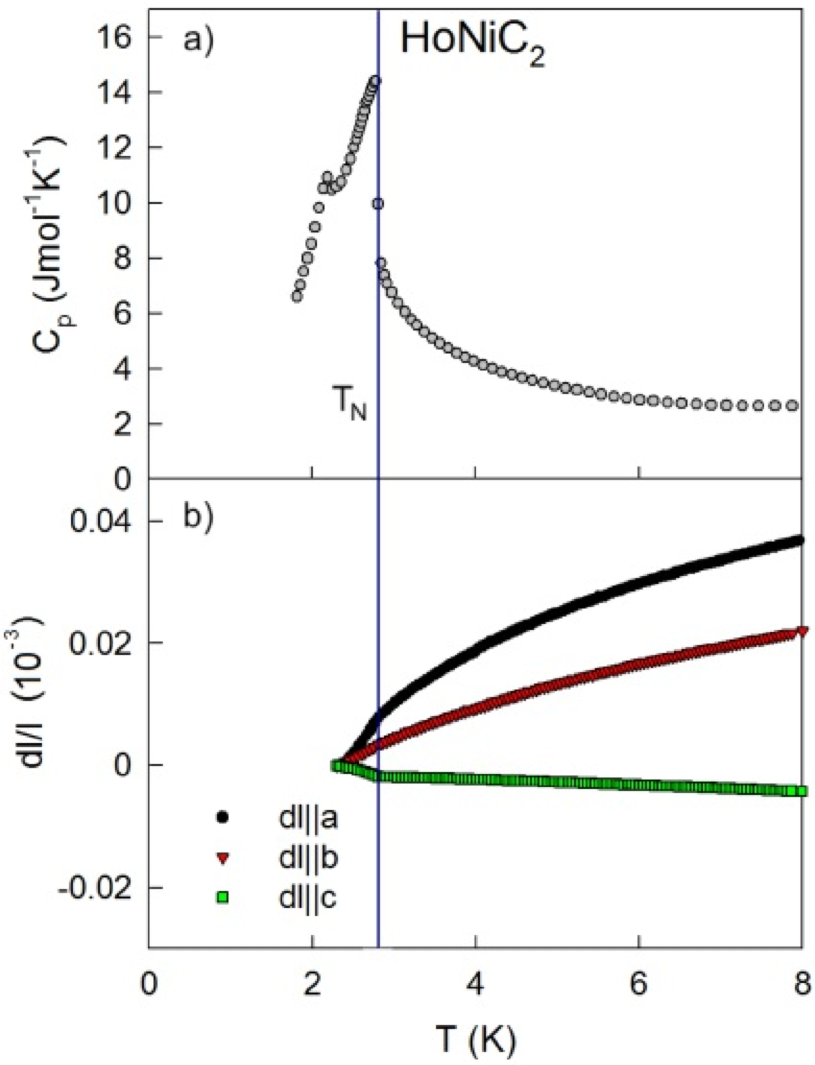

Figure 49: a) Temperature dependent specific heat and b) relative length change of $HoNiC_2$ around the Néel temperature.

Summary and Discussion

The focus of this chapter was set on the thermal expansion measurements of single crystalline cubes. During this thesis, the thermoelastic properties of $PrNiC_2$, $GdNiC_2$, $DyNiC_2$, $HoNiC_2$ and $LuNi_{0.92}Co_{0.08}C_2$ were investigated. Along with thermal measurements of $NdNiC_2$, $YNiC_2$ and $LuNiC_2$ that were already conducted before and with available resistivity measurements [92], a systematic in the behavior of the CDW phase transitions is noticed. It is found that the compounds containing Pr and Nd only exhibit a second order CDW transition. On the contrary, $RNiC_2$ compounds including Y, Gd, Dy or Ho display a first order as well as a second order CDW transition. Except for $PrNiC_2$, a similar relative length change of the three dimensions of the crystals at room temperature as compared to 2 K is observed. The relative change of the lattice parameter a is largest with $\sim 3\times10^{-3}$, followed by b and c with a dl/l of around 1×10^{-3}. In $PrNiC_2$, the elongation of the a direction shows a comparable relative length change but the b-axis only enlarges minimally and dl/l of c amounts to approximately 2×10^{-3}. The deviant behavior is due to the crystalline electric field that acts on the Pr^{+3} ion. Moreover, a pattern of the modifications in lengths of the crystal at the second order charge density wave transition is identified. Although no scheme of which direction is shortened or enlarged is observed, the changes of the b and c dimensions are larger than the change of a. In $HoNiC_2$, the a-axis showed a larger change in relative length than b and c at $T_{lock\text{-}in}$. These results conform with the results of single crystal X-ray diffraction that at the orthorhombic to incommensurate CDW transition, the atoms are primary displaced along the bc-plane, while at the incommensurate CDW to commensurate CDW transition, the displacement occurs predominantly along the a-axis. A corresponding hierarchy of the gap formation is corroborated by resistivity studies as well.

The pressure dependencies of the transition temperatures at the first order and second order CDW phase transitions were estimated *via* the Clausius-Clapeyron and a modified Ehrenfest relation. In general, it is expected that the phase transition shifts to lower temperatures with an increase in pressure as the suppression of the CDW has been achieved with this approach in several systems. The present study reveals a positive pressure dependence of the lock-in transition temperature, while the pressure dependence of the second order CDW transition temperature is negative. As a consequence, hydrostatic pressure weakens the incommensurate CDW order parameter, whereas the commensurate order parameter will be stabilized. By applying strain along certain orientations of the crystal, the transition temperatures can be tuned to higher or lower temperatures for both phases. The discovered behavior could explain the "anomalous pressure dependence" observed in $LaNiC_2$ [99]. Roman *et al.* [8] reported about the correlation between the unit cell volume of rare-earth nickel dicarbides and the transition temperatures, *c.f.* Fig. 50. In heavy rare-earths, the commensurate CDW phase is more stable, whereas in light rare-earths with larger unit cell volume the incommensurate CDW phase is favored. The present findings predict that the commensurate CDW phase transition can not only be favored by the lanthanide contraction, thus the decreasing distance between the Ni atoms with increasing atomic number of the rare-earth element, but also the temperature depending shrinking of the unit cell contributes to the stabilization of the commensurate phase.

In addition, a scheme in the pressure dependence of the critical temperature at the second order phase transition is observed. Whereas the specific heat jump augments with

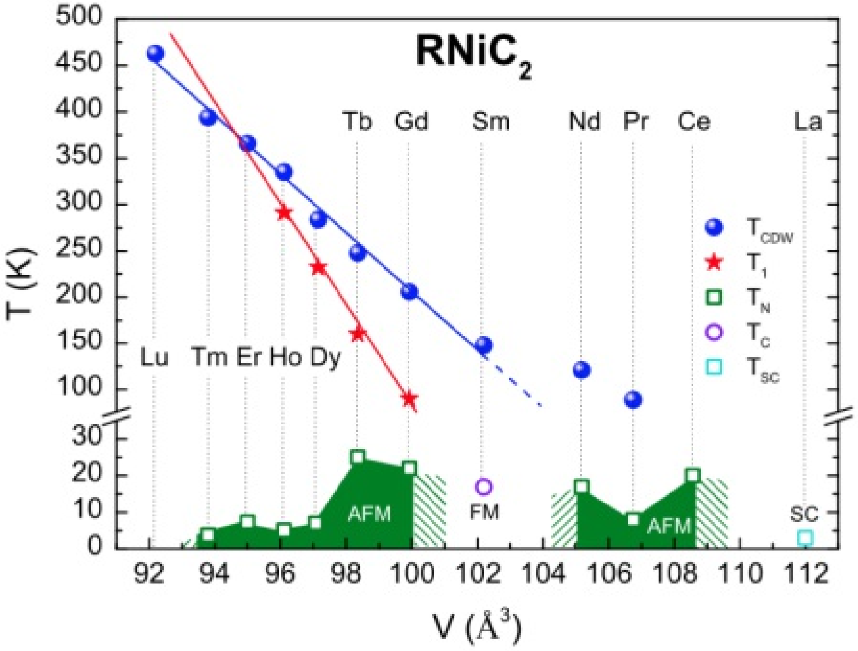

Figure 50: The second order CDW (T_{CDW}) and the lock-in transition (T_1) temperatures are depicted as a function of unit cell volume of RNiC$_2$. Adapted from Ref. [8].

higher T_{CDW}, the changes of the anisotropic thermal expansion coefficients display an equivalent magnitude independently of the critical temperature. Therefore, the pressure dependence of T_{CDW} is stronger the smaller T_{CDW}. The same effect is ascertained when analyzing the isotropic pressure dependence $\partial T_{\mathrm{CDW}}/\partial\sigma$.

The thermal expansion at the magnetic ordering transitions revealed that the strength of the exchange energy has a significant effect on the structural changes of the lattice. The most pronounced anomaly among currently studied compounds is observed in GdNiC$_2$, in which the exchange interaction is strongest and the Néel temperature is highest, followed by DyNiC$_2$ and HoNiC$_2$. Whereas the structural changes in GdNiC$_2$ at T_N are larger than at the first order lock-in transition, in DyNiC$_2$ and HoNiC$_2$ the change in length at the magnetic transition is much smaller than at $T_{lock\text{-}in}$. Due to the connection of the exchange energy and the Néel temperature, the present results conform to the expected behavior according to a scaling of these of these quantities with the de Gennes factor.

7 Summary and Outlook

In the course of the present master thesis, some earlier data was confirmed but also intriguing new characteristics could be discovered. The first achievement of this thesis was the growth of several crystals *via* the floating zone technique. These include single crystals of $GdNiC_2$ and $HoNiC_2$, as well as multidomain crystals of pseudo-ternary solid solutions of $LuNi_{0.8}Co_{0.2}C_2$ and $LuNi_{0.86}Co_{0.14}C_2$. Also, some of the measurements that are presented in this thesis were conducted with already available single crystals.

With respect to the search for a quantum critical point and the emergency of superconductivity in the solid solution of $LuNi_{1\text{-}x}Co_xC_2$, heat capacity, magnetic and resistivity measurements were performed on compounds with a Co concentration at the Ni site of 8 %, 14 % and 20 %. On the basis of these studies, the critical point that is associated with the suppression of the CDW in $LuNi_{1\text{-}x}Co_xC_2$ solid solutions is suggested to be in the range of 15 % to 20 % Co at the Ni site.

Motivated by the observation of spin glass behavior in some Pr compounds, which was attributed to a dynamic frustration, extensive studies on $PrNiC_2$ were performed. In combining heat capacity and magnetic measurements it was demonstrated that in $PrNiC_2$ no spin glass phase exists for temperatures above 0.4 K. In order to characterize the paramagnetic ground state of $PrNiC_2$ in closer detail, simultaneous fits of the experimental magnetic susceptibility and thermodynamic data were performed and an estimate of the crystal field parameters and the energy level splitting in the 4f orbital due to crystal field effects has been obtained.

In order to study the nature of structural and magnetic phase transitions, the thermal expansion of a variety of single crystalline $RNiC_2$ cubes was measured with dilatometry. It was revealed that compounds with light rare-earth elements like Pr and Nd exhibit a single second order CDW transition, while compounds containing Y, Gd, Dy or Ho feature a Peierls transition and a second lock-in transition. At the orthorhombic to incommensurate CDW phase transition, the change in length of b and c is largest, whereas at the incommensurate to commensurate CDW transition, it is most distinct for a and thus, corresponding gap formation for the electronic transport along the a-axis is suggested, which is supported by currently available resistivity data. The influence of the crystal field is clearly visible in the thermal expansion of $PrNiC_2$, as well as spontaneous magnetoelastic effects in $GdNiC_2$ due to exchange-striction. The pressure dependence of the transition temperatures of the first and second order CDW were estimated with the Clausius-Clapeyron and a modified Ehrenfest relation. While $\partial T_{CDW}/\partial p$ is predominantly negative, $dT_{lock-in}/dp$ is positive. This finding may explain why the commensurate CDW phase is stabilized by the lanthanide contraction against the incommensurate CDW phase. The application of strain along a particular crystal orientation is expected to allow shifting the CDW transitions to both, lower or higher temperatures.

The present results of research open the door to a number of new and promising proposals for future studies. These include the further examination of the CDW critical point in $LuNi_{1\text{-}x}Co_xC_2$ solid solutions. A successful growth of pseudo-ternary single crystals could be beneficial in order to trace the critical point and perhaps find a superconducting phase connected to it. Arising from the astonishing pressure dependencies of the CDW transition temperatures, it would be interesting to examine even more materials in this sense and furthermore, to try if *e.g.* in $PrNiC_2$ an incommensurate CDW to commensurate CDW transition can be induced by applying pressure. A variety of fascinating properties in this field of study are yet to be discovered.

Acknowledgements

I am grateful to all those I have had the pleasure to work with and meet during my time at the Institute of Solid State Physics at the Vienna University of Technology.

Most importantly, I extend my special thanks to Herwig Michor for enabling and supervising this master thesis. Thank you for the daily dedication and the support during all of this work. He always had an open ear for questions and patiently provided advice and assistance.

Also, I would like to thank Herbert Müller for his help in operating the thermal expansion measurements.

I would like to acknowledge Snezana Stojanovic for her introduction to metallography and X-ray diffraction.

Furthermore, I have to thank Martin Rotter for holding the *McPhase* online workshop and assisting with advice when technical difficulties during the installation of the program occurred.

Appendix

A Sample Dimensions and Measurements

A.1 Resistivity

The measurements were conducted with a Physical Property Measurement System by *Quantum Design*. Prior to the measurement, the height, width and distance between V_+ and V_- of all measured samples were determined. The electrical resistivities of the first polycrystalline $LuNi_{0.8}Co_{0.2}C_2$, the second $LuNi_{0.8}Co_{0.2}C_2$ and of the polycrystalline $LuNi_{0.86}Co_{0.14}C_2$ bar were examined. In Table 8, the dimensions of the samples are listed.

Table 8: Resistivity samples and their corresponding dimensions.

Sample	Height in mm	Width in mm	Distance V_+ - V_- in mm
$LuNi_{0.8}Co_{0.2}C_2$ No. 1	0.810	1.290	2.533
$LuNi_{0.8}Co_{0.2}C_2$ No. 2	0.660	1.500	1.292
$LuNi_{0.86}Co_{0.14}C_2$	0.650	1.140	1.320

Supplementary Graphics

In the illustration in Fig. 51, the necessary spot welding contacts on the sample are shown with the aid of a computer generated image.

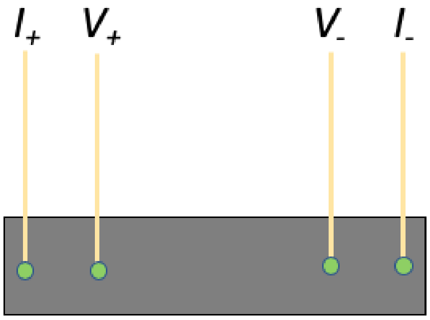

Figure 51: Schematic of the sample with four gold wire contacts affixed with spot welding.

A.2 Heat Capacity

The heat capacities were either measured with the heat capacity option of a *Quantum Design* PPMS or with an adiabatic calorimeter. During this master thesis, one monocrystalline sample of $LuNi_{0.92}Co_{0.08}C_2$ and one sample of polycrystalline $LuNi_{0.86}Co_{0.14}C_2$, as well as the second crystal of $LuNi_{0.8}Co_{0.2}C_2$, were measured with the PPMS. Furthermore, the heat capacity of a $GdNiC_2$ sample was analyzed with the PPMS, as well as with the adiabatic calorimeter due to its higher accuracy in the low temperature range. A list of the measured samples is given in Table 9.

Table 9: Samples undertaken heat capacity measurements.

Sample	Mass in mg
$LuNi_{0.92}Co_{0.08}C_2$	43.895
$LuNi_{0.86}Co_{0.14}C_2$	30.058
$LuNi_{0.8}Co_{0.2}C_2$ No. 2	52.193
$GdNiC_2$	-

A.3 Thermal Expansion

The thermal expansion was measured with a custom-made miniature capacitance dilatometer. In the course of this work, the thermal expansions of five crystals were measured, including two of $HoNiC_2$, $LuNi_{0.92}Co_{0.08}C_2$, $PrNiC_2$ and $DyNiC_2$. Unfortunately, the first $HoNiC_2$ crystal broke before mounting. Therefore, the change in length could only be determined for one crystalline direction as solely two parallel planes remained. Except from this cube, the thermal expansions of all three crystallographic axes were determined. The dimensions of the cubes including the conducted measurements are summarized in Table 10.

Table 10: Thermal expansion samples, their corresponding dimensions and the conducted measurements.

Sample	a in mm	b in mm	c in mm	THE Measurements
$HoNiC_2$ No. 1	-	1.810	-	dl || b
$HoNiC_2$ No. 2	1.925	1.335	2.170	dl || a, dl || b, dl || c
$LuNi_{0.92}Co_{0.08}C_2$	1.550	1.860	1.870	dl || a, dl || b, dl || c
$PrNiC_2$	2.335	2.230	1.625	dl || a, dl || b, dl || c
$DyNiC_2$	2.548	2.121	2.172	dl || a, dl || b, dl || c
$GdNiC_2$	2.195	1.200	2.020	dl || a, dl || b, dl || c

A.4 Magnetic Measurements

For the analysis of the magnetic properties of the rare-earth nickel dicarbide samples, the Vibrating Sample Magnetometer option of the PPMS, a SQUID, as well as a modified AC susceptometer were used.

With the VSM, the magnetization curves of a single crystal $PrNiC_2$ cube were studied. Three measurements were performed with an external magnetic field being parallel to each of the crystalline axes one after another. The cube was weighted and the corresponding value is listed in Table 11. The frequency of the vibration was adjusted to 40 Hz and the oscillation amplitude was regulated to 2 mm.

Table 11: Mass of the sample measured with the VSM option of the PPMS and orientation of the sample in the external magnetic field.

Sample	Mass in mg	VSM Measurements
$PrNiC_2$	54.140	H || a, H || b, H || c

In Fig. 52, the crystal cube inside the brass holder with the quartz cylinders and the round pieces of paper are shown.

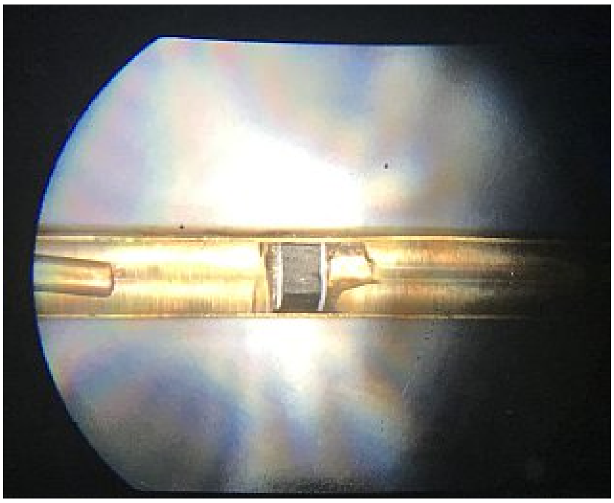

Figure 52: Sample in the VSM sample holder.

The magnetic properties of the $PrNiC_2$ cube were examined once more in the SQUID with the magnetic field being parallel to each of the three crystallographic directions. The cube was weighed again before measurement, because small pieces have splintered off since the measurements in the VSM. In addition, the magnetization of a polycrystalline piece of $LuNi_{0.8}Co_{0.2}C_2$ was studied. The masses are listed in Table 12.

Table 12: Summary of the conducted measurements with the SQUID.

Sample	Mass in mg	SQUID Measurements
$PrNiC_2$	54.073	H || a, H || b, H || c
$LuNi_{0.8}Co_{0.2}C_2$	50.020	Polycrystalline Sample

In Fig. 53, the custom-made sample holder with a sample glued to it is depicted.

Figure 53: SQUID sample holder with sample.

In the AC susceptometer, all measured samples were examined using a 400 $\frac{A}{m}$ magnetic field and frequencies of 11 Hz, 22 Hz, 40 Hz, 90 Hz, 222 Hz, 400 Hz and 889 Hz. Before mounting the sample, the exact mass was evaluated. The $PrNiC_2$ single crystalline cube was measured in all three possible orientations. The corresponding mass of the cube is listed in Table 13.

Table 13: Mass of the $PrNiC_2$ AC susceptibility cube and conducted measurements.

Sample	Mass in mg	AC Susceptibility Measurements
$PrNiC_2$	54.073	H || a, H || b, H || c

B Growth Protocol of $LuNi_{0.8}Co_{0.2}C_2$ Crystal No. 1

Elapsed Time	**Occurrences and Changed Parameters**
0min	Power: 50%; only upper rod rotating
18min	Power: 55%
30min	Power: 60%
45min	Power: 62%
59min	Power: 63%
1h12min	Rods begin to melt at 63% of power; Power: 63.4%
1h28min	Movement of upper shaft: 2.1 mm/h down; lower shaft: 4.1 mm/h down
1h35min	Power: 63.5%
1h48min	Power: 63.6%; movement of upper shaft: 2.8 mm/h; lower shaft: 5.1 mm/h
2h18min	Power: 63.7%
2h49min	Movement of upper shaft: 2.1 mm/h; lower shaft: 4.1 mm/h
2h53min	Movement of upper shaft: 2.5 mm/h
3h10min	Movement of lower shaft: 5.1 mm/h
3h34min	Movement of upper shaft: 2.0 mm/h; lower shaft: 5.5 mm/h
3h40min	Power: 63.6%
3h50min	Movement of upper shaft: 2.5 mm/h
3h58min	Movement of shafts stopped; Power: 63.7%
4h	Power: 63.8%
4h01min	Power: 63.9%
4h11min	Movement of upper shaft: 3.0 mm/h; lower shaft: 5.0 mm/h
4h20min	Power: 63.8%
4h27min	Movement of upper shaft: 4.0 mm/h
4h33min	Movement of upper shaft: 5.0 mm/h
5h08min	Movement of upper shaft: 4.0 mm/h
5h35min	Power: 63.9%
5h41min	Movement of upper shaft: 3.7 mm/h
5h58min	Movement of upper shaft: 3.5 mm/h; Power: 64%
6h01min	Movement of upper shaft: 3.2 mm/h; Power: 64.1%
6h03min	Movement of shafts stopped
6h13min	Movement of upper shaft: 2.2 mm/h; lower shaft: 5.0 mm/h
6h24min	Movement of shafts stopped; Power: 64.2%
6h30min	Movement of upper shaft: 2.2 mm/h; lower shaft: 5.0 mm/h
6h36min	Movement of upper shaft: 2.0 mm/h; lower shaft: 6.0 mm/h
6h42min	Power: 64.3%
6h44min	Power: 64.5%
6h45min	Power: 64.6%
6h49min	Movement of upper shaft: 1.0 mm/h
6h59min	Movement of lower shaft: 8.0 mm/h
7h21min	Movement of lower shaft: 12.0 mm/h
7h28min	Growth was finished

C Growth Protocol of $LuNi_{0.8}Co_{0.2}C_2$ Crystal No. 2

Elapsed Time	**Occurrences and Changed Parameters**
0min	Power: 52%; both rods rotating
18min	Power: 55%
24min	Power: 60%
37min	Power: 60.2%
40min	Power: 60.4%
51min	Power: 60.5%
57min	Power: 60.6%
59min	Movement of upper shaft: 2.1 mm/h down; lower shaft: 0.1 mm/h down
1h	Rotation of upper shaft stopped; Movement of lower shaft: 5.1 mm/h
1h03min	Rods begin to melt at 60.6% of power
1h08min	Movement of lower shaft: 4.1 mm/h
1h12min	Power: 60.7%
1h16min	Rotation of upper shaft started and lower shaft stopped
1h45min	Movement of upper shaft: 2.1 mm/h; lower shaft: 3.1 mm/h
1h53min	Power: 60.8%
2h33min	Power: 60.7%
2h52min	Power: 60.6%
3h05min	Power: 60.5%
3h14min	Power: 60.4%
3h28min	Movement of upper shaft: 1.8 mm/h; lower shaft: 3.0 mm/h; Power: 60.3%
3h31min	Movement of upper shaft stopped
3h37min	Power: 60.3%
3h46min	Power: 60.2%
4h	Slow down upper shaft rotation from 5.0 rpm to 4.4 rpm
4h06min	Movement of both shafts stopped
4h14min	Power: 60.3%
4h35min	Movement of upper shaft: 2.2 mm/h; lower shaft: 3.0 mm/h
5h37min	Power: 60.4%
6h07min	Power: 60.5%
6h19min	Movement of upper shaft stopped; Power: 60.6%
6h26min	Power: 60.7%
6h28min	Movement of upper shaft: 2.0 mm/h; lower shaft: 3.0 mm/h
6h31min	Power: 60.8%
6h38min	Power: 60.9%
6h44min	Power: 61.0%
6h50min	Movement of upper shaft stopped; Power: 61.1%
6h54min	Power: 61.2%
6h58min	Movement of upper shaft: 2.0 mm/h
6h59min	Power: 61.3%
7h20min	Movement of lower shaft: 3.5 mm/h
7h39min	Movement of lower shaft: 5.0 mm/h
7h40min	Power: 61.2%
7h44min	Movement of lower shaft: 5.5 mm/h

Elapsed Time	**Occurrences and Changed Parameters**
7h50min	Movement of upper shaft stopped; lower shaft: 6.0 mm/h
8h13min	Movement of lower shaft: 8.0 mm/h
8h19min	Movement of lower shaft: 10.0 mm/h
8h31min	Growth was finished

D Growth Protocol of $LuNi_{0.86}Co_{0.14}C_2$

Elapsed Time	**Occurrences and Changed Parameters**
0min	Power: 52%; only upper rod rotating
18min	Power: 55%
24min	Power: 60%
50min	Power: 61%
57min	Rods begin to melt at 60.5% of power
1h03min	Power: 62%
1h12min	Power: 61.5%, Movement of lower shaft: 2.1 mm/h down
1h18min	Power: 62%
1h25min	Movement upper shaft: 2.1 mm/h down; lower shaft: 4.1 mm/h
1h53min	Movement lower shaft: 3.1 mm/h
2h37min	Movement upper shaft: 2.5 mm/h; lower shaft: 3.5 mm/h
3h33min	Movement lower shaft: 3.2 mm/h
4h03min	Power: 62.1%
4h29min	Movement lower shaft: 4.2 mm/h; Power: 62.2%
6h37min	Movement lower shaft: 4.8 mm/h
6h46min	Movement lower shaft: 5.8 mm/h
6h59min	Power: 62.3%
7h04min	Problem during Growth; Power: 63.2%
7h08min	Movement upper shaft: 2.0 mm/h; lower shaft: 7.0 mm/h; Power: 63.4%
7h10min	Power: 63.5%
7h15min	Power: 63.4%
7h41min	Movement upper shaft: 1.0 mm/h; lower shaft: 11.0 mm/h
7h48min	Movement upper shaft stopped; lower shaft: 14.0 mm/h
7h53min	Growth was finished

E Growth Protocol of $HoNiC_2$ Crystal No. 2

Elapsed Time	**Occurrences and Changed Parameters**
0min	Power: 49%; upper rod rotating
18min	Power: 53%
30min	Power: 57%
34min	Rods begin to melt at 54.8% of power
39min	Power: 57.1%
45min	Power: 57.2%
50min	Power: 57.3%
51min	Movement of lower shaft: 2.1 mm/h down
58min	Power: 57.4%
59min	Movement of upper shaft: 2.1 mm/h down; lower shaft: 4.0 mm/h
2h01min	Movement of upper shaft: 2.5 mm/h
2h20min	Power: 57.3%
3h18min	Movement of upper shaft: 3.2 mm/h
3h24min	Movement of shafts stopped
3h34min	Power: 57.2%; Movement of upper shaft: 2.0 mm/h; lower shaft: 3.0 mm/h
3h53min	Movement of upper shaft: 2.5 mm/h; lower shaft: 3.6 mm/h
4h41min	Movement of upper shaft: 2.2 mm/h
5h02min	Movement of upper shaft: 2.0 mm/h; lower shaft: 3.8 mm/h
5h46min	Movement of lower shaft: 4.0 mm/h
5h56min	Movement of lower shaft: 4.2 mm/h
6h06min	Movement of lower shaft: 4.4 mm/h
6h15min	Movement of lower shaft: 4.7 mm/h
6h25min	Movement of lower shaft: 5.0 mm/h
6h36min	Movement of lower shaft: 5.5 mm/h
6h54min	Movement of lower shaft: 6.0 mm/h
7h05min	Movement of upper shaft: 1.0 mm/h; lower shaft: 8.0 mm/h
7h15min	Power: 57.4%
7h30min	Growth was finished

F Growth Protocol of $GdNiC_2$

Elapsed Time	**Occurrences and Changed Parameters**
0min	Power: 48%; upper rod rotating
18min	Power: 51%
24min	Ramp Power to 54%
31min	Rods begin to melt at 53% of power
37min	Power: 54.1%
41min	Movement of lower shaft: 2.1 mm/h down
43min	Power: 54.2%
54min	Movement of of upper shaft: 2.1 mm/h down; lower shaft: 4.0 mm/h
1h49min	Movement of upper shaft: 2.5 mm/h
2h27min	Power: 54.1%
2h53min	Movement of lower shaft: 3.8 mm/h
3h30min	Power: 54.2%; Movement of lower shaft: 3.4 mm/h
3h41min	Power: 54.1%; Movement of upper shaft: 2.3 mm/h
4h05min	Movement of lower shaft: 3.3 mm/h
4h49min	Movement of lower shaft: 3.1 mm/h
6h07min	Movement of upper shaft: 2.0 mm/h; lower shaft: 3.6 mm/h
6h17min	Movement of lower shaft: 4.0 mm/h
6h27min	Movement of lower shaft: 4.4 mm/h
6h37min	Movement of lower shaft: 4.8 mm/h
6h47min	Movement of lower shaft: 5.3 mm/h
6h57min	Movement of lower shaft: 5.8 mm/h
7h07min	Movement of lower shaft: 6.3 mm/h
7h25min	Movement of upper shaft: 1.8 mm/h
7h48min	Movement of upper shaft: 1.4 mm/h; lower shaft: 7.0 mm/h
8h06min	Movement of upper shaft: 1.0 mm/h; lower shaft: 9.0 mm/h
8h20min	Growth was finished

G Blank Signal and Temperature Correction

On the following page, it is shown how the AC susceptibility is calculated in an *Excel* sheet from the obtained data file and subsequently, the temperature is corrected, as described in section 3.3. For this purpose, an extract of the in-phase data of the AC susceptibility measurement of $PrNiC_2$ with the magnetic field applied along the crystallographic a-axis and a frequency of 889 Hz is used.

Some additional remarks:

- A, B, C, D, E and F mark columns
- The rows are labelled with numbers, *e.g.* 1, 2, ...
- The parameters a, b, c and d can be looked up in section 3.3.
- The calculations in the boxes below the table only typify the formulas for the first row filled with numbers and have to be inserted into the corresponding cell.
- The values of row 3 and higher can be computed by marking the 2^{nd} cell and pulling the lower right corner of it down.

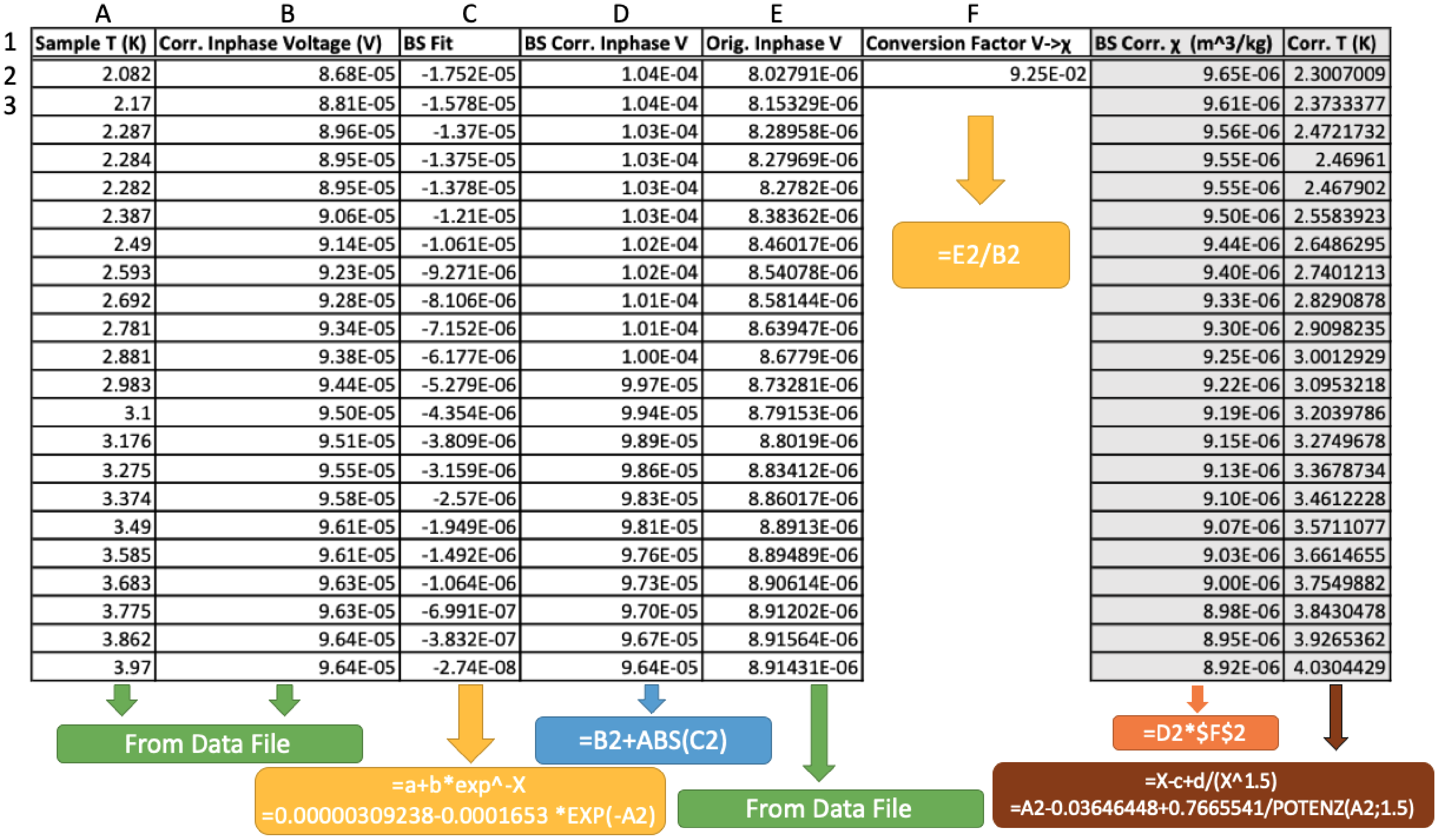

	A	B	C	D	E	F		
1	Sample T (K)	Corr. Inphase Voltage (V)	BS Fit	BS Corr. Inphase V	Orig. Inphase V	Conversion Factor V->χ	BS Corr. χ (m^3/kg)	Corr. T (K)
2	2.082	8.68E-05	-1.752E-05	1.04E-04	8.02791E-06	9.25E-02	9.65E-06	2.3007009
3	2.17	8.81E-05	-1.578E-05	1.04E-04	8.15329E-06		9.61E-06	2.3733377
	2.287	8.96E-05	-1.37E-05	1.03E-04	8.28958E-06		9.56E-06	2.4721732
	2.284	8.95E-05	-1.375E-05	1.03E-04	8.27969E-06		9.55E-06	2.46961
	2.282	8.95E-05	-1.378E-05	1.03E-04	8.2782E-06		9.55E-06	2.467902
	2.387	9.06E-05	-1.21E-05	1.03E-04	8.38362E-06		9.50E-06	2.5583923
	2.49	9.14E-05	-1.061E-05	1.02E-04	8.46017E-06		9.44E-06	2.6486295
	2.593	9.23E-05	-9.271E-06	1.02E-04	8.54078E-06		9.40E-06	2.7401213
	2.692	9.28E-05	-8.106E-06	1.01E-04	8.58144E-06		9.33E-06	2.8290878
	2.781	9.34E-05	-7.152E-06	1.01E-04	8.63947E-06		9.30E-06	2.9098235
	2.881	9.38E-05	-6.177E-06	1.00E-04	8.6779E-06		9.25E-06	3.0012929
	2.983	9.44E-05	-5.279E-06	9.97E-05	8.73281E-06		9.22E-06	3.0953218
	3.1	9.50E-05	-4.354E-06	9.94E-05	8.79153E-06		9.19E-06	3.2039786
	3.176	9.51E-05	-3.809E-06	9.89E-05	8.8019E-06		9.15E-06	3.2749678
	3.275	9.55E-05	-3.159E-06	9.86E-05	8.83412E-06		9.13E-06	3.3678734
	3.374	9.58E-05	-2.57E-06	9.83E-05	8.86017E-06		9.10E-06	3.4612228
	3.49	9.61E-05	-1.949E-06	9.81E-05	8.8913E-06		9.07E-06	3.5711077
	3.585	9.61E-05	-1.492E-06	9.76E-05	8.89489E-06		9.03E-06	3.6614655
	3.683	9.63E-05	-1.064E-06	9.73E-05	8.90614E-06		9.00E-06	3.7549882
	3.775	9.63E-05	-6.991E-07	9.70E-05	8.91202E-06		8.98E-06	3.8430478
	3.862	9.64E-05	-3.832E-07	9.67E-05	8.91564E-06		8.95E-06	3.9265362
	3.97	9.64E-05	-2.74E-08	9.64E-05	8.91431E-06		8.92E-06	4.0304429

=E2/B2

From Data File

=a+b*exp^-X
=0.00000309238-0.0001653 *EXP(-A2)

=B2+ABS(C2)

From Data File

=D2*F2

=X-c+d/(X^1.5)
=A2-0.03646448+0.7665541/POTENZ(A2;1.5)

H Original AC Susceptibility Data of $PrNiC_2$

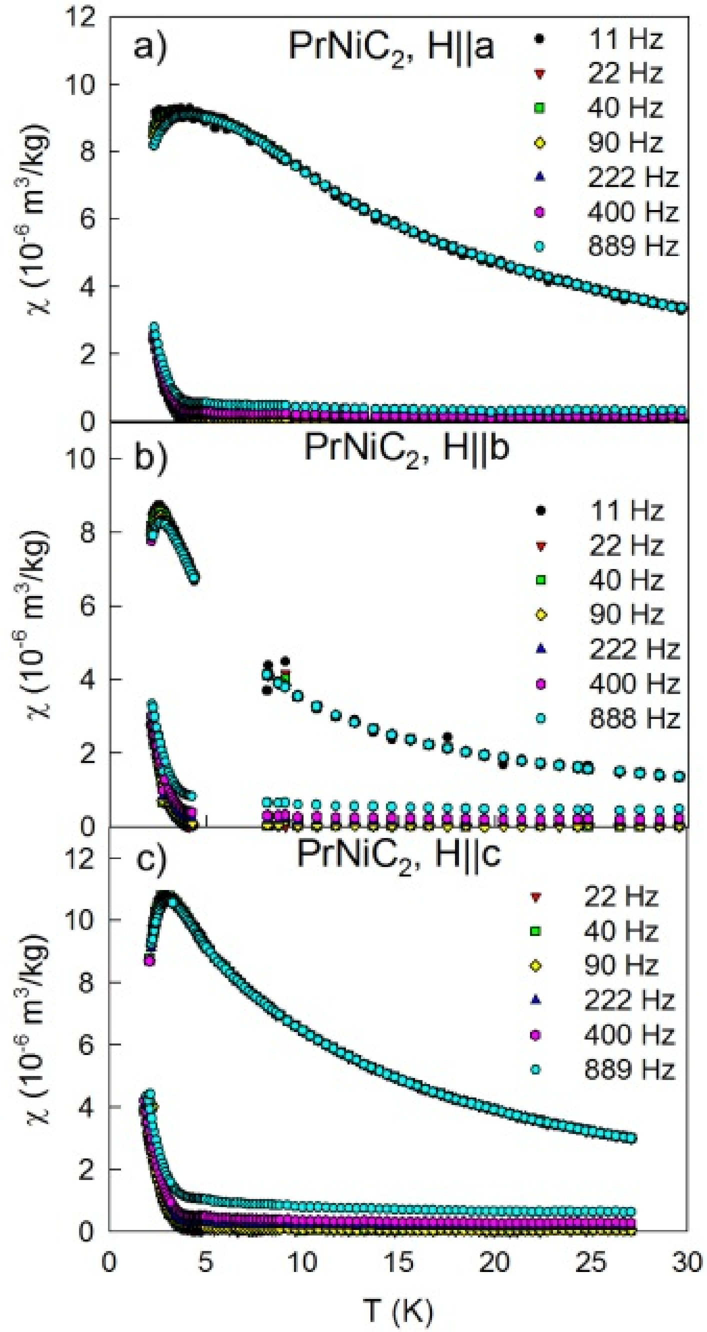

Figure 54: Uncorrected AC susceptibility data of $PrNiC_2$. a) $H||a$. b) $H||$. c) $H||c$.

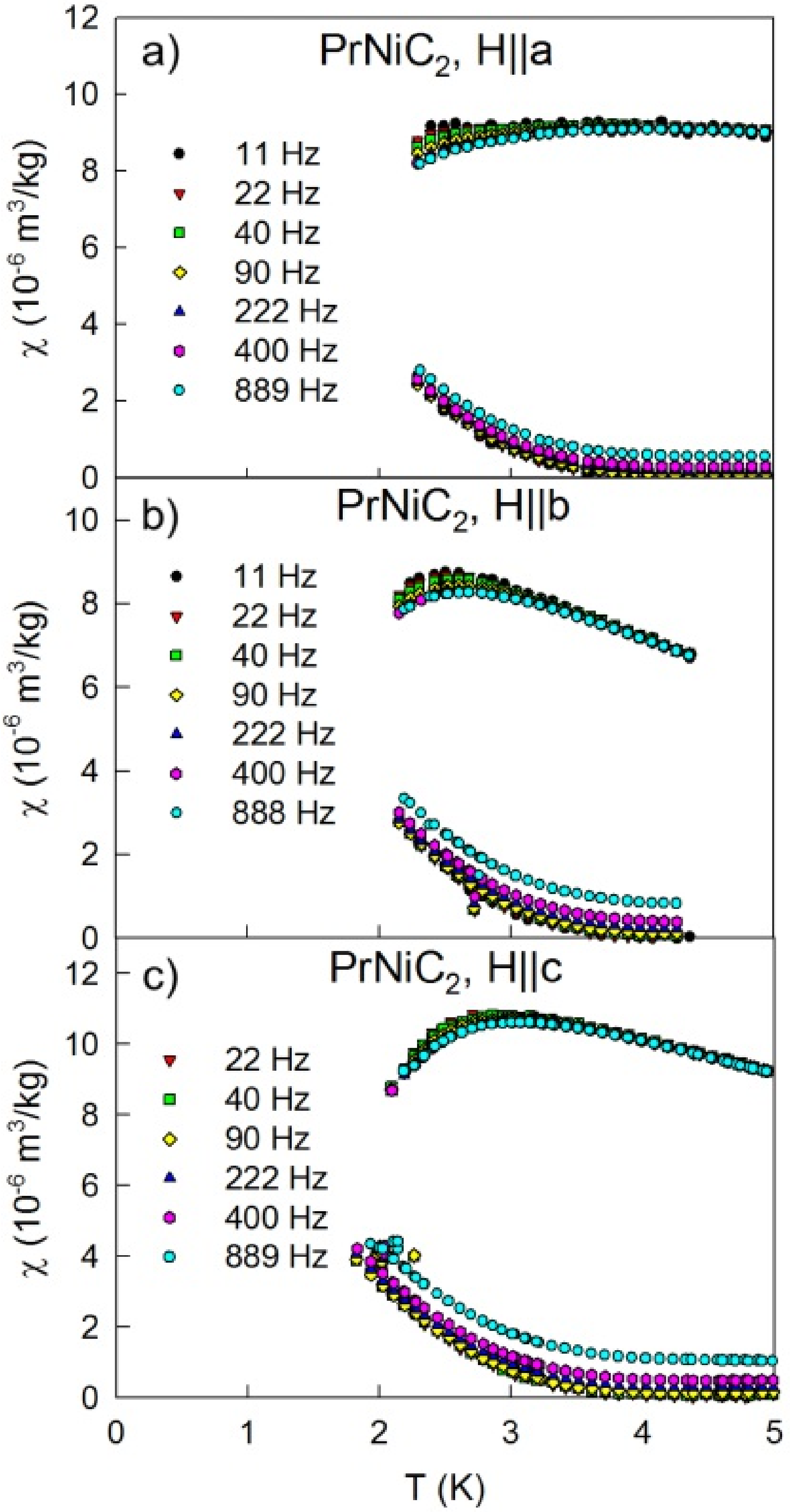

Figure 55: Close-up of the uncorrected AC susceptibility data of $PrNiC_2$. a) $H||a$. b) $H||$. c) $H||c$.

I THE Comparison of $HoNiC_2$ crystal No.1 & No. 2

As mentioned earlier, the thermal expansion of $HoNiC_2$ had to be conducted twice because the first crystal broke during mounting and only the modification of the b-axis of the first crystal could be examined. For comparison, the thermal expansion of the b-axis of both crystals is presented in Fig. 56. Only small deviations that get larger at temperatures above 200 K are visible but overall, the data appears to be meaningful and can be reproduced. The minor discrepancies of this quantity of the two crystals can be a result of various factors. The crystal which was measured first had a longer b of 1.810 mm, compared to the secondly examined crystal with $b = 1.335$ mm. The longer the side length, the more precise the measurement will be. Another reason that influences the outcome can be the accuracy of orientation. Also, the shift of the cube during mounting is a possible source of error.

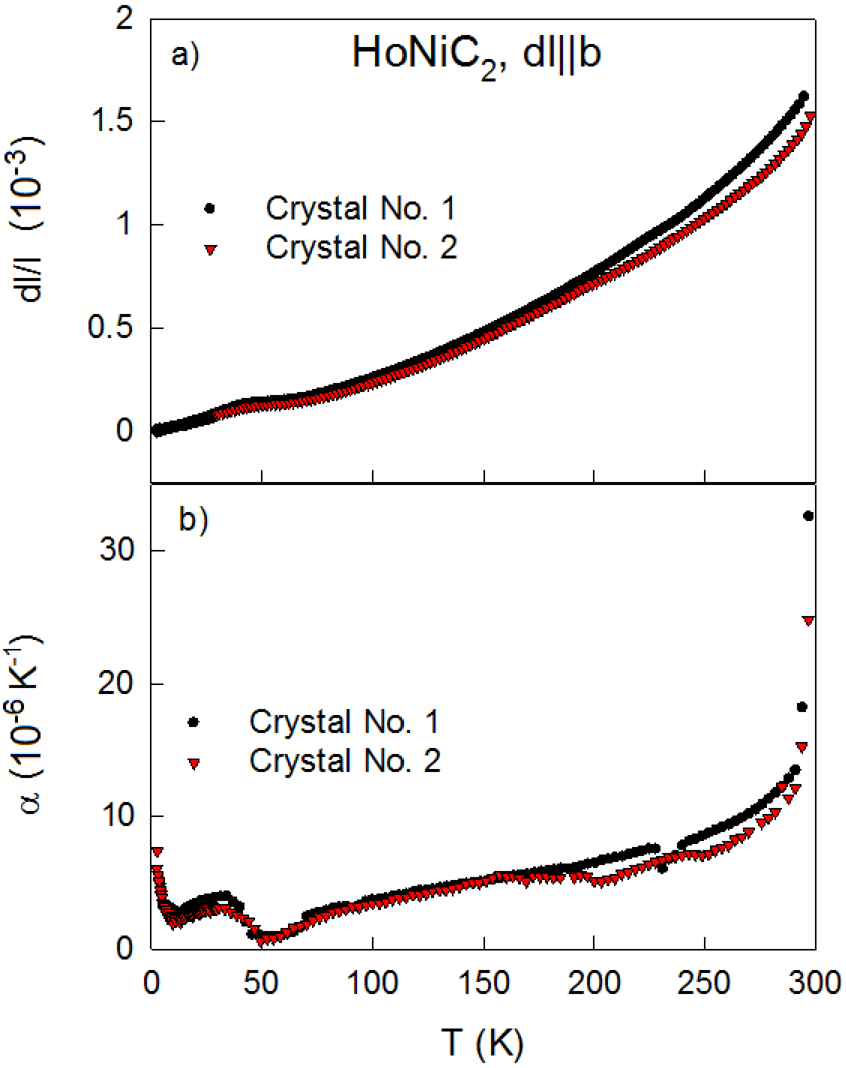

Figure 56: Comparison of a) the relative change in length and b) α of the b-axis of the first and second crystal of $HoNiC_2$.

References

[1] E. Canadell. Dimensionality and Fermi Surface of Low-Dimensional Metals. *Chem. Mater.*, 10(2770-2786), 1998.

[2] J. Laverock, T.D. Haynes, C. Utfeld, and S.B. Dugdale. Electronic structure of $RNiC_2$ (R=Sm, Gd, and Nd) intermetallic compounds. *Phys. Rev. B*, 80(125111), 2009.

[3] J.-C.G. Bünzli, and V.K. Pecharsky, editor. *Handbook on the Physics and Chemistry of Rare Earths*, volume 52. Elsevier, 2017.

[4] S. Steiner, H. Michor, O. Sologub, B. Hinterleitner, F. Höfenstock, M. Waas, E. Bauer, B. Stöger, V. Babizhetskyy, V. Levytskyy, and B. Kotur. Single crystal study of the charge density wave metal $LuNiC_2$. *Phys. Rev. B*, 97(205115), May 2018.

[5] J. Yakinthos, P. Kotsanidis, W. Scha fer, W. Kockelmann, G. Will, and W. Reimers. The two-component non-collinear antiferromagnetic structures of $DyNiC_2$ and $HoNiC_2$. *J. Magn. Magn. Mater.*, 136:327–334, 1994.

[6] W. Schäfer, W. Kockelmann, G. Will, J.K. Yakinthos, P.A. Kotsanidis. Magnetic structures of rare earths R in $RCoC_2$ and $RNiC_2$ compounds. *Journal of Alloys and Compounds*, 250(565-568), 1997.

[7] M. Murase, A. Tobo, H.Onodera, Y. Hirano, T. Hosaka, s. Shimomura, and N. Wakabayashi. Lattice Constants, Electrical Resistivity an Specific Heat of $RNiC_2$. *J.Phys.Soc.Jpn*, 73(10):2790–2794, 2004.

[8] M. Roman, J. Strychalska-Nowak, T. Klimczuk, and K.K. Kolincio. Extended phase diagram of $RNiC_2$ family: Linear scaling of the Peierls temperature. *Phys. Rev. B*, 97(041103), January 2018.

[9] S. Shimomura, C. Hayashi, N. Hanasaki, K. Ohnuma, Y. Kobayashim H. Nakao, M. Mizumaki, and H. Onodera. Multiple charge density wave transitions in antiferromagnets $RNiC_2$ (R=Gd,Tb). *Phys. Rev. B*, 93(165108), April 2016.

[10] W.H. Lee, H.K. Zeng, Y.D. Yao, and Y.Y. Chen. Superconductivity in the Ni based ternary carbide $LaNiC_2$. *Physica C: Superconductivity*, 266(1-2):138–142, July 1996.

[11] Y. Hirose, T. Kishino, J. Sakaguchi, Y. Miura, F. Honda, T. Takeuchi, E. Yamamoto, Y. Haga, H. Harima, R. Settai, and Y. Onuki. Fermi Surface and Superconducting Properties of Non-centrosymmetric $LaNiC_2$. *J.Phys.Soc.Jpn*, 81(113703), 2012.

[12] S. Shimomura, C. Hayashi, G. Asaka, N. Wakabayashi, M. Mizumaki, and H. Onodera. Charge-density-wave destruction and ferromagnetic order in $SmNiC_2$. *Phys. Rev. B*, 102(7), 2009.

[13] K.K. Kolincio, M. Roman, and T. Klimczuk. Charge density wave and large nonsaturating magnetoresistance in $YNiC_2$ and $LuNiC_2$. *Phys. Rev. B*, 99(205127), May 2019.

[14] R.E. Thorne. Charge-Density-Wave Conductors. *Physics Today*, 49(5):42, May 1996.

[15] K.K. Kolincio, M. Roman, M. J. Winiarski, J. Strychalska - Nowak, T. Klimczuk. Magnetism and charge density waves in $RNiC_2$ (R = Ce, Pr, Nd). *Phys. Rev. B*, 95(235156), June 2017.

[16] W. Schäfer, G. Will, J.K. Yakinthos, and P.A. Kotsanidis. Neutron diffraction study of $RNiC_2$ (R =rare earth) compounds. *Journal of Alloys and Compounds*, 180(1-2):251–257, 1992.

[17] H. Maeda, R. Kondo, and Y. Nogami. Multiple charge density waves compete in ternary rare-earth nickel carbides, $RNiC_2$ (R:Y,Dy,Ho,and Er). *Phys. Rev. B*, 100(104107), 2019.

[18] A. Krimmel, J. Hemberger, M. Nicklas, G. Knebel, W. Trinkl, M. Brando, V. Fritsch, and A. Loidl. Spin-glass behavior in $PrAu_2Si_2$. *Phys. Rev. B*, 59(10), 1998.

[19] W. Nolting. *Grundkurs Theoretische Physik 4*, volume 8. Springer-Verlag, 2012.

[20] G. Jaeger. The Ehrenfest Classification of Phase Transitions: Introduction and Evolution. *Arch. Hist. Exact Sci.*, 53(1):51–81, 1998.

[21] G. Kriza, K.-C. Ameline, D. Jérome, A. Dworkin, H. Szwarc, C. Fabre, D. Schütz, A. Rassat, P. Bernier, A. Zahab. Pressure dependence ot the structural phase transition in C_{60}. *J. Phys F* , 1:1361–1364, 1991.

[22] F. Guillou, A.K. Pathak, D. Paudyal, Y. Mudryk, F. Wilhelm, A. Rogalev, and V.K. Pecharsky. Non-hysteretic first-order phase transition with large latent heat and giant low-field magnetocaloric effect. *Nature Communications*, 9(2925), 2018.

[23] W. Wang, D. Dietzel, and A. Schirmeisen. Lattice Discontinuities of 1T-TaS_2 across First Order Charge Density Wave Phase Transitions. *Scientific Reports*, 9(7066), 2019.

[24] J. Rosaler. Generalized Ehrenfest Relations, Deformation Quantization, and the Geometry of Inter-model Reduction. *Found Phys*, 48:355–385, 2018.

[25] L.D. Landau. On the Theory of Phase Transitions. *Zh. Eksp. Teor. Fiz.*, 7:19–32, 1937.

[26] L.R. Testardi. Elastic modulus, thermal expansion, and specific heat at a phase transition. *Phys. Rev. B*, 12(9), 1975.

[27] M. Saint-Paul, and P. Monceau. Phenomenological approach of the thermodynamic properties of the charge density wave systems. *Philosophical Magazine*, 2020.

[28] M. Saint-Paul, and P. Monceau. Survey of the Thermodynamic Properties of the Charge Density Wave Systems. *Advances in Condensed Matter Physics*, 2019(4):1–14, 2019.

[29] P. Debye. Zur Theorie der spezifischen Wärme. *Ann. Phys.*, 39(4):789–839, 1912.

[30] P.A. Tipler and G. Mosca. *Physik: für Wissenschaftler und Ingenieure*. Spektrum Akademischer Verlag, 2009.

[31] R. Gross and A. Marx. *Festkörperphysik*. De Gruyter, 2nd edition, 2014.

[32] C. Kittel. *Introduction to Solid State Physics*. Wiley John & Sons, 8th edition, 2004.

[33] S. Blundell. *Magnetism In Condensed Matter*. Oxford University Press,, 2001.

[34] E. Bolthausen. *Spin Glasses*. Springer, 2007.

[35] K. Binder, and A. Young. Spin glasses: Experimental facts, theoretical concepts, and open questions. *Rev. Mod. Phys.*, 58(801), 1986.

[36] S. Shtrikman, and E.P. Wohlfarth. The Theory of the Vogel-Fulcher Law of Spin Glasses. *Phys. Lett.*, 85 A(8), 1981.

[37] E.A. Goremychkin, R. Osborn, B.D. Rainford, R.T. Macaluso, D.T. Adroja, and M. Koza. Spin-glass order induced by dynamic frustration. *Nature Physics*, 4, 2008.

[38] K.W.H. Stevens. Matrix Elements and Operator Equivalents Connected with Magnetic Properties of Rare Earth Ions‘. *Proc. Phys. Soc.*, A 65(209), 1952.

[39] M. Rotter, McPhase Project, Program Version: 5.2, Dec. 2016, www.mcphase.de.

[40] J. Jensen, and A.R. Mackintosh. *Rare Earth Magnetism: Structures and Excitations*. Clarendon Press, 1991.

[41] D.J. Newman, and B. Ng. *Crystal Field Handbook*. Cambridge University Press, 2000.

[42] R. Peierls. *Quantum Theory of Solids*. Oxford Clarendon Press, 1955.

[43] H. Fröhlich. On the theory of superconductivity: the one-dimensional case. *Proc. R. Soc. Lond. A*, 223(1154):296–305, 1954.

[44] X. Zhu, J. Guo, J. Zhang, and E.W. Plummer. Misconceptions associated with the origin of charge density waves. *Advances in Physics:X*, 2(3):622–640, 2017.

[45] X. Zhu, Y. Cao, J. Zhang, E.W. Plummer, and J. Guo. Classification of charge density waves based on their nature. *Proceedings of the National Academy of Sciences*, 112(8), 2015.

[46] Z.Z. Wang, J.C. Girard, C. Pasquier, and D. Jerome. Study of C-I-C CDW phase transition in TTF-TCNQ with STM. *Synthetic Metals*, 133-134:23–26, 2003.

[47] X. Xi, L. Zhao, Z. Wang, H. Berger, L. Forró, J. Shan, and K.F. Mak . Strongly enhanced charge-density-wave order in monolayer $NbSe_2$. *Nature Nanotechnology*, 10:765–769, 2015.

[48] S. van Smaalen, M. Shaz, L. Palatinus, P. Daniels, F. Galli, G. J. Nieuwenhuys, and J. A. Mydosh. Multiple charge-density waves in $R_5Ir_4Si_{10}$ (R = Ho, Er, Tm, and Lu. *Phys. Rev. B*, 69(014103), 2004.

[49] H. Miao, R. Fumagalli, M. Rossi, J. Lorenzana, G. Seibold, F. Yakhou-Harris, K. Kummer, N. B. Brookes, G. D. Gu, L. Braicovich, G. Ghiringhelli, and M. P. M. Dean. Formation of Incommensurate Charge Density Waves in Cuprates. *Phys. Rev. X*, 9(031042), 2019.

[50] H.K.D.H. Bhadeshia, and C.M. Wayman,. *Physical Metallurgy, 16 Phase Transformations: Nondiffusive.* Elsevier, 5th edition, 2014.

[51] A. W. Overhauser. Theory of charge-density-wave–spin-density-wave mixing. *Phys. Rev. B*, 29(7023), 1984.

[52] M. Roman. Gdansk University of Technology.

[53] V. Levytskyy. Ivan Franko National University of Lviv.

[54] S.M. Koohpayeh, D. Fort, and J.S. Abell. The optical floating zone technique: A review ofexperimental procedures with special reference to oxides. *Progress in Crystal Growth and Characterization of Materials*, 54(3-4):121–137, 2008.

[55] B. Vucelić Radović, D. Lazić, and M. Nikšić. *Application of Molecular Methods and Raman Microscopy/Spectroscopy in Agricultural Sciences and Food Technology.* London: Ubiquity Press., 2019.

[56] W. Zinth, and U. Zinth. *Optik, Lichtstrahlen - Wellen - Photonen.* Oldenbourg Wissenschaftsverlag GmbH, 2005.

[57] W. Friedrich, P. Knipping, and M. Laue. Interferenzerscheinungen bei Röntgenstrahlen. *Ann. Phys.*, 346:971–988, 1913.

[58] https://www.nobelprize.org/prizes/physics/1914/laue/facts/; last accessed August 24th 2020.

[59] https://www.nobelprize.org/prizes/physics/1915/summary/; last accessed November 4th 2020.

[60] A. Filhol, OrientExpress Program Version 3.4.

[61] G. Ventura, and L. Risegari, editor. *The Art of Cryogenics, 12 - Measurements of Heat Capacity.* Elsevier, 2008.

[62] Quantum Design. *Physical Property Measurement System; Heat Capacity Option User's Manual*, part number 1085-150, h-1 edition, 2004.

[63] L. Leber. *Magnetische und magnetokalorische Untersuchung des intermetallischen Systems* $LaCo_9Si_{(4\text{-}x)}Ge_{(x)}$. Master Thesis, TU Wien, 2012.

[64] M. Rotter, H. Müller, E. Gratz, M. Doerr, and M. Loewenhaupt. A miniature capacitance dilatometer for thermal expansion and magnetostriction. *Rev. Sci. Instr.*, 69(7):2742–2746, 1998.

[65] https://www.nobelprize.org/prizes/physics/1973/press-release/; last accessed August 8th 2021.

[66] Quantum Design. *Physical Property Measurement System; Vibrating Sample Magnetometer (VSM) Option User's Manual*, part number 1096-100, a3 edition, 2008.

[67] R. Fagaly. Superconducting quantum interference device instruments andapplications. *Rev. Sci. Instrum.*, 77(101101), 2006.

[68] R. Kleiner, D. Koelle, F. Ludwig, and J. Clarke . Superconducting quantum interference devices: State of the art and applications. *Proceedings of the IEEE*, 92(10), 2004.

[69] G. Binder. *Untersuchung von Spingläsern durch Wechselfeldsuszeptibilitätsmessungen*. Master Thesis, TU Wien, 2019.

[70] LakeShore Crytronics Inc. *LakeShore. User's Manual 7000 Series AC SUSCEPTOMETERS*, 1996.

[71] T. Gruner, D. Jang, Z. Huesges, R. Cardoso-Gil, G. H. Fecher, M. M. Koza, O. Stockert, A.P. Mackenzie, M. Brando, and C. Geibel. Charge density wave quantum critical point withstrong enhancement of superconductivity. *Nature Physics*, 13, 2017.

[72] A. Vock. *Thermal and Electronic Properties of* $LuNi_xCo_{1-x}C_2$ *Compounds*. Project Work, TU Wien, 2019.

[73] V. Levytskyy, Ivan Franko National University of Lviv (Private Communication, 2017).

[74] M. Fritthum. *Preparation and Measurements of physical properties of rare-earth transition-metal dicarbide single crystals*. Project Work, TU Wien, 2019.

[75] C. Wei, N. Antolin, O.D. Restrepo, W. Windl, J.-C. Zhao. A general model for thermal and electrical conductivity of binarymetallic systems. *Acta Materialia*, 126:272–279, 2017.

[76] P.W. Selwood. *Magnetochemistry*. Interscience Publishers Inc., 1956.

[77] H. Onodera, Y. Koshikawa, M. Kosaka, M. Ohashi, H. Yamauchi, and Y. Yamaguchi. Magnetic properties of single-crystalline $\mathrm{RNiC_2}$ compounds (R = Ce, Pr, Nd and Sm). *J. Magn. Magn. Mater.*, 182:161–171, 1998.

[78] P.A. Kotsanidis, J.K. Yakinthos, and E. Gamari-Seal. Magnetic properties of the ternary carbides of the rare earth and nickel group metals. *J. Less-Common Met.*, 152(287), 1989.

[79] N. Yamamoto, R. Kondo, H. Maeda, and Y. Nogami. Interplay of Charge-Density Wave and Magnetic Order in Ternary Rare-Earth Nickel Carbides, $\mathrm{RNiC_2}$ (R=Pr and Ni). *J.Phys.Soc.Jpn*, 83(123701), 2013.

[80] K. Trachenko. Understanding spin glass transition as a dynamic phenomenon. *J. Phys.: Condens. Matter*, 23(366003), 2011.

[81] J. Mantilla, E. Ter Haar, J. Coaquira, and V. Bindilatti. Dynamic susceptibility measurements at the spin-glass transition in the $\mathrm{Zn_{1x}Mn_xIn_2Se_4}$ semiconductor. *J. Phys.: Condens. Matter*, 19(386225), 2007.

[82] L. Reisinger. *Study of anisotropic electric and magnetic properties of Rare-Earth Nickel Dicarbides, RNiC$_2$*. Project Work, TU Wien, 2019.

[83] P. Fulde, and J. Jensen. Electronic heat capacity of the rare-earth metals. *Phys. Rev. B*, 27(7):4085, 1983.

[84] V.K. Anand, and Z. Hossain. Heavy fermion behavior in PrRh$_2$B$_2$C: Excitonic mass enhancement. *Phys. Rev. B*, 79(113107), 2009.

[85] S. Kirkpatrick, C. Gelatt Jr., and M. Vecchi. Optimization by Simulated Annealing. *Science*, 220:661–680, 1983.

[86] B. Stöger, X-Ray Diffraction Center TU Wien (Private Communication, 2021).

[87] V. Eremenko, V. Sirenko, V. Ibulaev, J. Bartolomé, A. Arauzo, and G. Reményi. Heat capacity, thermal expansion and pressure derivative of critical temperature at the superconducting and charge density wave (CDW) transitions in NbSe$_2$. *Physica C*, 469(7):259–264, 2009.

[88] R. Gupta, A. Thamizhavel, P. Rodière, S. Nandi, K. P. Rajeev, and Z. Hossain. Electrical resistivity under pressure and thermal expansion of LaPt_2Si_2 single crystal. *J. Appl. Phys.*, 125(143902), 2019.

[89] H. Kim, J. H. Shim, S. Kim, J.-H. Park, K. Kim, and B. I. Min. Unusual Pressure-Induced Quantum Phase Transition from Superconducting to Charge-Density Wave State in Rare-Earth-Based Heusler LuPd$_2$In Compound. *Phys. Rev. Lett.*, 125(157001), 2020.

[90] M. O. Ajeesh, T. Gruner, C. Geibel, and M. Nicklas. Possible Pressure-Induced Charge-Density Wave Quantum Critical Point in LuPd$_2$In. *J.Phys.Soc.Jpn*, 90(035001), 2021.

[91] S. Shimomura, C. Hayashi, N. Hanasaki, K. Ohnuma, Y. Kobayashi, H. Nakao, M. Mizumaki, and H. Onodera. Multiple charge density wave transitions in the antiferromagnets RNiC$_2$ (R = Gd, Tb). *Phys. Rev. B*, 93(165108), 2016.

[92] M. Roman. Research stay in frame of ETIUDA 6 grant "Charge density wave and magnetism in LnNiC$_2$ family (Ln - lanthanide)". 2018-2019.

[93] H. Onodera, M. Ohashi, H. Amanai, S. Matsuo, H. Yamauchia, Y. Yamaguchia, S. Funahashi, and Y. Morii. Noncollinear antiferromagnetic structure and commensurate-incommensurate transition of DyNiC$_2$ studied by magnetization measurement, neutron diffraction and ^{161}Dy Mössbauer spectroscopy. *J. Magn. Magn. Mater.*, 149:287–296, 1995.

[94] M. Sandrieser. *Crystal growth and studies of magnetic properties of rare earth nickel dicarbides.* Bachelor Thesis, TU Wien, 2021.

[95] Y. Koshikawa, H. Onodera, M. Kosaka, H. Yamauchi, M. Ohashi, Y. Yamaguchi. Crystalline electric fields and magnetic properties of single-crystalline RNiC$_2$ compounds (R= Ho, Er and Tm). *J. Magn. Magn. Mater.*, 173:72–82, 1997.

[96] H. Michor, S. Steiner, A. Schumer, M. Hembara, V. Levytskyy, V. Babizhetskyy, and B. Kotur. Magnetic properties of $HoNiC_2$, $HoNiC_2$ and their solid solutions. *J. Magn. Magn. Mater.*, 441(69-72), 2017.

[97] W. Jeitschko, and M.H. Gerss. Ternary Carbides of the Rare Earth ans Iron Group Metals with CeCoC_2 and CeNiC_2 -Type Structure. *J. Less-Common Met.*, 116:147–157, 1986.

[98] A. Lindbaum, and M. Rotter. *Handbook of Magnetic Materials - Chapter 4: Spontaneous Magnetoelastic Effects in Gadolinium Compounds*, volume 14. North-Holland, 2002.

[99] S. Katano, H. Nakagawa, K. Matsubayashi, Y. Uwatoko, H. Soeda, T. Tomita, and H. Takahashi. Anomalous pressure dependence of the superconductivity in noncentrosymmetric $LaNiC_2$: Evidence of strong electronic correlations. *Phys. Rev. B*, 90(220508), 2014.